PNNL-31557, Rev. 0
RPT-DFTP-028, Rev. 0

Fiscal Year 2021 Filtration of Hanford Tank 241-AP-107 Supernatant Samples Obtained at Prototypic Tank Level and Filtered at 16 °C

August 2021

JR Allred
JGH Geeting
AM Westesen
EC Buck
RA Peterson

Prepared for the U.S. Department of Energy
under Contract DE-AC05-76RL01830

DISCLAIMER

This report was prepared as an account of work sponsored by an agency of the United States Government. Neither the United States Government nor any agency thereof, nor Battelle Memorial Institute, nor any of their employees, makes **any warranty, express or implied, or assumes any legal liability or responsibility for the accuracy, completeness, or usefulness of any information, apparatus, product, or process disclosed, or represents that its use would not infringe privately owned rights**. Reference herein to any specific commercial product, process, or service by trade name, trademark, manufacturer, or otherwise does not necessarily constitute or imply its endorsement, recommendation, or favoring by the United States Government or any agency thereof, or Battelle Memorial Institute. The views and opinions of authors expressed herein do not necessarily state or reflect those of the United States Government or any agency thereof.

PACIFIC NORTHWEST NATIONAL LABORATORY
operated by
BATTELLE
for the
UNITED STATES DEPARTMENT OF ENERGY
under Contract DE-AC05-76RL01830

Printed in the United States of America

Available to DOE and DOE contractors from the
Office of Scientific and Technical Information,
P.O. Box 62, Oak Ridge, TN 37831-0062;
ph: (865) 576-8401
fax: (865) 576-5728
email: reports@adonis.osti.gov

Available to the public from the National Technical Information Service
5301 Shawnee Rd., Alexandria, VA 22312
ph: (800) 553-NTIS (6847)
email: orders@ntis.gov <https://www.ntis.gov/about>
Online ordering: http://www.ntis.gov

PNNL-31557, Rev. 0
RPT-DFTP-028, Rev. 0

Fiscal Year 2021 Filtration of Hanford Tank 241-AP-107 Supernatant Samples Obtained at Prototypic Tank Level and Filtered at 16 °C

August 2021

JR Allred
JGH Geeting
AM Westesen
EC Buck
RA Peterson

Prepared for
the U.S. Department of Energy
under Contract DE-AC05-76RL01830

Pacific Northwest National Laboratory
Richland, Washington 99354

Summary

Bench-scale filtration testing of 8.5 liters of supernatant from Hanford waste tank 241-AP-107, chilled to 16 °C, was conducted using a backpulse dead-end filter (BDEF) filtration system equipped with a feed vessel and a Mott inline filter Model 6610 (Media Grade 5) in the hot cells of the Radiochemical Processing Laboratory at Pacific Northwest National Laboratory. This was done to assess the impact of a lower sampling location within the tank as well the lowered filtration temperature on supernatant stability and fouling. The as-received samples were transferred to 1.5-liter poly bottles and held at 16 °C for approximately 1 week prior to filtration.

The feed was filtered through the BDEF system at a targeted flux of 0.065 gpm/ft^2 to match the prototypic operation of the Tank Side Cesium Removal (TSCR) system. During the initial period of filtration, the differential pressure required to effect filtration at 0.065 gpm/ft^2 increased until it reached 2 psid [the TSCR action limit] at 26 hours. After this, the filter was backpulsed to dislodge accumulated solids and reduce this pressure differential. An additional eight backpulses were conducted during the initial filtration period; each time, the target pressure was reached sooner than during the previous interval. Volume filtered decreased from 0.9 to 0.03 m^3/m^2 over the course of 14 processing hours. After the ninth backpulse, the backpulse frequency had become unsustainable, and it was decided to perform an extensive filter cleaning.

The filter was cleaned by draining the chilled AP-107 feed into chilled holding containers, introducing 0.1 M NaOH into the feed vessel, and recirculating the NaOH through the system for 20 minutes before allowing the system to soak for 2 hours without temperature control. A measurable decrease in filter resistance during this recirculation indicated that the 0.1 M NaOH was likely dissolving some of the solids that had deposited on the filter. Post cleaning, the filter resistance was effectively restored to initial conditions as the initial transmembrane pressure was restored to original levels. However, resumed processing of the AP-107 feed at 16 °C continued to result in an increased rate of filter resistance. An additional five backpulses were conducted (four during feed processing, one during subsequent cleaning) before the conclusion of the test.

Solids concentrated from the backpulse solutions displayed sodium oxalate-type phases, Al-oxides and sodium Al-oxides/carbonates, iron oxides, and Ca-bearing phases (calcite). The scanning electron microscopy analyses also revealed a large distribution of particles, with some particles, notably sodium phosphate dodecahydrate, having diameters close to 0.5 mm.

Acknowledgments

The authors gratefully acknowledge the help of hot cell technicians Jarrod Turner, Hollan Brown, Michael Rojas, and Robert Cox in conducting this work. We thank Richard Daniel for conducting the technical reviews of the calculation files and test data packages. We also thank Matt Wilburn for technical editing of this report and Bill Dey for the quality reviews of the calculation packages and this report.

Microscopy work was performed at the Radiochemical Processing Laboratory Quiet-Suite at Pacific Northwest National Laboratory.

Acronyms and Abbreviations

AEA	alpha energy analysis
BDEF	backpulse dead-end filter (system)
BSE	backscattered electron
CWF	clean water flux
EDS	X-ray energy dispersive spectroscopy
EELS	electron energy loss spectroscopy
FEG	field emission gun
FFT	fast Fourier transform
HAADF	high-angle annular dark-field
IX	ion exchange
LAW	low-activity waste
MFC	mass flow controller
PNNL	Pacific Northwest National Laboratory
QA	quality assurance
R&D	research and development
RPL	Radiochemical Processing Laboratory
RPT	Radiation Protection Technologist
RTD	resistance temperature detector
SDD	silicon drift detector
SE	secondary electron
SEM	scanning electron microscopy
STEM	scanning transmission electron microscopy
TEM	transmission electron microscopy
TRU	transuranic
TSCR	Tank Side Cesium Removal
WRPS	Washington River Protection Solutions
WTP	Waste Treatment and Immobilization Plant
WWFTP	WRPS Waste Form Testing Program
XRD	X-ray diffraction

Contents

Figures

Tables

1.0 Introduction

The U.S. Department of Energy's Hanford Site houses 56 million gallons of high-level radioactive waste generated from plutonium production from 1944 to 1988 (Gerber 1992). The supernatant waste, currently stored in underground tanks, is intended to be vitrified following filtration and ^{137}Cs removal at the Hanford Waste Treatment and Immobilization Plant (WTP) Pretreatment Facility. Because the Pretreatment Facility will not be operational for several years, ^{137}Cs will be removed from low-activity waste (LAW) vitrification feeds using the Tank Side Cesium Removal (TSCR) system in a technology demonstration that will filter and remove cesium from tank waste supernate to support transferring the TSCR-processed waste directly to the WTP LAW Facility. The TSCR system is skid-mounted and employs two key technologies: (1) dead-end filtration for solids removal and (2) ion exchange (IX) for cesium removal. Filtration is necessary to protect the functionality of the IX columns.

A small-scale test platform was established in 2017 to demonstrate these processes in the Pacific Northwest National Laboratory (PNNL) 325 Building, also known as the Radiochemical Processing Laboratory (RPL).

The presence of solids has been observed in previous filtration experiments using waste from Hanford tanks 241-AP-105 and 241-AP-107 (Geeting et al. 2018a,b; Allred et al. 2020). The first test with AP-107 was performed with samples that were retrieved from the tank within a few weeks of raw water addition (and tank recirculation); solids were observed in those filtration experiments. Additional AP-107 samples were taken 14 months later and filtration showed no recoverable solids (Geeting et al. 2019), indicating that settle-then-decant works to reduce solids in supernatant. Both sets of these samples were taken from relatively high in tank AP-107; however, the pump suction is located much lower in the tank. In addition, the prior tests were performed at the ambient temperature of the hot cell (25 to 30 °C), while the TSCR operating temperature may be as low as 16 °C.

Solids obtained from the first sampling event in AP-107 are suspected to be due to tank mixing and formation of precipitates when combined with process water to achieve a dilution from 8.5 to 5.6 M Na for prototypic processing conditions. Formation of solids upon dilution with process water is supported by Daniel et al. (2020), who observed that precipitates formed upon dilution of AP-105 simulant with process water. However, reducing the temperature to 16 °C is also suspected of having the potential to produce additional solids.

Thus, the objective of the current work was to perform filtration under prototypic conditions using Mott Grade 5 sintered metal at the targeted flux of 0.065 gpm/ft^2 planned for TSCR, at the TSCR operation temperature, on feed obtained closer to the pump suction to assess whether these two factors (depth of sample collection in the waste tank and filtration temperature) result in higher solids loading to the filters, and thus lower filter fluxes. Filter resistance as a function of time was measured and the filter was backpulsed if the differential pressure increased to 2 psi across the filter. Backpulse solutions were collected and solids were found and assessed by microscopy methods.

2.0 Quality Assurance

All research and development (R&D) work at PNNL is performed in accordance with PNNL's Laboratory-Level Quality Management Program, which is based on a graded application of NQA-1-2000, *Quality Assurance Requirements for Nuclear Facility Applications* (ASME 2000), to R&D activities. To ensure that all client quality assurance (QA) expectations were addressed, the QA controls of PNNL's Washington River Protection Solutions (WRPS) Waste Form Testing Program (WWFTP) QA program were also implemented for this work. The WWFTP QA program implements the requirements of NQA-1-2008, *Quality Assurance Requirements for Nuclear Facility Applications* (ASME 2008), and NQA-1a-2009*, Addenda to ASME NQA-1-2008* (ASME 2009), and consists of the WWFTP Quality Assurance Plan (QA-WWFTP-001) and associated QA-NSLW-numbered procedures that provide detailed instructions for implementing NQA-1 requirements for R&D work.

The work described in this report was assigned the technology level "Applied Research" and was planned, performed, documented, and reported in accordance with procedure QA-NSLW-1102, *Scientific Investigation for Applied Research*. All staff members contributing to the work received proper technical and QA training prior to performing quality-affecting work.

3.0 Test Conditions

In November 2020, WRPS collected 36 supernatant samples (~250 mL each) from tank 241-AP-107 in two batches, at a level near the pump suction (3 ft from the bottom of the tank), and provided them to PNNL. Two of the sample containers were held for IX batch contacts, leaving 34 bottles for filtration. At the RPL, PNNL composited the 34 remaining samples into 1.5-L polyethylene bottles and chilled the bottles (16 °C setpoint) for approximately 1 week. Filtration testing of the tank waste began on February 9, 2021 using a new Mott Model 6610 (Media Grade 5) line filter with porous end cap. This is a sintered 316L stainless steel filter with a 0.317-in. porous diameter, 1.463-in. porous length, and 1.51-in.^{2} filter area.

3.1 BDEF Filtration

3.1.1 Backpulse Dead-End Filter (BDEF) System Description

The filtration system is the same system that was used in fiscal year 2020 (Allred et al. 2020) with a few modifications to support reduced-temperature filtration. Modifications included two additional heat exchangers installed in the hot cell (connected to two chillers) to control the temperature of the feed before and during filtration. The first new heat exchanger (trough heat exchanger) kept all the feed at the setpoint temperature until it was added to the BDEF system. The trough heat exchanger has dimensions of 9 in. × 25 in. × 12 in. (width, length, height) with removable cover on the top. The feed bottles were stored in the trough heat exchanger with a cover until the feed was transferred to the BDEF system.

Once the feed was added to the BDEF, the existing heat exchanger kept the feed at the setpoint temperature in the reservoir and in the BDEF recirculation loop. The second new heat exchanger (clamshell heat exchanger) completely enclosed the filter and associated tubing to keep the feed at the setpoint temperature as it exited the recirculation loop until it was filtered. After filtration, the temperature was no longer controlled.

A piping and instrumentation diagram is provided in Appendix A. A photograph of the BDEF system installed in the RPL Shielded Analytical Laboratory hot cell is shown in Figure 3.1.

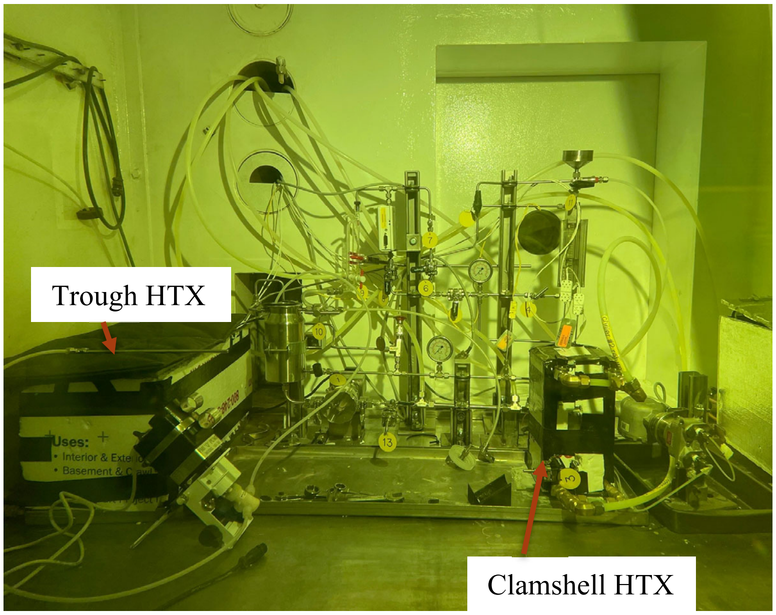

Figure 3.1. BDEF system installed in hot cell. HTX = heat exchanger.

The BDEF system is composed of a slurry recirculation loop, a filter assembly, and a permeate system. The main recirculation loop consists of a 1-liter stainless steel container (Eagle, EPV1A), a low-shear quaternary diaphragm pump (Quattro Flow QF150), a heat exchanger, and a throttle valve. The pump speed is controlled by a variable frequency drive that is located outside the hot cell. The slurry flow rate and pressure are controlled by adjusting the pump variable frequency drive (pump speed control) and throttle valve. The recirculation loop provides mixed, pressurized feed to the filter assembly. During the testing described in this report, the slurry temperature was controlled at a 16 °C setpoint.

The filter assembly receives pressurized slurry from the slurry recirculation loop. The filter assembly is composed of a filter, a Rosemount differential pressure transducer, and a flush valve (V3 in Appendix A). The flush valve is actuated during backpulse operations used to clear solids off the filter and out of the system.

The permeate system receives permeate produced by the filter assembly. The permeate flow rate is controlled with a mass flow controller (MFC), which can control feed in the range of 0.15 to 0.33 liter/hour. (These rates equate to allowable filter areas of 1.5 to 3.3 in.^{2} assuming flux of 0.065 gpm/ft^2.) The MFC measures flow rate and density of the permeate while a glass flowmeter is provided as a secondary flow rate measurement device. The permeate system can also perform a backpulse function. Pressurized air can be introduced (V12) into the backpulse chamber and used to force permeate (or other fluids) backward through the filter and out of the system through V3.

The Mott 6610 filter used in testing is cylindrical, with dimensions of 0.317-in. diameter × 1.5-in. length and a filtration area of 1.51 in.^{2}. The filter element is fabricated from a seamless sintered stainless steel tube that is a closed/dead-end porous tube (with a porous end cap); the open end is welded to a pipe-reducing bushing. At 0.065 gpm/ft^2, the rate of filter processing is 3.7 L feed per 24-hour day. Figure 3.2 shows a schematic of the filter assembly and a photo of the filter.

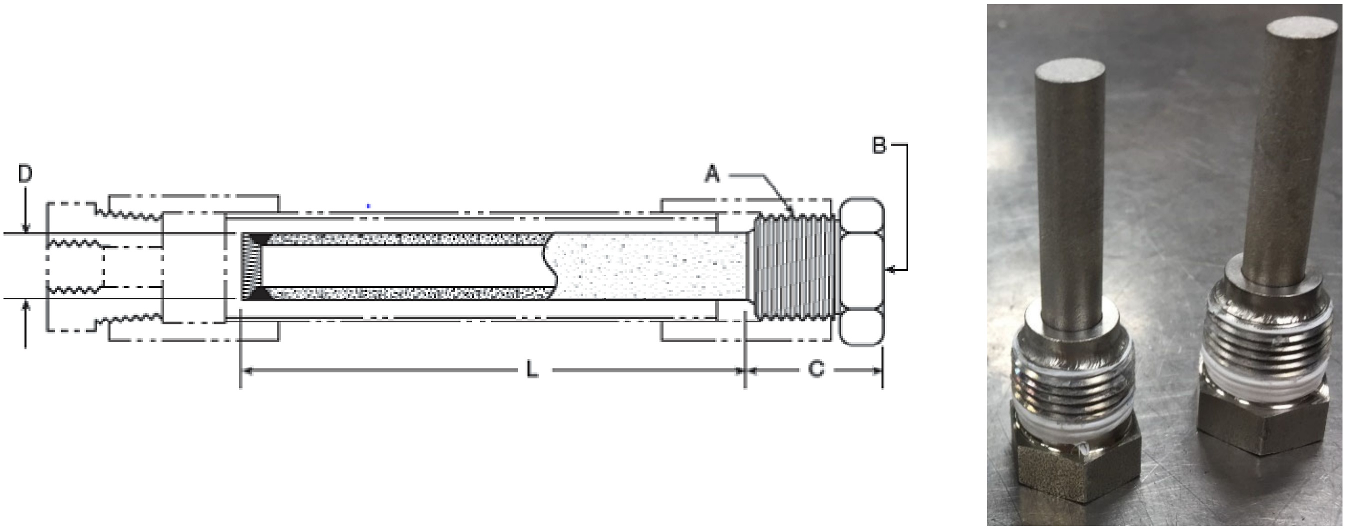

(a) (b)

Figure 3.2. (a) Filter housing schematic[1] (note that the 6610 series filter was welded to a 3/8-in. pipe fitting, making the configuration similar to the 6480 series illustrated here); (b) photo of modified filters with filter housings removed.

3.1.2 System Operation during Testing

The evolutions used to test the diluted AP-107 waste samples are outlined below.

1. Clean water flux (CWF) measurement: The CWF measurement serves as a system leak test and provides a baseline measurement of the filter resistance; it was conducted with 0.01 M NaOH solution at nominal test conditions (2.57 mL/min) and operated for 16 min. After the CWF, the BDEF system was drained.
2. Filtration of AP-107 – filtered AP-107 feed with the BDEF at nominally 2.57 mL/min: The targeted filtration rate is based on scaled flux used during AVANTech testing.[2] The filtration rate was controlled with an MFC. Permeate was sampled after approximately 1/3, 2/3, and 3/3 of the feed had been filtered.

   The filter was backpulsed when the differential pressure was greater than 2 psid. Each backpulse used a charge of pressurized air to push nominally 26 mL of filtered permeate through the filter at a rate of nominally[3] 1.5 mL/s.

---

[1] Mott 6480 line filter from https://mottcorp.com

[2] 0.306 gpm through 4.7 ft^2 of Mott sintered metal filter (0.065 gpm/ft^2) obtained from *TSCR Dead End Filter Scoping Test Summary*, presentation by AVANTech Inc., November 13, 2018, Richland, Washington.

[3] Scaled from 2.2 gpm/ft^2 per AVANTech communications. Tracy Barker (AVANTech VP and principal engineer), “RE: TSCR Filter Cleaning Procedure,” email message to Jarrod Allred (PNNL engineer), March 20, 2020.

The filter was cleaned after approximately 39 hours of filtration operations (and nine periodic backpulses) because of the marked reduction in permeate recovered by filter backpulse. The filter was cleaned after draining the AP-107 from the BDEF system. (Drained AP-107 was stored in the trough heat exchanger and maintained at the 16 °C setpoint temperature.) A solution of 0.1 M NaOH was added to the BDEF system and pumped through the filter. The recirculation pump was turned off and the filter soaked in the hydroxide solution for 2 hours without temperature control. A measurable decrease in filter resistance during this recirculation indicated that the 0.1 M NaOH was likely dissolving some of the solids that had deposited on the filter. After the filter soak, the filter was backpulsed. Then, the BDEF system was drained of the cleaning solution and filtration of AP-107 continued (second cycle). The filtration test concluded after approximately 14 additional hours of filtration operations, during which time an additional four backpulses were conducted to address increases in transmembrane pressure.

3. The BDEF system was drained.
4. Filter cleaning: 0.1 M NaOH was added to the BDEF system and pumped through the filter. The recirculation pump was turned off and the filter soaked in the hydroxide solution for 2 hours. After the filter soak, the filter was backpulsed, then the BDEF system was drained of the cleaning solution.
5. The BDEF system was rinsed using 0.01 M NaOH and subsequently drained.
6. Final CWF measurement: After rinsing, another CWF test was conducted using fresh 0.01 M NaOH solution using the same conditions outlined in Evolution 1.
7. The BDEF was laid-up for post-test storage.

Table 3.1 provides a mass balance for the BDEF testing. A total of 11,363 g of AP-107 supernatant was added to the BDEF system during testing, and a total of 11,175 g was removed. The missing mass (~190 g) is likely due to evaporation and material that wets the inside of the BDEF system, is not recoverable, and represents less than 2% of the initial feed.

Table 3.1. Mass balance – BDEF.

Description	In (g)	Out (g)
Decanted supernate filtration	11,363.1	
Product to IX		9,941.0
Permeate samples		17.5
Backpulse samples		907.5
Drained from BDEF		309.4
Total	11,363.1	11,175.4

The permeate density of the filtered AP-107 product (to be used for IX) was determined gravimetrically by measuring 10 mL from each permeate collection bottle into a volumetric flask and weighing on an analytical balance. The density average was 1.271 g/mL (0.38% relative standard deviation). Results are provided in Table 3.2.

Table 3.2. Density of filtered AP-107 for Cs ion exchange.

Bottle ID	Vol Flask Tare (g)	Vol Flask Gross (g)	Measured Density (g/mL)
IX-AP7-1	15.0431	27.7491	1.2706
IX-AP7-2	15.1585	27.9176	1.2759
IX-AP7-3	15.2166	27.8959	1.2679
IX-AP7-4	15.1827	27.8597	1.2677
IX-AP7-5	15.1729	27.8050	1.2632
IX-AP7-7	14.4186	27.1903	1.2772
IX-AP7-Last	14.5879	27.2979	1.2710

3.2 Feed Temperature Control

Figure 3.3 provides the temperature profile of the AP-107 feed as it awaited introduction into the BDEF system for filtration. The feed was chilled and held at the 16 °C setpoint temperature for approximately 1 week before the start of filtration testing. Two 100-ohm platinum resistance temperature detector (RTD) probes, labeled TE-104 and TE-105, measured the temperature in different feed bottles held in the trough heat exchanger and averaged 16.3 and 15.8 °C, respectively. Near the end of testing, TE-105 was removed from service when its feed bottle was emptied.

At 0100 on 2/11/21, feed was drained from the BDEF (and added back into the feed bottle) in preparation for filter cleaning. During this operation, the TE-104 probe was removed from the feed bottle. When TE-104 was returned to the feed bottle and allowed to come to thermal equilibrium, an increase in temperature of approximately 1.5 °C was observed and was a result of the transfer operation. The second spike in temperature on 2/11/21 is a result of temporarily removing the RTD when managing the feed bottles in the trough heat exchanger.

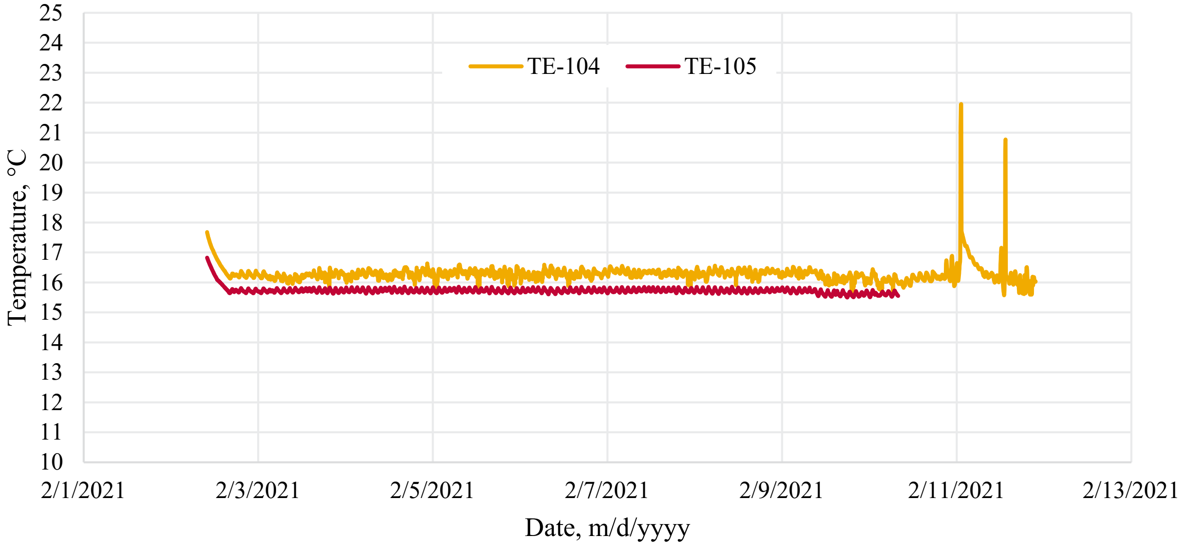

Figure 3.3. AP-107 temperature in the trough heat exchanger.

Figure 3.4 shows the temperature of the AP-107 in the BDEF recirculation loop (TE-101) during the entire filtration test. Similarly, the temperature profile of the AP-107 feed immediately before (TE-102) and after (TE-103) the filter is shown in Figure 3.5. Filtration started at 0810 on 2/9/21 and concluded at 0204 on 2/12/21. The small temperature increases shown in the figures are a result of backpulsing the filter, which increased in frequency especially before filter cleaning and near the conclusion of testing. During a backpulse, the recirculation pump is turned off and the AP-107 temperature increases in the 1/4-in. tubing, as the fluid is no longer being circulated through heat exchangers. However, the bulk of the fluid is in the 1-liter slurry reservoir, and when the pump is turned back on (after the backpulse) the temperature rapidly returns to near the setpoint. This, and the much smaller temperature changes shown in Figure 3.5, indicates that the temperature swings shown in Figure 3.4 are exaggerated relative to those experienced by the large mass of feed stored in the 1-liter reservoir. The large temperature increase on 2/11/21 is due to draining the BDEF system and cleaning the filter with 0.1 M NaOH (see Section 4.3 for a description) and is not representative of the AP-107 temperature during filtration (see Section 4.2 for a timeline of events).

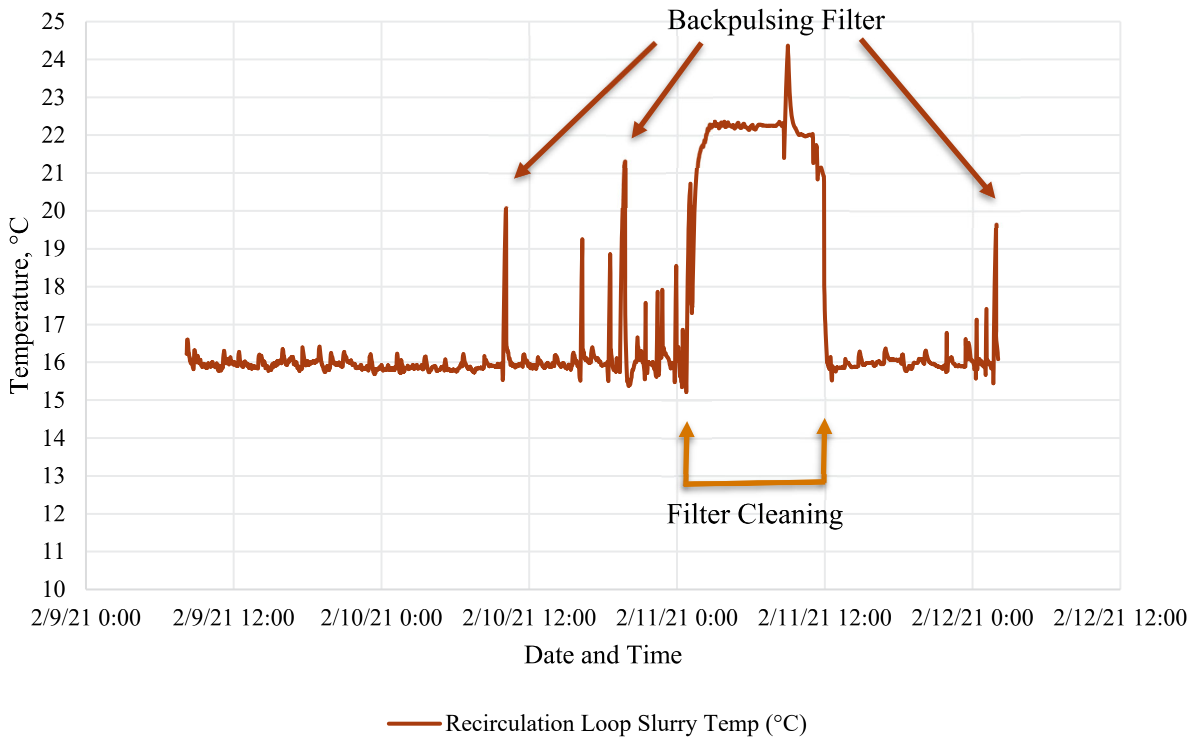

Figure 3.4. AP-107 temperature in the BDEF recirculation loop.

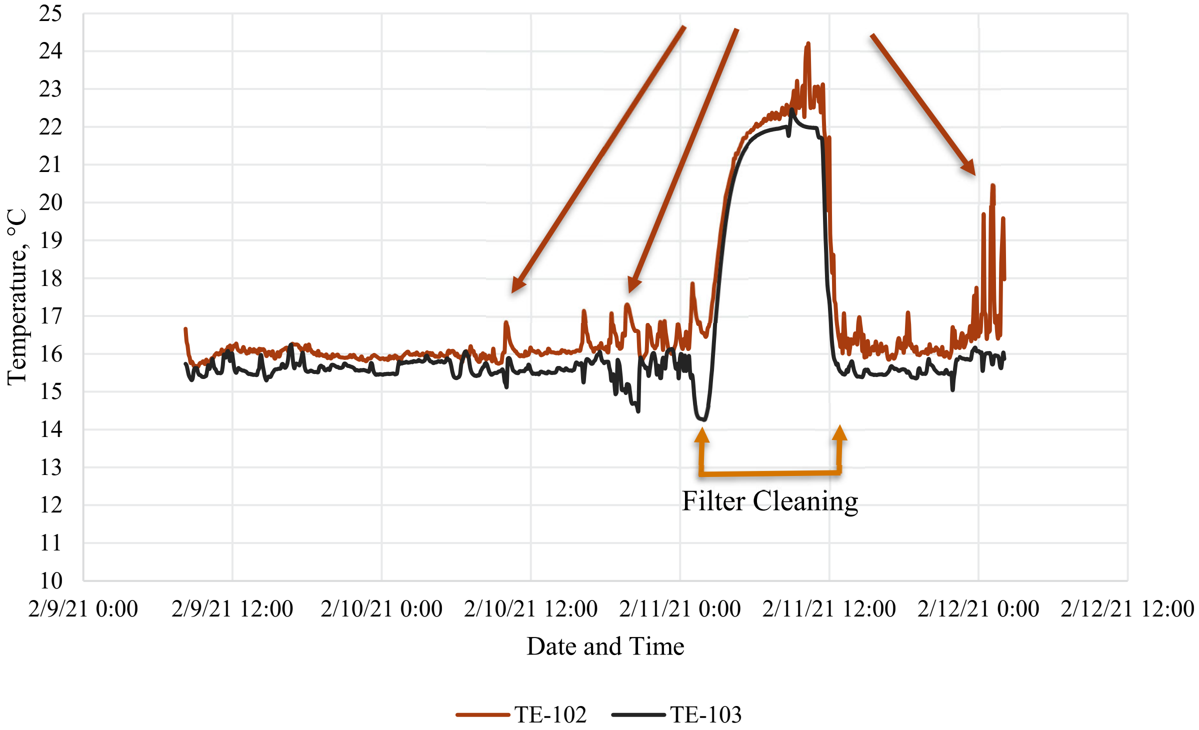

Figure 3.5. AP-107 temperature in the clamshell heat exchanger.

3.3 Sample Analysis

Three permeate samples (TI-088-P1, TI-088-P2, TI-088-P3) were collected after approximately 1/3, 2/3, and 3/3, of the AP-107 feed had been filtered. These samples were submitted for total alpha analysis to determine the transuranic content of the filtered permeate.

A total of 14 backpulses (nine before the filter was cleaned, five after) were performed during filtration operations when the system was filled with AP-107 feed. To concentrate solids, solutions collected from the feed backpulse events were centrifuged at 2500 rpm for 10 min. The bulk amount of the supernatant was decanted and the solids from the centrifuge tubes were suspended and combined. The decanted supernatant was added to an AP-107 feed bottle and filtered in the BDEF system. Very few solids were collected and there was only sufficient sample available to conduct scanning electron microscopy (SEM) analysis. The SEM results are reported in Section 4.5. Figure 3.6 shows the solids that were collected from the backpulsed solution after the solutions were centrifuged and decanted to further concentrate the solids.

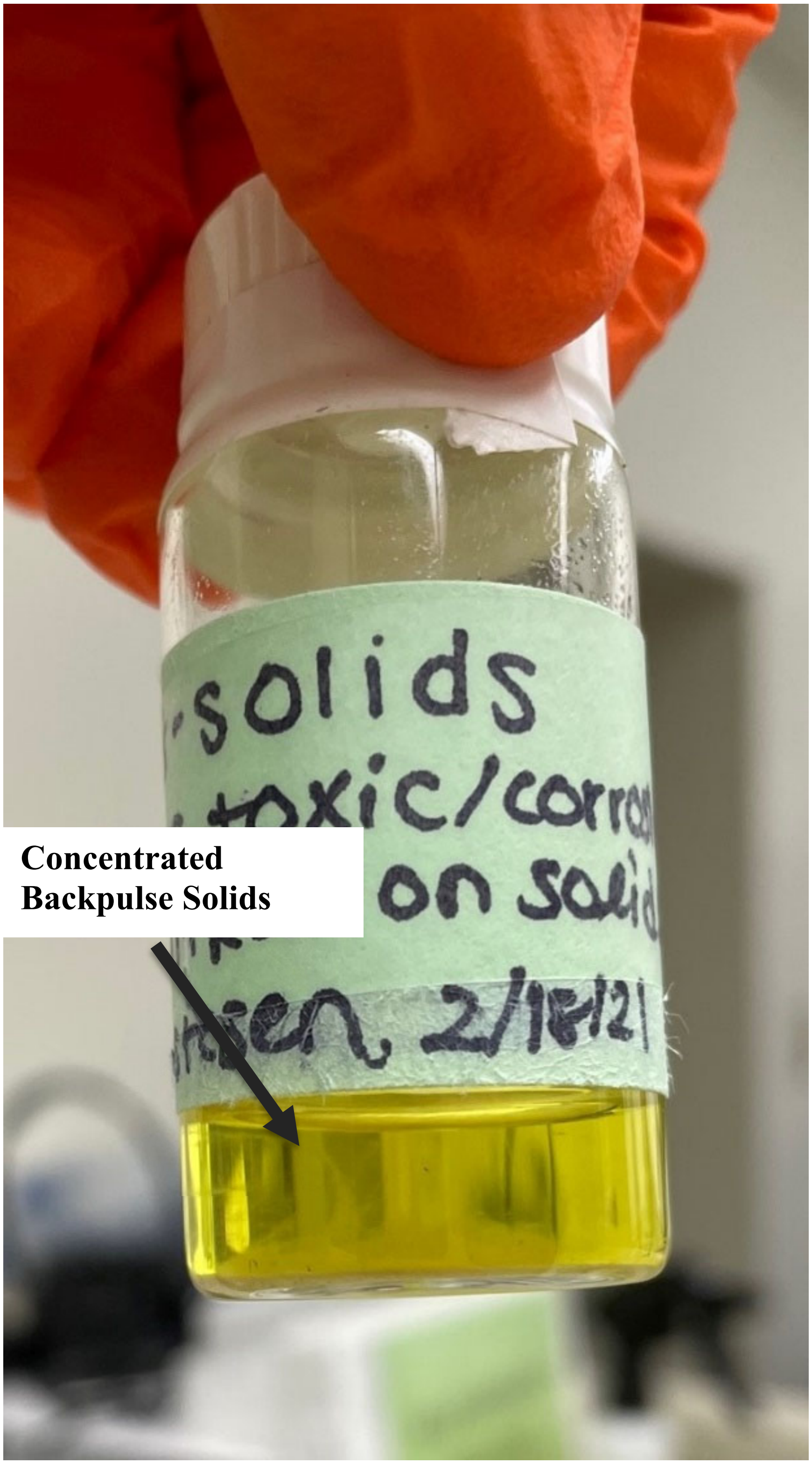

Concentrated Backpulse Solids

Figure 3.6. Concentrated solids after centrifugation.

4.0 Results

4.1 Clean Water Flux

The objective of the CWF is to assess the state of the system at the start of testing to ensure a uniform basis for comparing different filtration trials, and in particular to ensure that the system is "clean" at the start of testing. Figure 4.1 shows the initial CWF at 16 °C using 0.01 M NaOH with the Media Grade 5 stainless steel BDEF filter. The CWF tests were conducted at ambient cell temperature at a nominal 2.57 mL/min permeate flow rate. The transmembrane pressure averaged 0.043 psid in the initial CWF with an average filter resistance of 6.06×10^{9} m^{-1}. Resistance is calculated via Darcy's law:

$$Q = \frac{PA_t}{\mu R}$$

where Q is the volumetric flow rate [m^3/s], P is the transmembrane pressure [Pa], A_t is the total filter area [m^2] [9.74×10^{-4} m^2], μ is the filtrate dynamic viscosity [Pa·s] (assumed to be 1.11 cP). Rearranging so that:

$$R(t) = \frac{P(t)A_t}{\mu Q(t)}$$

Prior CWF results ranged from 0.015 to 0.1 psid transmembrane pressure (Allred et al. 2020). These values all are likely within the accuracy of the CWF measurement and represent a relatively clean filter. Estimates of the resistance for the Mott 6610 series Grade 5 are on the order of 2×10^{10} m^{-1}. By this metric, the filter is cleaner than the baseline flux by a factor of ~2. If there were significant fouling (due to residual solids in the system), the upward curvature of the differential pressure would be greater during the CWF. As such, these results indicate an overall clean system at the start of testing.

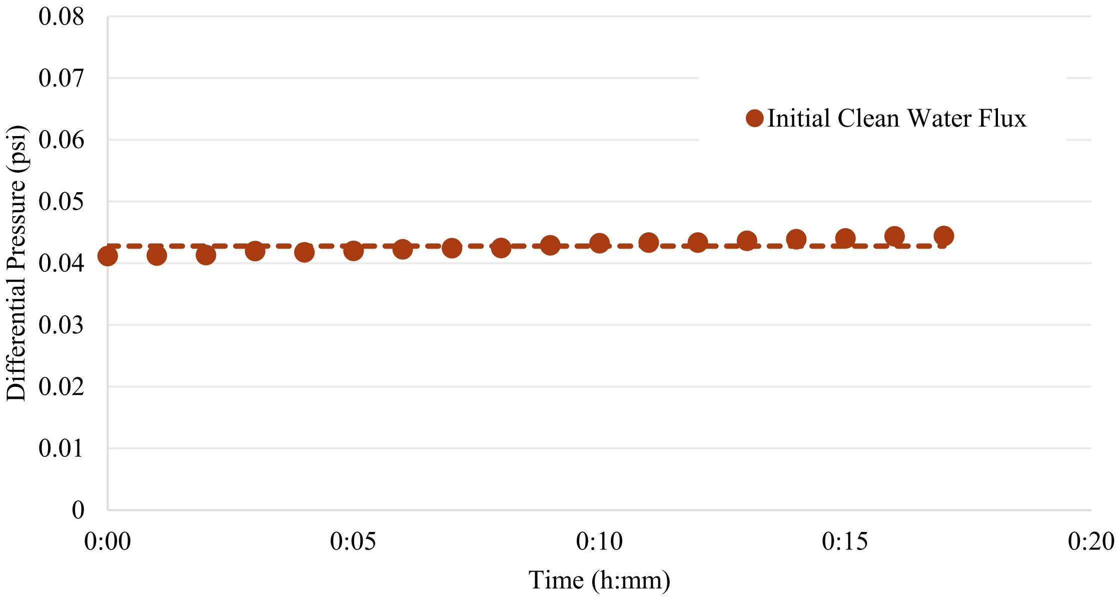

Figure 4.1. CWF measurements for Media Grade 5 BDEF at 0.33 liter/hour permeate rate (nominal) before testing. (Dashed line is average pressure over the 15-minute period.)

4.2 BDEF Filtration

Table 4.1 provides a timeline for filtration testing. Testing was started the morning of February 9 at 8:10 a.m. For the duration of the first 24 hours of testing, the filter resistance increased gradually. At 22 hours of operation (3.4 m^3/m^2), there is a discontinuity in the resistance increase. This does not coincide with any of the bottle changes, which has been shown in the past to cause a discontinuity in the resistance increase. However, this type of discontinuity has been seen previously and is generally associated with sloughing of solids from the filter surface. After this event, the filter resistance continued to increase until the 2 psid target was reached after 25 hours and 53 minutes of operation (4.07 m^3/m^2). A backpulse was performed and filtration was resumed. The resistance was significantly reduced by the backpulse, but did not return to the original condition ($7.7x10^9$ m^{-1} after the first backpulse versus $4.3x10^9$ m^{-1} at the start of testing); see Figure 4.8 for more detail regarding filter restoration after backpulse. Filtrate viscosity used in these resistance calculations is assumed to be 6.3 cP, derived from Geeting et al. (2018b) for 5.6 M Na AP-105 supernatant measured via rheometer at 16°C.

Table 4.1. System timeline.

Date	Time	Volume Filtered (m^3/m^2)	Event
09-Feb-21	08:10	0.00	Filtration Started
10-Feb-21	09:47	4.08	Backpulse 1 with 50 psig air motive force
	16:01	4.99	Backpulse 2 with 50 psig air motive force
	18:19	5.31	Backpulse 3 with 50 psig air motive force
	18:19 – 20:46	5.31	Stopped filtration - replace mass flow controller
	20:46	5.31	Resumed filtration
	21:20	5.36	Backpulse 4 with 50 psig air motive force
	22:01	5.43	Backpulse 5 with 50 psig air motive force
	22:42	5.45	Backpulse 6 with 50 psig air motive force
	23:28	5.55	Backpulse 7 with 50 psig air motive force
11-Feb-21	00:15	5.58	Backpulse 8 with 50 psig air motive force
	00:42	5.62	Backpulse 9 with 50 psig air motive force
	00:42-08:40	5.62	After backpulsing, drained AP-107 from BDEF and stored in trough chiller, then cleaned filter
	08:40-12:08	5.62	Cleaned filter with 0.1 M NaOH (20-minute recirculation, 2-hour soak)
	12:08	5.62	Resumed filtration
	21:50	7.13	Backpulse 10 with 50 psig air motive force
	00:15	7.49	Backpulse 11 with 50 psig air motive force
12-Feb-21	01:02	7.59	Backpulse 12 with 60 psig air motive force
	01:39	7.67	Backpulse 13, with 60 psig air motive force
	02:04	7.69	Backpulse 14, filtration complete

As seen in Figure 4.2, the resistance increased faster after the first backpulse (less volume filtered at a constant flow rate = shorter time interval); it reached the 2-psi threshold after 0.914 m^3/m^2 volume filtered. This behavior was repeated after the second backpulse, and reached the pressure limit significantly less time. After the third backpulse, testing was stopped for a short duration to replace the mass flow controller. Once testing was restarted, the duration between backpulses continued to shorten, as seen in Figure 4.3. In an attempt to extend the period between backpulses, the target pressure was allowed to increase to 4 psi. However, this did little to extend the time period as the filter continued to foul ever faster (see Table 4.2).

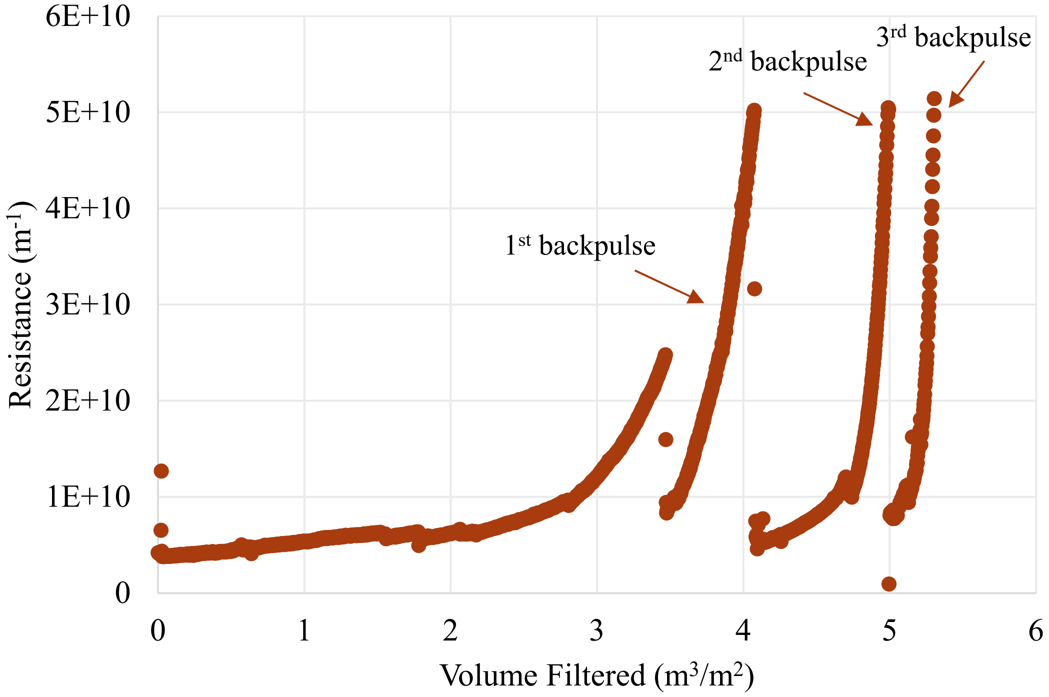

Figure 4.2. Filter resistance for filtration prior to cleaning, backpulses 1 through 3.

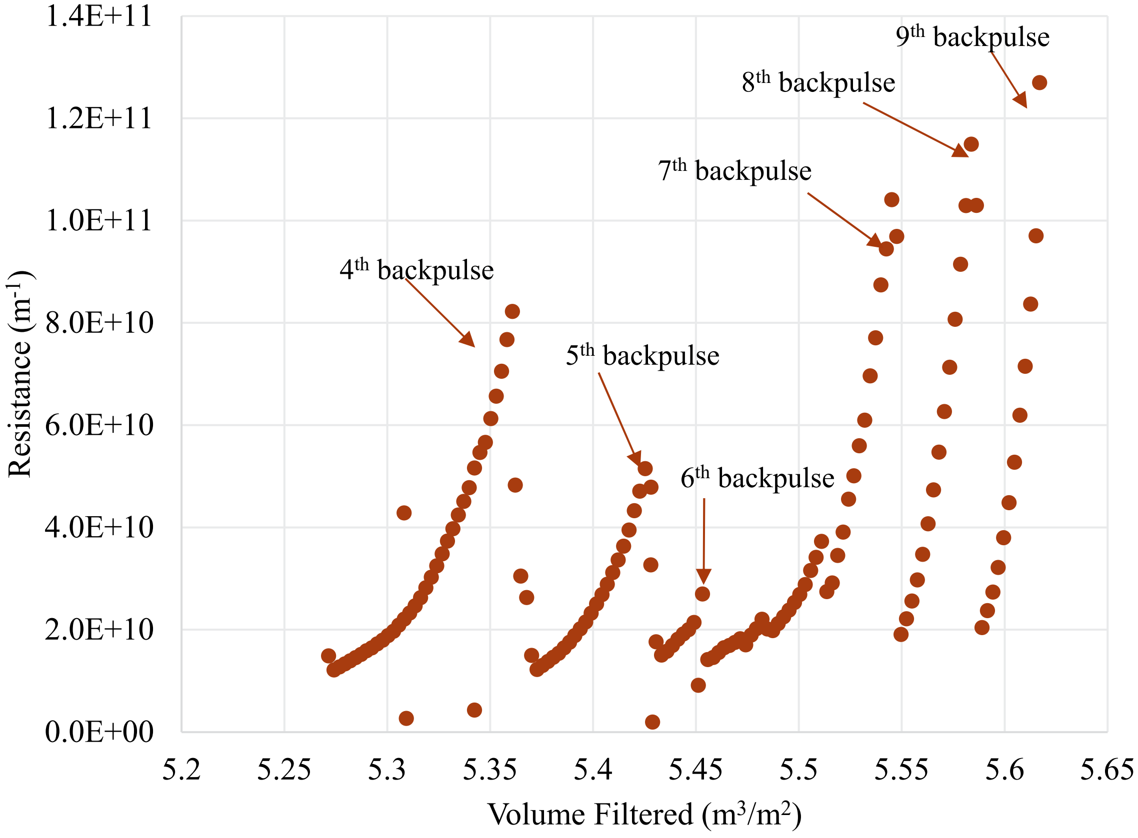

Figure 4.3. Filter resistance for filtration prior to cleaning, backpulses 4 through 9.

After the ninth backpulse, the backpulse frequency had become untenable as the quantity of backflush fluid used to clear the solids outpaced the permeate production rate. It was decided to perform a more extensive filter cleaning.

As indicated in Section 3.1.2, the filter was cleaned at this point by draining the AP-107 feed into chilled holding containers, introducing 0.1 M NaOH into the feed vessel, and recirculating this solution through the system to ensure the filter was filled with 0.1 M NaOH. During this operation, the filter resistance decreased measurably, indicating that this process alone was likely dissolving some of the solids that had deposited on the filter. The filter was subsequently allowed to soak for 2 hours before another backpulse was performed and filtration restarted after replacing the cleaning solution with AP-107 feed. This cleaning protocol improved filter performance but did not restore the system to the original condition. While the initial post-cleaning resistance (3.9×10^9 m^{-1}) was effectively the same as the initial condition (4.3×10^9 m^{-1}), the filter resistance increased much faster after the cleaning than during the initial testing (see Figure 4.4). Testing was continued with backpulses performed as required to process the balance of the feed, which was accomplished with four subsequent backpulses without having to resort to an additional filter cleaning.

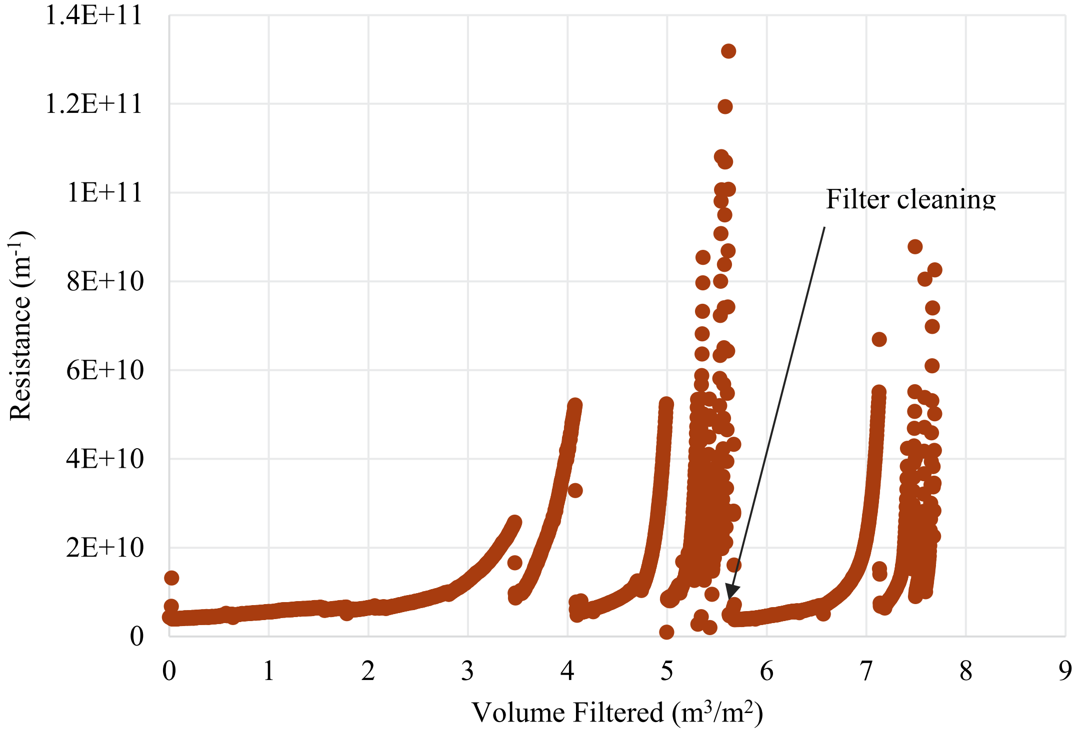

Figure 4.4. Filter resistance before and after filter cleaning.

A comparison of the efficacy of backpulsing shows that while the initial resistance was restored significantly by a backpulse, the time to reach the 2-psid action threshold deteriorated quickly as subsequent backpulses were performed. Table 4.2 provides the test parameters prior to backpulsing, highlighting the reduced volume filtered after each successive backpulse (reduced volume filtered corresponds to shorter time). It was observed that simple backpulsing quickly became ineffective at dislodging particles from the filter surface and subsequent filter fouling accelerated. In contrast, flowing dilute caustic solution through the filter apparently dissolved some of the solids. It should be noted, however, that this dissolution appears far from complete. While the initial resistance appears similar, the duration to reach 2 psi was significantly reduced (by roughly 2/3) after the filter cleaning. These results suggest that some of the solid species may not dissolve in the cleaning solution used for this cleaning protocol.

Note that the effectiveness of the TSCR cleaning protocol is expected to fall somewhere between a backpulse and the cleaning protocol used in this test. The TSCR protocol does not actively flow solution through the system as was done to charge the test platform filter. Thus, the test platform provides a reasonable bound on expected full-scale performance. That is, performance of the TSCR system should neither be worse than observed with the backpulse nor better than observed with the test system cleaning protocol for this type of feed.

The reduced volume filtered after each successive backpulse is consistent with depth fouling of the filter. Depth fouling is characterized as a slow increase in filter resistance as the pores are filled with solids. Once nearly all the pores are filled, the filter resistance begins to increase rapidly, as additional solids are deposited on the surface of the fouled filter. This type of depth fouling is also expected to result in the type of backpulse behavior that was observed. Depth fouling will be less amenable to restoration by backpulsing, as the solids will lodge deep in the pores and be difficult to dislodge. This type of filtration behavior is seen when the size of the particles is such that they are not rejected at the surface of the filter, but rather penetrate the depth of the filter.

Table 4.2. Test parameters prior to backpulsing.

Test Event	Filtration Resistance (m^{-1})	Volume Filtered (m^3/m^2)	Transmembrane Pressure (psid)
Backpulse 1	5.21E+10	4.08	2.01
Backpulse 2	5.22E+10	0.914	2.00
Backpulse 3	5.34E+10	0.309	2.06
Backpulse 4	8.54E+10	0.095	3.29
Backpulse 5	5.34E+10	0.063	2.06
Backpulse 6	6.17E+12	0.024	2.20
Backpulse 7	1.08E+11	0.095	4.16
Backpulse 8	1.19E+11	0.038	4.60
Backpulse 9	1.32E+11	0.032	3.31
Backpulse 10	6.69E+10	1.51	2.45
Backpulse 11	8.78E+10	0.358	3.51
Backpulse 12	8.05E+10	0.097	3.03
Backpulse 13	7.40E+10	0.076	2.80
Backpulse 14	8.26E+10	0.023	1.80

It is desirable to compare these filtration results with previous AP-107 BDEF testing. Work done in 2019 was performed at 25 °C at a permeate flow rate of 0.065 gpm/ft^2 and with a sample gathered higher in the tank, at 50” below the waste surface and 367” from the bottom of the tank (Geeting et al. 2019). This previous test was also performed using a larger dead-end filter (3.24 in.^{2} vs. 1.51 in.^{2}). This resulted in truncated data sets when compared to the current (2021) testing. Figure 4.5 shows that the 2021 testing (16 °C data in the figure) resulted in fouling whereas the 2019 testing (25 °C data) did not experience any increase in filter resistance.

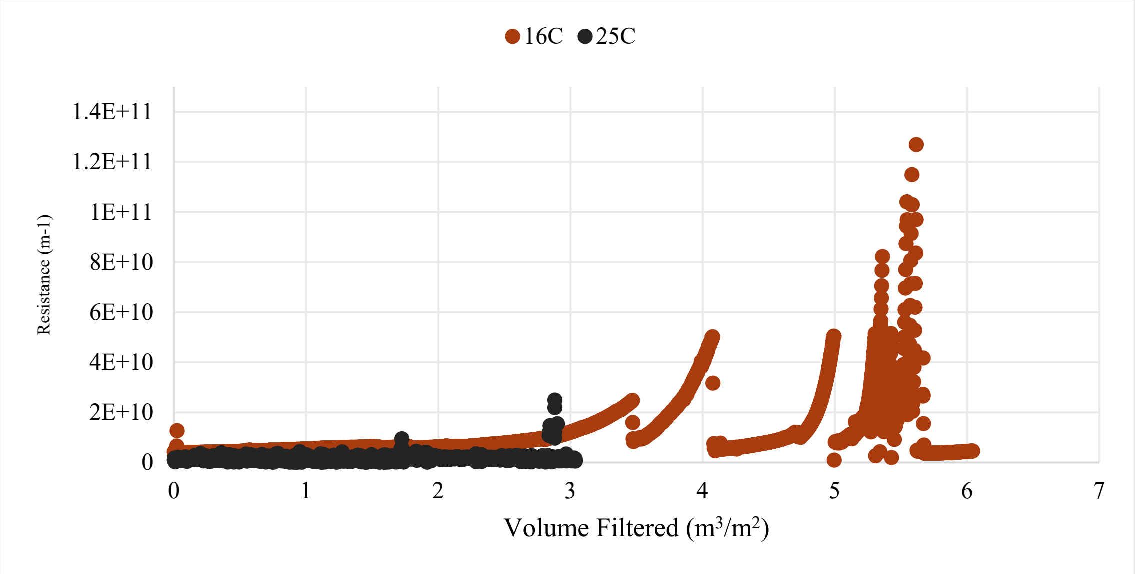

Figure 4.5. Comparison of filter data at 25 °C (2019 testing; higher sampling location in Tank AP-107) vs. 16 °C (2021 testing; lower sampling location).

To better quantify this filter fouling, three blocking filtration laws were used to model each test data set prior to backpulse. These filtration laws are described in more detail in Hermia (1982) and Allred et al. (2020). The filtration laws were solved for the following volumetric flow rate equations:

$$Q(t) = Q_0 \, e^{-K_i V(t)} \qquad \text{Intermediate blocking}$$

$$Q(t) = Q_0 + K_b V(t) \qquad \text{Complete pore blocking}$$

$$Q(t) = Q_0 \left(1 + \frac{K_s V(t)}{2}\right)^2 \qquad \text{Standard (constriction) blocking}$$

where Q is the volumetric flow rate at time t, Q_0 is the initial volumetric flow rate, K_i is the intermediate blocking parameter, K_b is the complete blocking parameter, K_s is the standard blocking parameter, and $V(t)$ is the filtrate volume at time t. These formulae are recast for constant-flux filtration in Appendix C.

$$R(v) = R_0 e^{\sigma_i v} \qquad \text{Intermediate blocking}$$

$$R(v) = R_0 \frac{1}{1 - \sigma_c v} \qquad \text{Complete pore blocking}$$

$$R(v) = R_0 (1 - \psi v)^{-2} \qquad \text{Standard (constriction) blocking}$$

where $R(v)$ is filter resistance at volume filtered per unit area, v is volume filtered per unit filter area, σ is blocked area per unit filtrate volume, and ψ is the standard blocking parameter. Curve fits were developed using the first and last data point before a backpulse, with the backpulses serving as the cutoff for each data set.

Figure 4.6 and Figure 4.7 present the test data of the first backpulse subset via plots of filter resistance as a function of volume filtered normalized to filter area. Plots for additional backpulses are found in Appendix B. Analysis of the curve fits indicates that the "complete blocking" mechanism fits the majority of these resistance curves. As the filter fouled and prior to the filter cleaning, the fits varied between standard and complete blocking.

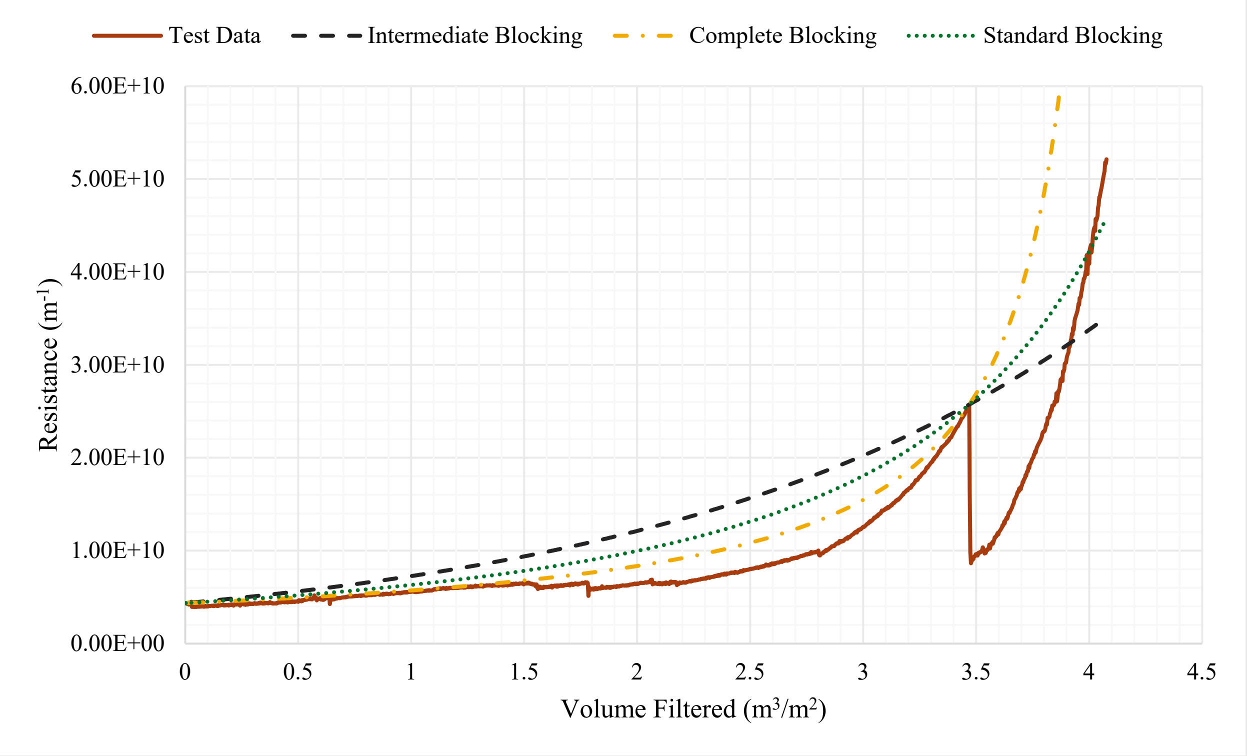

Figure 4.6. Fit to test data prior to slough using classical fouling mechanisms.

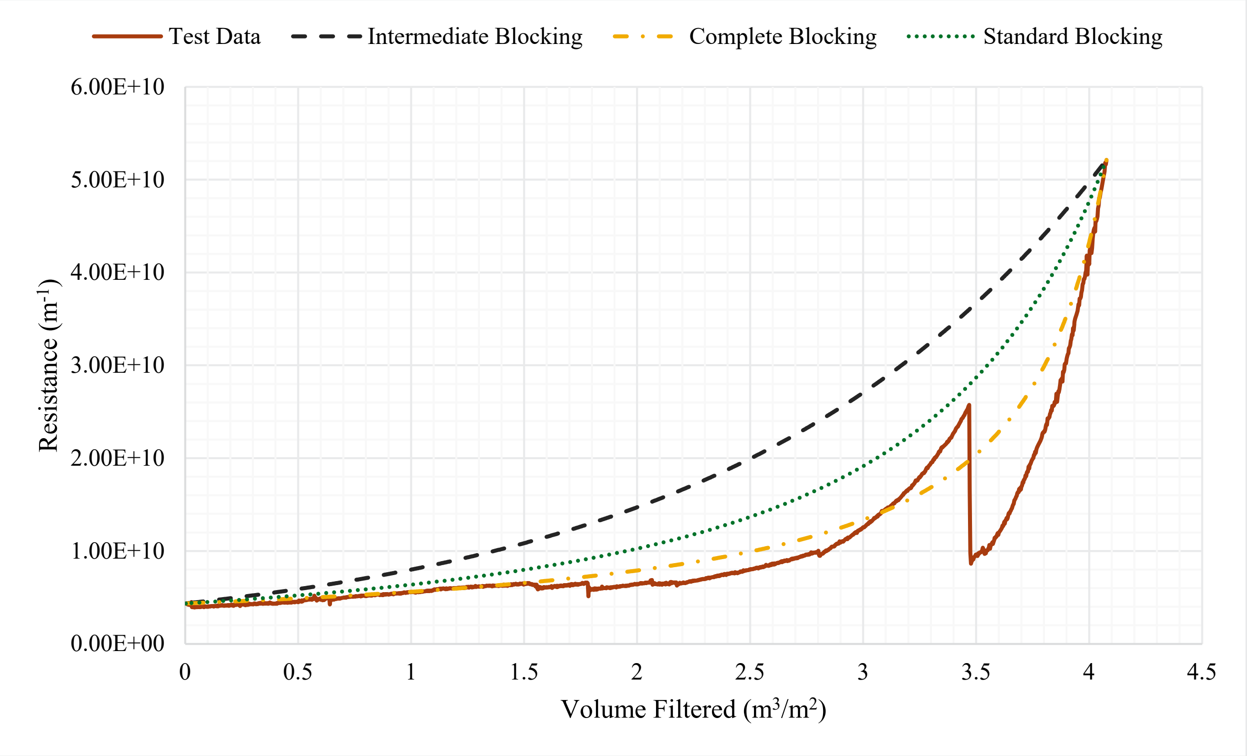

Figure 4.7. Fit to test data prior to backpulse 1 using classical fouling mechanisms.

In Figure 4.8, the initial differential filter pressure rises linearly after each successive backpulse. It can also be noted that while cleaning the filter did well to restore initial differential filter pressure, Figure 4.9 shows that the blocking parameter increases at a faster rate after cleaning, indicating that the filter was fouling quicker after the cleaning operation than before. This plot also highlights the rise in initial transmembrane pressure observed after each subsequent backpulse and better illustrates the depth fouling of the filter pores and how these small solids are difficult to dislodge via backpulse.

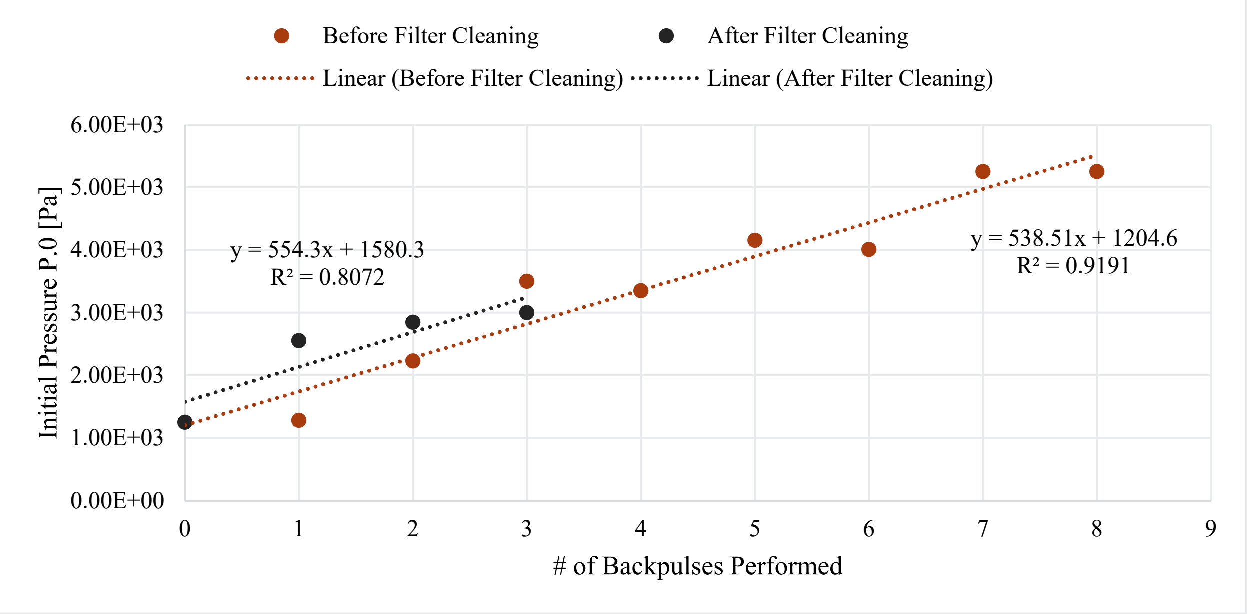

Figure 4.8 Initial differential pressure for backpulses performed before and after filter cleaning.

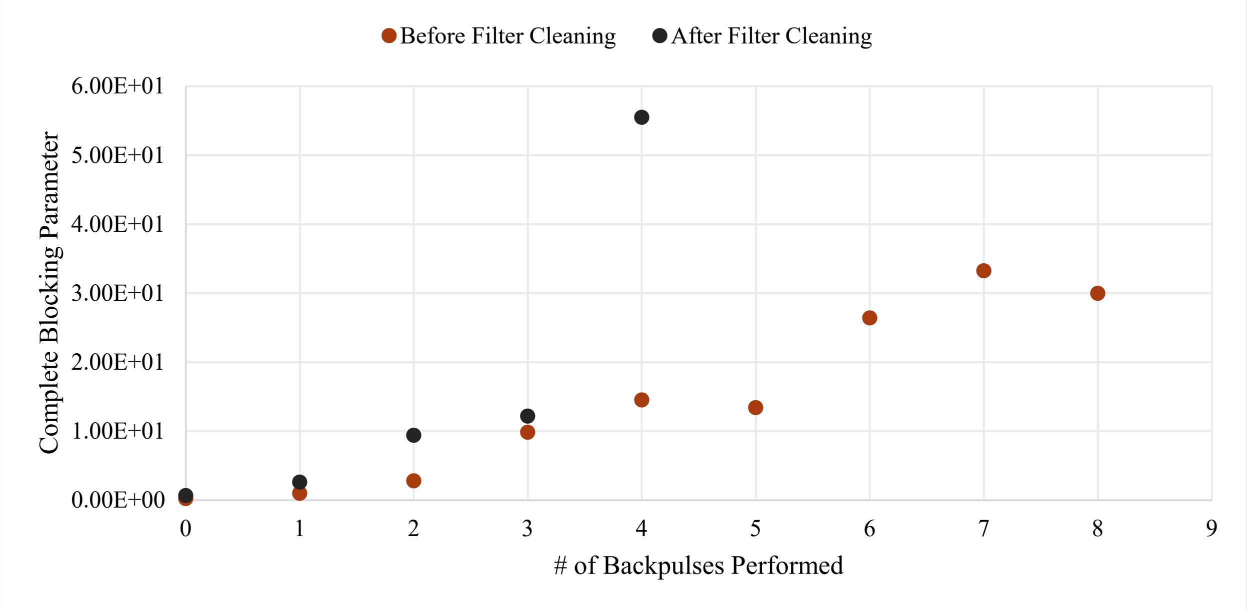

Figure 4.9. Complete blocking parameter for backpulses performed before and after filter cleaning.

4.3 Final CWF

At the conclusion of AP-107 filtration, a second cleaning was performed, and the CWF was measured again. Figure 4.10 compares this final CWF with the initial CWF. The filter differential pressure was lower during the final CWF, indicating that the second cleaning dissolved much of the solids that were deposited on the filter. It is unclear whether this cleaning would result in an increase in the time between backpulses if additional AP-107 were to be filtered; the first cleaning (during AP-107 filtration) had shown significant improvement in the initial resistance, but that improvement was short-lived and frequent backpulses were required during the remainder of the filtration.

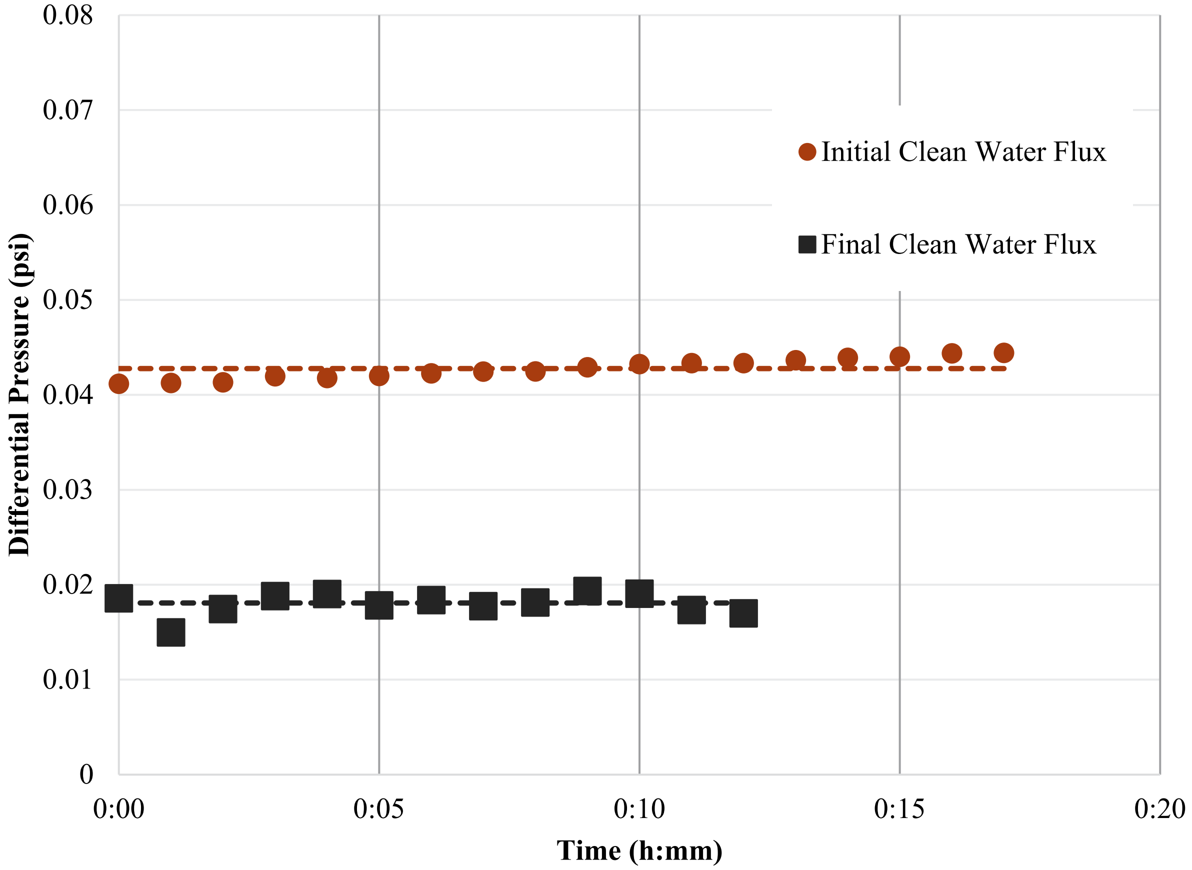

Figure 4.10. Initial and final clean water flux.

4.4 Analytical Results

Total alpha analysis (alpha energy analysis, AEA) was conducted on three permeate samples to determine the transuranic (TRU) content of the filtered permeate. The analysis results are given in Table 4.3 and show no gross breakthrough of TRU components that aren't already soluble, between the three permeate samples taken. All samples remained below the 0.1 µCi/g threshold defining TRU waste per DOE M 435.1-1, Radioactive Waste Management Manual.

Table 4.3. AEA for permeate samples.

Analysis Method	Sample ID	(µCi/mL)	(µCi/g)
Total alpha analysis	Permeate sample 1	8.47E-04	6.66E-04
	Permeate sample 2	1.22E-03	9.60E-04
	Permeate sample 3	9.27E-04	3.26E-04

4.5 Microscopy Solids Analysis

Materials collected from backpulse events were submitted for examination by scanning electron microscopy (SEM) and higher-resolution scanning transmission electron microscopy (STEM). A full report of the particle analysis can be found in Appendix E. The SEM analysis revealed a large distribution of particles sizes with some particles close to 0.5 mm in diameter, which were identified as sodium phosphates. A series of images of the material were collected with backscattered electron imaging and X-ray energy dispersive spectroscopy (EDS) mapping, and spot analysis was performed to understand the types of phases present in the material (see Figure 4.11 for examples of the morphologies in the specimen).

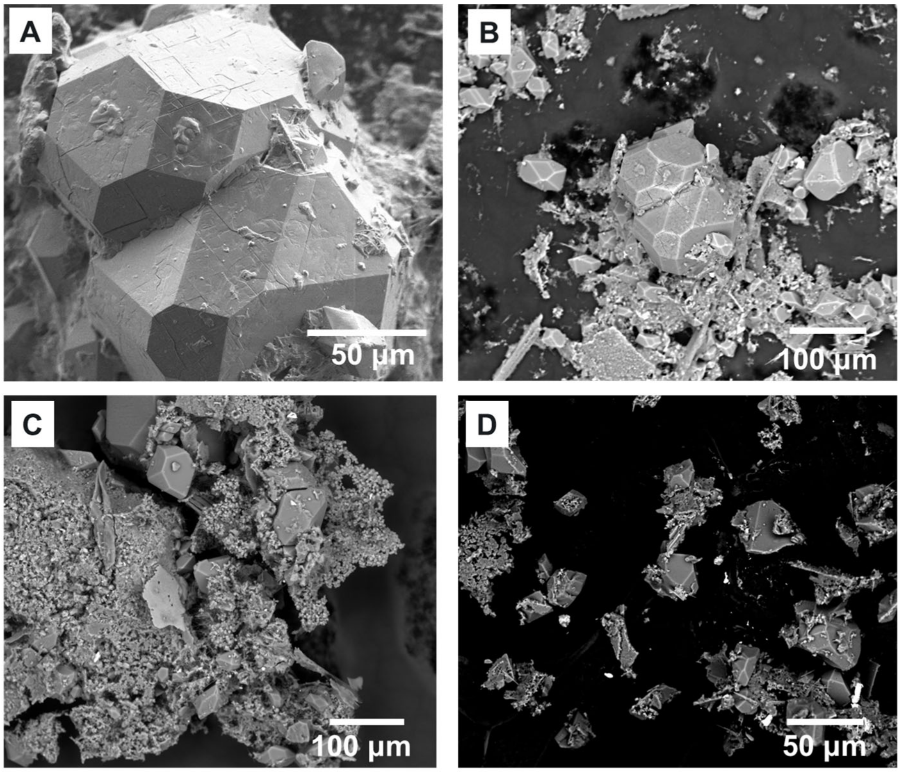

Figure 4.11. SEM images of large particles found in the backpulse concentrate.

The SEM image and elemental maps in Figure 4.12 reveal several readily identified phases, including a sodium phosphate, calcite-like phase; iron oxides; and aluminum oxides. SEM-EDS images of the calcite and phosphate phases shown in Figure 4.12 are displayed in Figure 4.13. The match of the sodium phosphate dodecahydrate to the EDS experimental result supports the assignment of this phase. Furthermore, there was no evidence of the presence of fluorine in the phase. The copper "particles" were artifacts from the transmission electron microscopy (TEM) instrument grid from sample preparation. Both Al-oxides and Al-silicates were present, as were several transition metal oxides (Fe, Cr, and Ni) and the calcite phase.

Using automated particle analysis, a series of compositional ternary diagrams were developed for some major elements to provide an overview of the compositions in the material; these are given in Table 4.4.

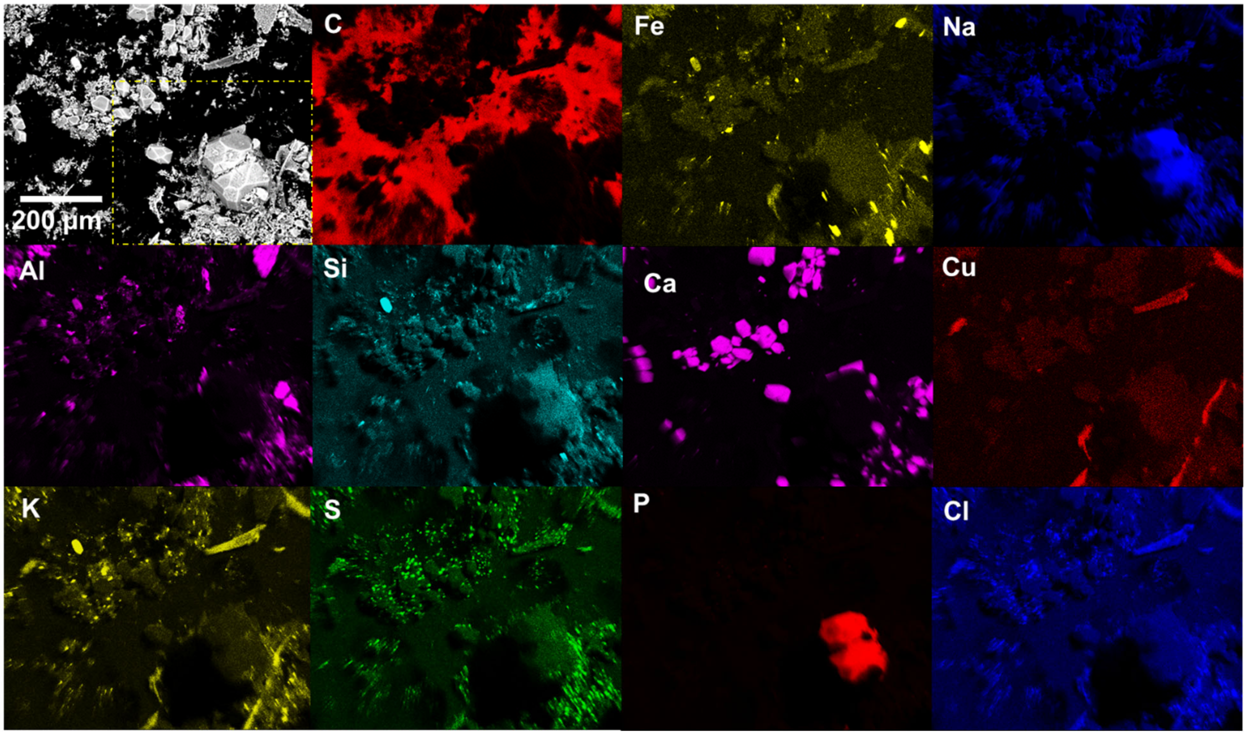

Figure 4.12. SEM-EDS elemental maps of the large particles found in the backpulse concentrate showing Ca-rich, phosphate, and Al-particles. The yellow outline in the secondary electron image (upper-left corner, above) is the same region as in Figure 4.11B and confirms that this large particle is sodium phosphate.

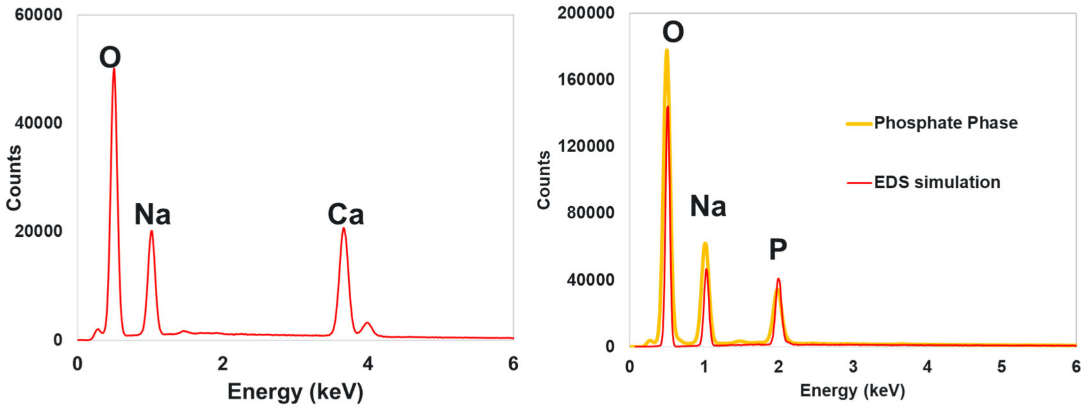

Figure 4.13. EDS spectra of calcite phase (left) and phosphate phase (right).

Table 4.4. Summary of particle classes and their average compositions (element wt%).

Class	CK	OK	NaK	MgK	AlK	SiK	PK	SK	ClK	KK	CaK	TiK	FeK	NiK
Nitrite/Nitrate	6.8	47.0	38.7	0.1	4.0	0.1	0.1	0.5	0.3	0.3	0.3	0.1	0.4	0.3
Gibbsite/Al-Oxide	1.2	55.8	10.8	0.1	29.3	0.1	0.0	0.1	0.3	0.4	0.4	0.1	0.4	0.3
Oxalate (C and O)	36.9	44.7	2.7	1.5	1.7	1.4	1.0	1.0	1.0	0.8	1.0	0.7	0.8	0.9
Na-Aluminate/Dawsonite	11.4	50.9	19.2	0.2	13.4	0.6	0.2	0.2	0.4	0.4	0.5	0.2	0.4	0.4
Calcite	7.5	52.4	17.9	0.4	1.5	0.5	0.3	0.4	0.4	0.5	14.8	0.3	0.6	0.5
Na-Phosphate	6.7	44.7	33.6	0.3	1.8	0.4	7.7	0.4	0.5	0.5	0.4	0.3	0.4	0.5
Metal Oxides/Hematite	20.1	41.7	13.1	1.0	5.3	1.3	0.9	0.9	1.1	1.2	1.4	0.9	3.1	1.9
Na/Gaylussite	22.2	47.0	24.5	0.4	1.8	0.3	0.3	0.3	0.4	0.3	0.3	0.2	0.2	0.3
Unknown	10.7	11.9	6.2	0.9	3.2	1.7	1.8	2.4	2.9	3.3	5.0	3.6	6.3	5.8

Using *in situ* liquid cells, particles were examined to determine the effect of drying the Hanford waste particles prior to imaging them in the electron microscope. The backpulse solids were dissolved using 0.1 M NaOH. A cap containing a few drops of 0.1 M NaOH was placed over the top of the SEM instrument mount, creating a chamber where the sample was exposed to vapor. The intention was not to dissolve the particle directly, but merely to look at partial dissolution. Figure 4.14 shows the result of this technique on a sodium phosphate particle. The image shows the same phase before and after this process. The phosphate had undergone extensive pitting and dissolution. A few smaller particles were either completely dissolved or transported away. Some particles appeared to be unaffected by this process. Following the dissolution treatment, the particles appeared to form an amalgam, but the phosphate component appeared to be completely dissolved.

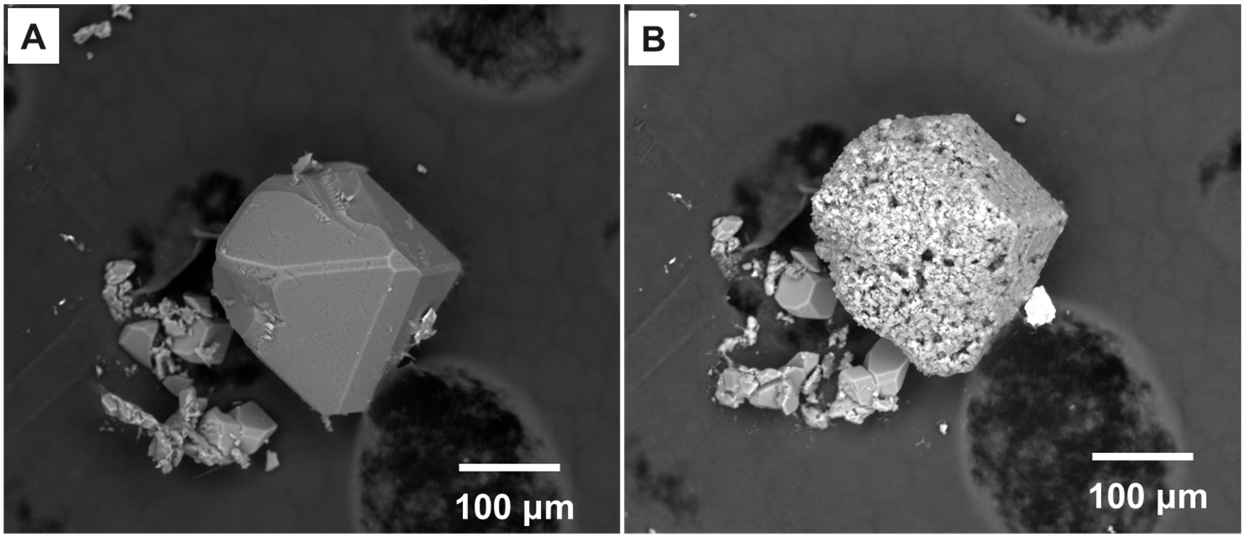

Figure 4.14. Phosphate particle from as-received AP-107 sample and following exposure with 0.1 M NaOH “vapor.” The large phosphate particle has undergone corrosion and pitting but the smaller calcite particles have not been affected.

5.0 Conclusions

Testing was performed to assess the impact of sampling tank AP-107 at a lower height in the tank and the effect of a lower operating temperature (16 °C) on filter performance. The testing results demonstrated significantly faster filter fouling than was seen in prior testing that used a sample collected higher in the tank and tested at a higher temperature (25 °C). The solids that were present in the current sample caused significant depth fouling that could not be alleviated with a simple backpulse. Additional effort was required to dissolve these solids. Post cleaning, the filter resistance was effectively restored to initial conditions as the initial transmembrane pressure was restored to original levels. However, resumed processing of the AP-107 feed at 16 °C continued to result in an increased rate of filter resistance.

The source of these solids is not fully understood. They may have been associated with the lower sample collection depth or the lower processing temperature. However, the fact that the bulk of the solids readily dissolved with water addition suggests that they are perhaps more likely attributable to formation due to temperature changes. Formation of solids due to temperature change is driven by changes in solubility. Dilution with water would effectively reverse the impact of decreasing temperature. Thus, the result that these solids dissolve with water addition suggests temperature as a primary driver for the solids formation. Therefore, one method to alleviate this type of filter fouling may be to increase the operating temperature of the TSCR filtration system.

6.0 References

Allred JR, JGH Geeting, AM Westesen, EC Buck, and RA Peterson. 2020. *Fiscal Year 2020 Filtration of Hanford Tank Waste 241-AP-105*. PNNL-30485, Rev. 0 (RPT-DFTP-021, Rev. 0). Pacific Northwest National Laboratory, Richland, Washington.

ASME. 2000. *Quality Assurance Requirements for Nuclear Facility Applications*. NQA-1-2000. The American Society of Mechanical Engineers, New York, New York.

ASME. 2008. *Quality Assurance Requirements for Nuclear Facility Applications*. NQA-1-2008. The American Society of Mechanical Engineers, New York, New York.

ASME. 2009. *Addenda to ASME NQA-1-2008*. NQA-1a-2009. The American Society of Mechanical Engineers, New York, New York.

Daniel RC, CA Burns, RA Peterson, VL Saldana, and NL Canfield. 2020. *Testing of an AP-105 Precipitation Simulant.* PNNL-29690, Rev. 0 (RPT-DFTP-016, Rev. 0). Pacific Northwest National Laboratory, Richland, Washington.

Geeting JGH, JR Allred, AM Rovira, and RA Peterson. 2019. *Fiscal Year 2019 Filtration of Hanford Tank AP-107 Supernatant*. PNNL-28780, Rev. 0 (RPT-DFTP-015, Rev. 0). Pacific Northwest National Laboratory, Richland, Washington.

Geeting JGH, AM Rovira, JR Allred, RW Shimskey, CA Burns, and RA Peterson. 2018a. *Filtration of Hanford Tank AP-107 Supernatant*. PNNL-27638 (RPT-DFTP-009, Rev. 0). Pacific Northwest National Laboratory, Richland, Washington.

Geeting JGH, JR Allred, AM Rovira, RW Shimskey, CA Burns, and RA Peterson. 2018b. *Crossflow Filtration of Hanford Tank AP-105 Supernatant*. PNNL-27085 (RPT-DFTP-005, Rev. 0). Pacific Northwest National Laboratory, Richland, Washington.

Gerber MS. 1992. *Legend and Legacy: Fifty Years of Defense Production at the Hanford Site*. WHC-MR-0293, Rev. 2. Westinghouse Hanford Company, Richland, Washington. doi:10.2172/10144167

Hermia J. 1982. "Constant Pressure Blocking Filtration Laws – Application to Power-Law Non-Newtonian Fluids." *Transactions of the Institution of Chemical Engineers* 60(3):183-187.

Appendix A – BDEF Piping and Instrumentation Diagram

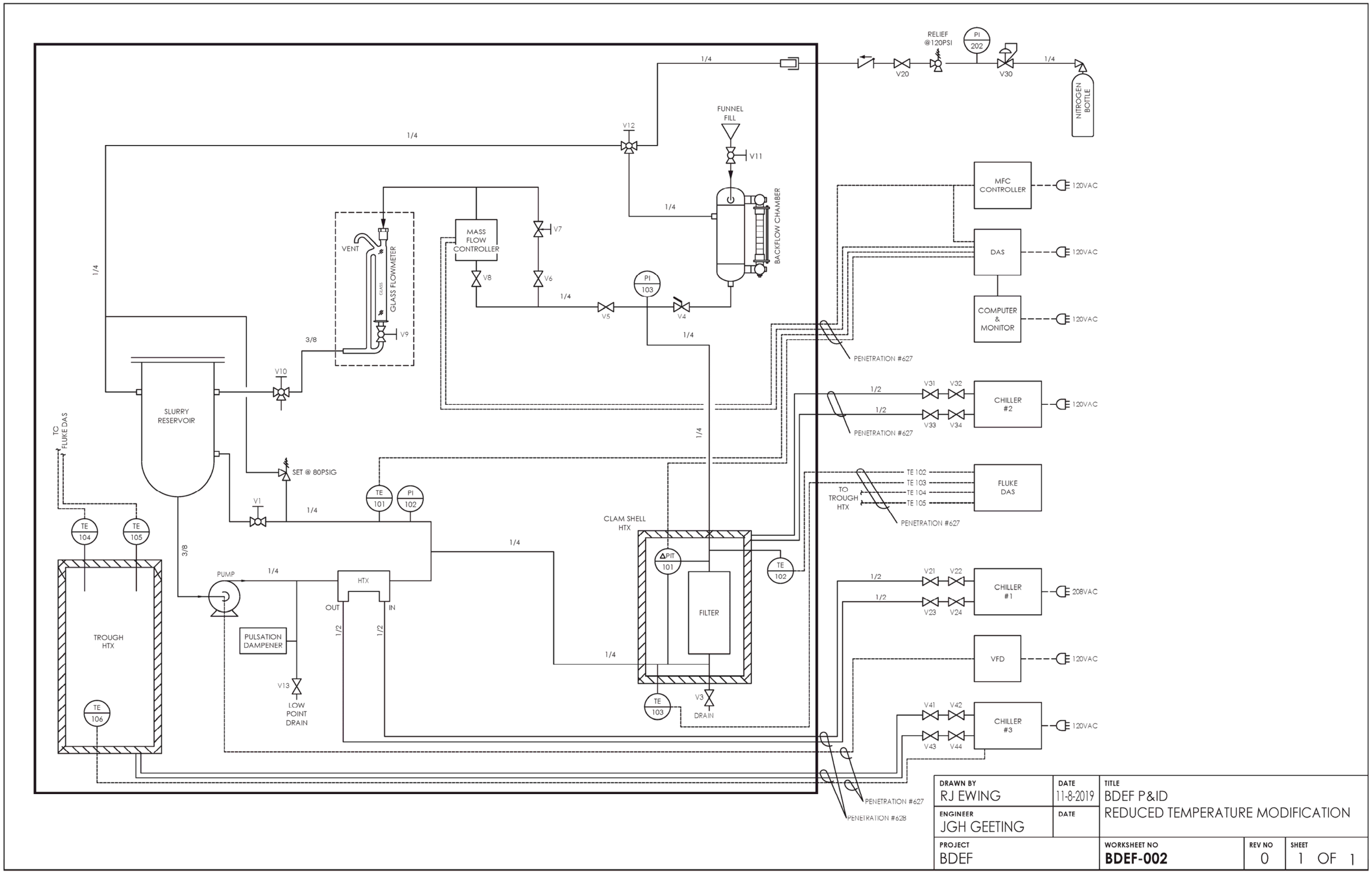

Figure A.1. BDEF Piping and Instrumentation Diagram.

Appendix B – Backpulse Curve Fits

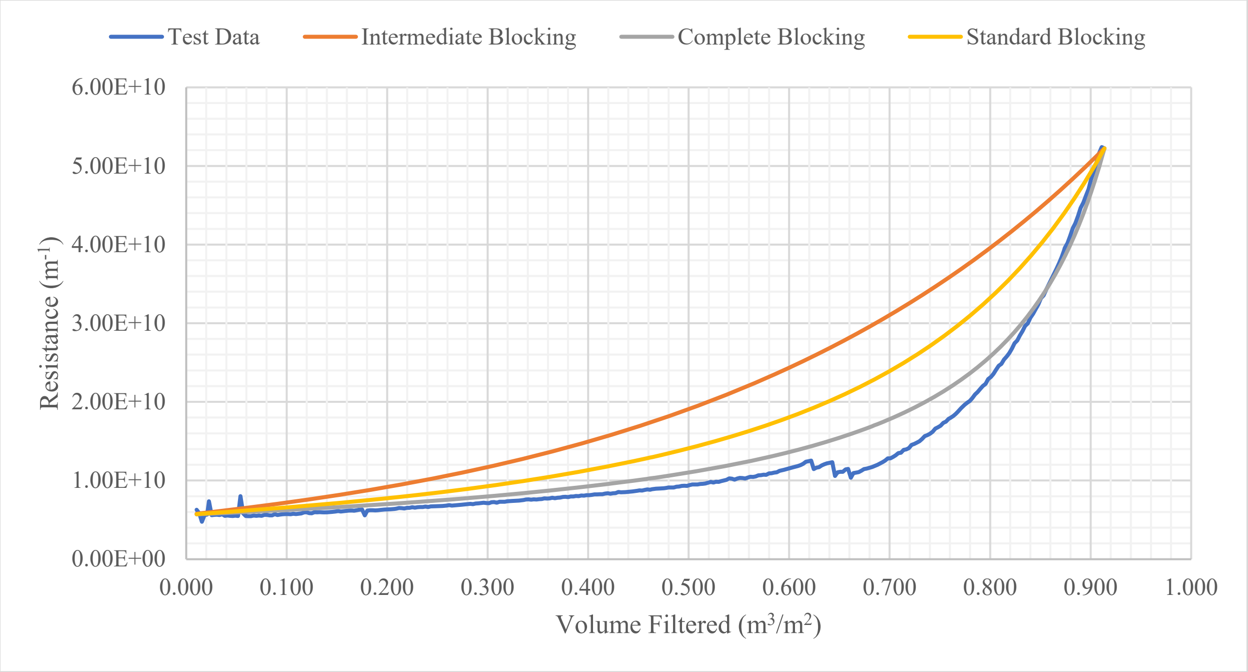

Figure B.1. Fit to test data prior to backpulse 2 using classical fouling mechanisms.

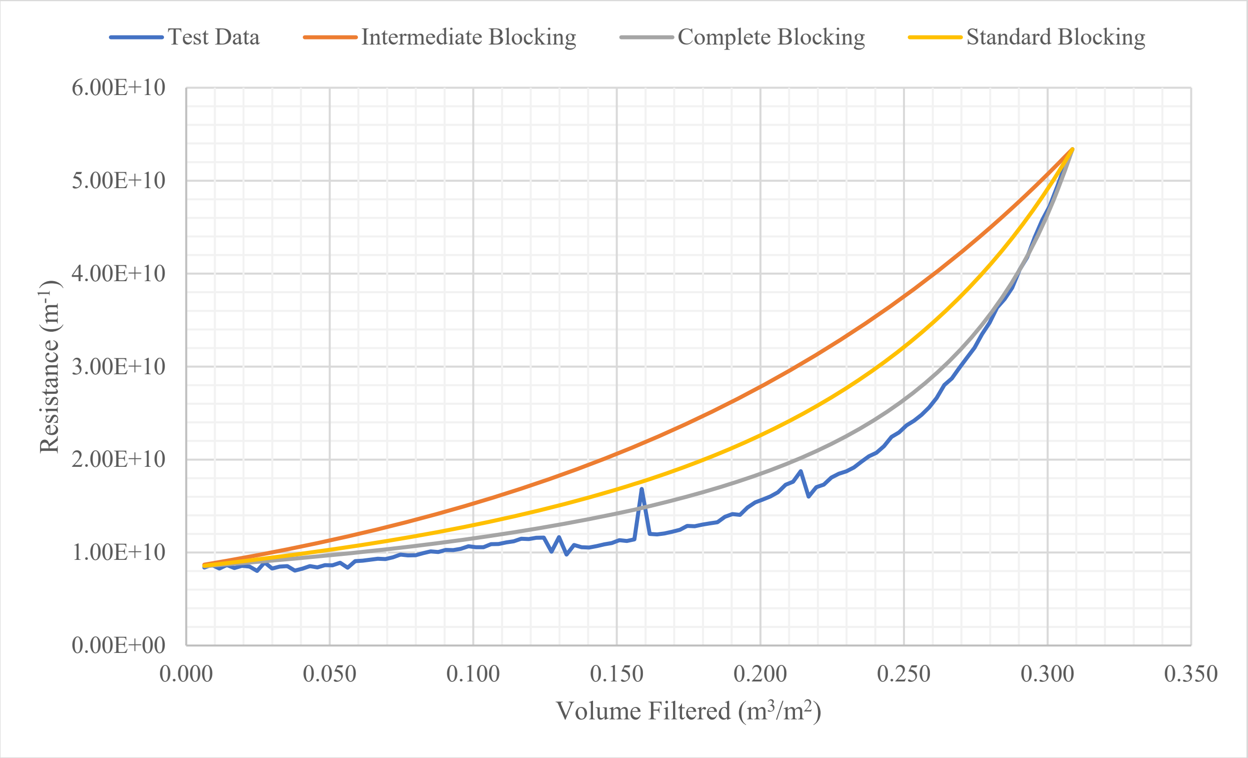

Figure B.2. Fit to test data prior to backpulse 3 using classical fouling mechanisms.

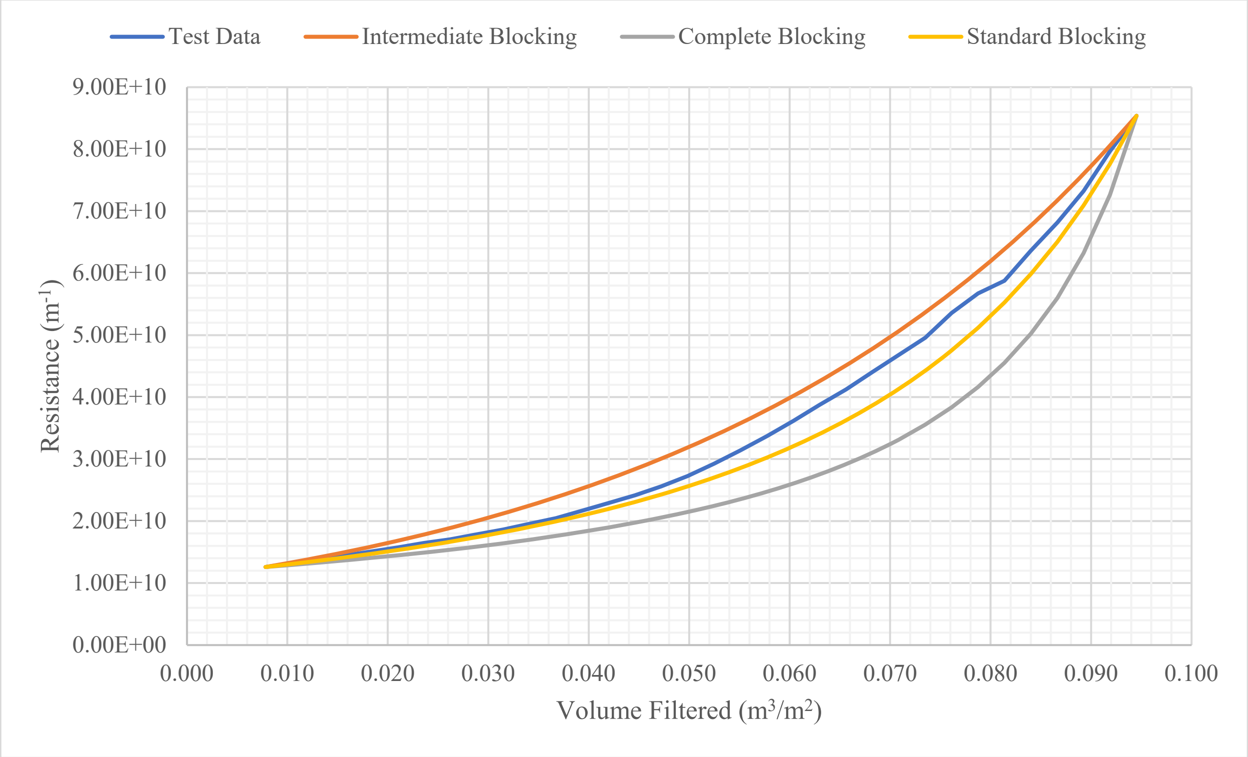

Figure B.3. Fit to test data prior to backpulse 4 using classical fouling mechanisms.

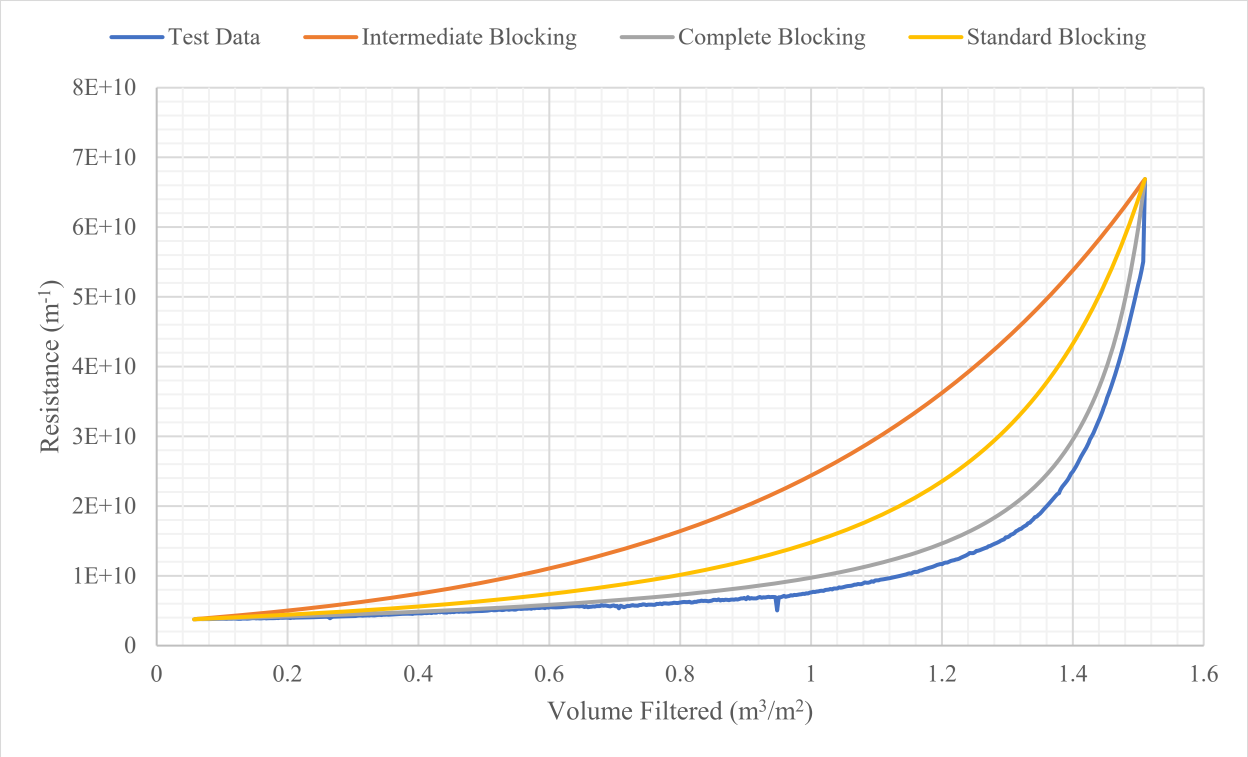

Figure B.4. Fit to test data prior to backpulse 10 using classical fouling mechanisms.

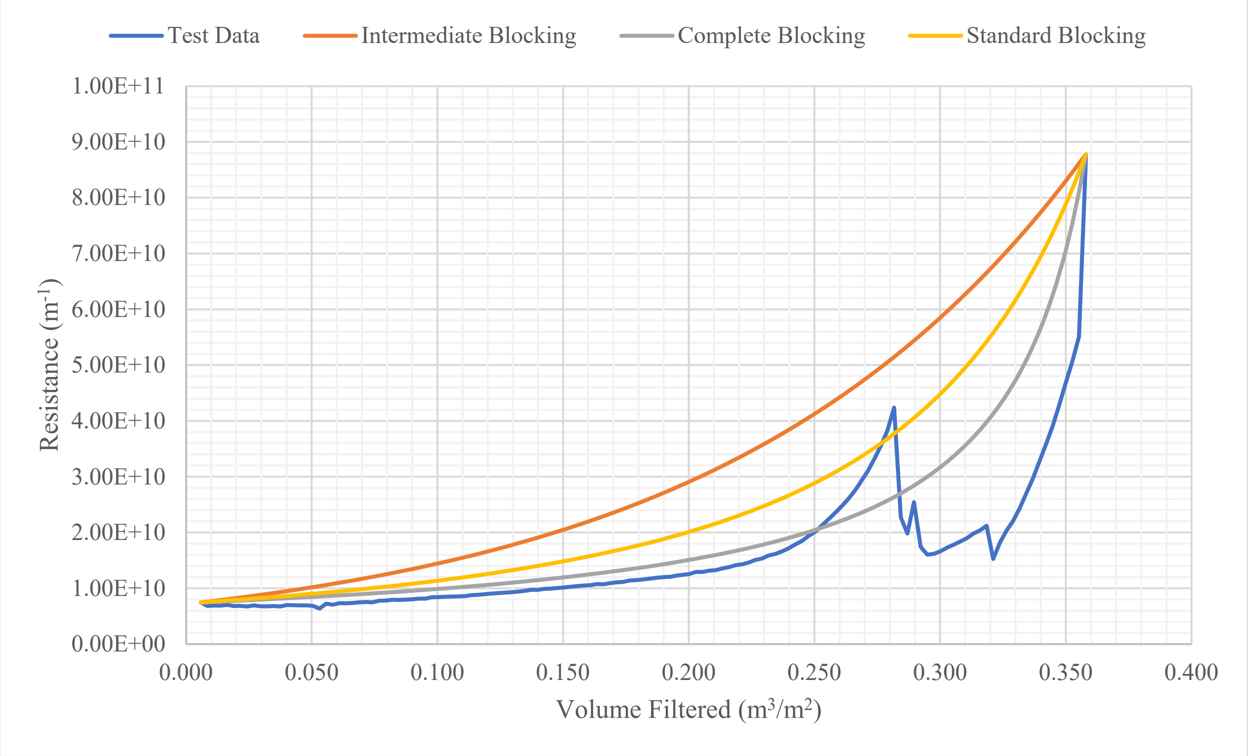

Figure B.5. Fit to test data prior to backpulse 11 using classical fouling mechanisms.

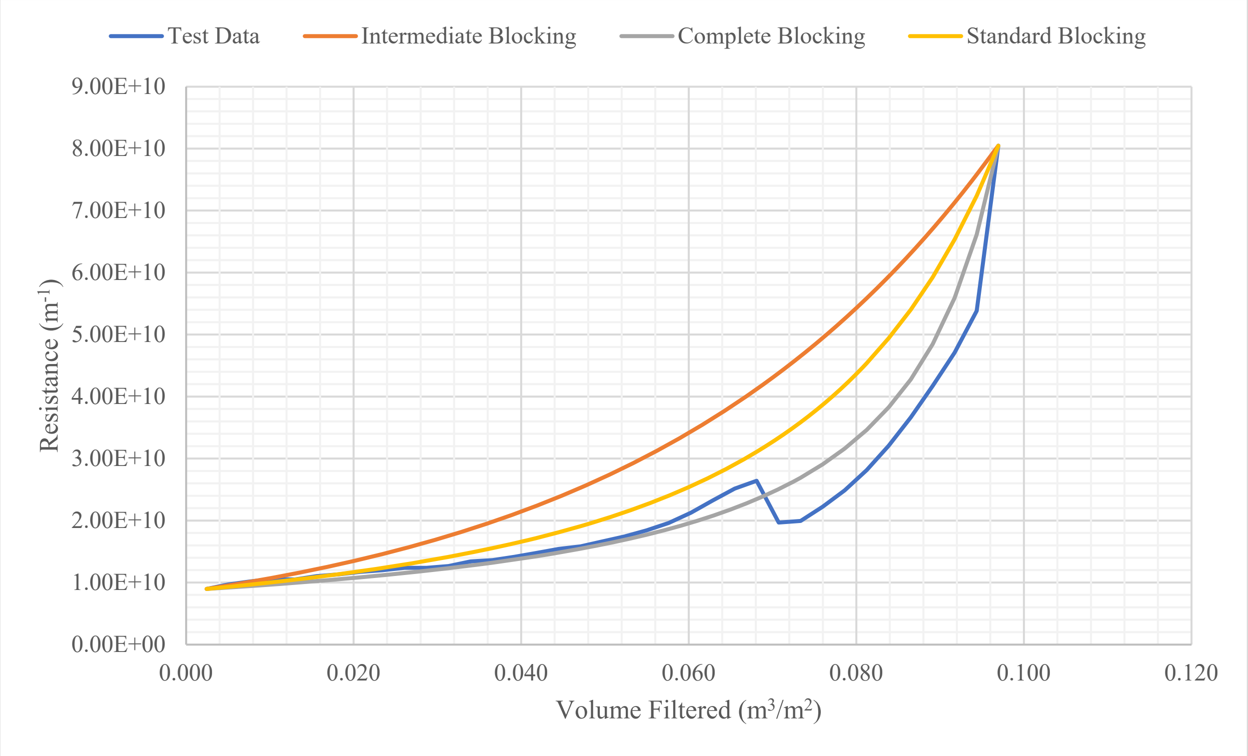

Figure B.6. Fit to test data prior to backpulse 12 using classical fouling mechanisms.

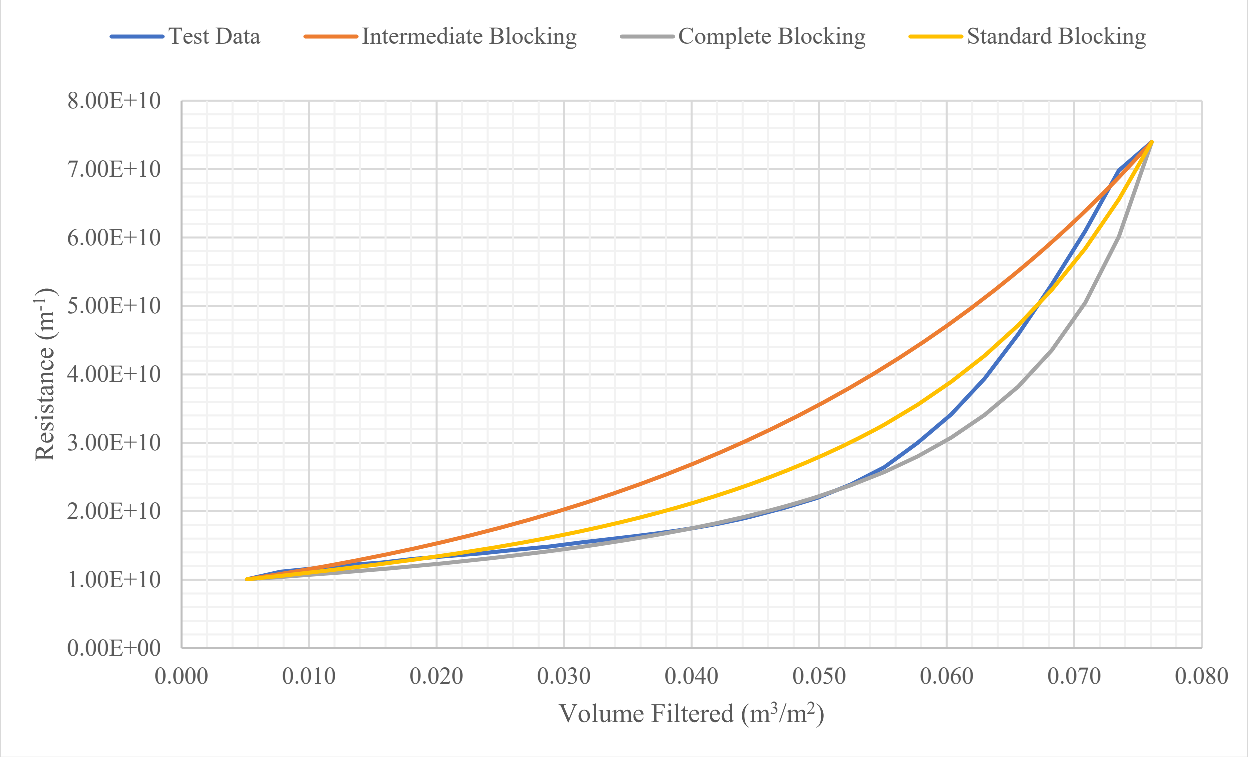

Figure B.7. Fit to test data prior to backpulse 13 using classical fouling mechanisms.

Table B.1. Blocking law model parameters.

Backpulse #	R.0 [1/m]	P.0 [Pa]$^{(a)}$	Intermediate Blocking σ	Complete Blocking σ	Standard Blocking ψ	Best Fit
1.a	4.35E+09	1.04E+03	5.13E-01	2.40E-01	1.70E-01	Complete blocking
1.b	4.35E+09	1.04E+03	6.10E-01	2.25E-01	1.75E-01	Complete blocking
2	5.64E+09	1.28E+03	2.46E+00	9.88E-01	7.43E-01	Complete blocking
3	8.38E+09	2.23E+03	6.13E+00	2.79E+00	2.00E+00	Complete blocking
4	1.26E+10	3.50E+03	2.21E+01	9.83E+00	7.10E+00	Standard blocking
5	1.27E+10	3.35E+03	2.74E+01	1.45E+01	9.76E+00	N/A
6	1.56E+10	4.15E+03	1.59E+01	1.34E+01	7.30E+00	N/A
7	4.06E+10	4.01E+03	4.14E+01	2.64E+01	1.64E+01	N/A
8	5.68E+10	5.25E+03	4.71E+01	3.32E+01	1.97E+01	N/A
9	2.12E+10	5.25E+03	6.53E+01	3.00E+01	2.14E+01	N/A
10	3.77E+09	1.06E+03	1.98E+00	6.49E-01	5.25E-01	Complete blocking
11	7.47E+09	1.25E+03	7.00E+00	2.60E+00	2.01E+00	Complete blocking
12	8.97E+09	2.55E+03	2.32E+01	9.40E+00	7.05E+00	Complete blocking
13	1.01E+10	2.85E+03	2.81E+01	1.22E+01	8.89E+00	Complete blocking
14	2.25E+10	3.00E+03	9.91E+01	5.55E+01	3.64E+01	N/A

(a) P.0 is the initial transmembrane pressure observed at the beginning of the backpulse data set.

Appendix C – Adjusting Hermia Laws for Constant Flux Filtration

Symbols

A	filter surface area [m^2]
A_0	clean filter surface area [m^2]
C	volume of particles deposited by unit volume of filtrate [dimensionless]
j	filter flux [m^3/m^2/s]
j_0	clean filter flux [m^3/m^2/s]
k	blocking parameter [dimensionless]
L	pore length [m]
N	number of pores in filter [dimensionless]
p	transmembrane pressure [Pa]
p_0	clean filter transmembrane pressure [Pa] (defined only for a given Q or j)
Q	volumetric flow rate [m^3/s]
Q_0	clean filter volumetric flow rate [m^3/s] (defined only for a given p)
r	radius of pore [m]
r_0	radius of pore in clean filter [m]
R	filtration resistance [1/m]
R_0	clean filter resistance [1/m]
t	filtration time [s]
V	volume filtered [m^3]
Λ	scaled unblocked filter area
μ	fluid viscosity (Newtonian dynamic viscosity) [N s/m^2]
ν	volume filtered per unit filter area [m^3/m^2]
σ	blocked area per unit filtrate volume [m^{-1}]
ψ	standard blocking parameter (m^{-1})
ω	scaled resistance

We seek to derive Hermia's filtration laws (Hermia 1982) for constant-pressure filtration into equivalent laws for constant-flux filtration. Hermia's form relies on Darcy's law of

$$j = \frac{Q}{A} = \frac{p}{\mu R}$$

Hermia's filtration forms have the basic relationship

$$\frac{d^2t}{dV^2} = k_n \left(\frac{dt}{dV}\right)^n$$

The filter flow rate form of this equation is

$$\frac{dQ}{dV} = -k_n Q^{2-n}$$

It can be shown that for a reduced resistance defined by

$$\omega = \frac{R}{R_0}$$

We can write

$$\frac{d\omega}{d\nu} = \kappa_n \omega^n \text{ with } \kappa_n = \left(\frac{A_0}{Q_0^{n-1}}\right) k_n$$

where $\nu = V/A_0$ and Q_0 is the clean filter flow rate (defined only for constant-pressure filtration). The individual forms and proof of this relationship are derived below.

Complete Blocking (n=2)

For complete blocking, Hermia assumes any change in filter performance results from pore blocking. Pore blocking is treated as a loss of area for flow such that

$$A = A_0 - \sigma V$$

where A_0 is the clean filer surface area

$$\Lambda = \frac{A}{A_0} = 1 - \sigma v$$

where v is the specific volume filtered

$$v = \frac{V}{A_0}$$

From Darcy's law, we write

$$p = \frac{\mu R_0 j_0}{\Lambda}$$

where the flux $j_0 = \frac{Q}{A_0} = const$ and R_0 is the baseline filter resistance.

$$p_0 = \mu R_0 j_0$$

So,

$$p = \frac{p_0}{\Lambda} = \frac{p_0}{1 - \sigma v}$$

We could also interpret this as an increase in filter resistance. We define

$$R = \frac{p}{\mu j_0}$$

Thus,

$$R = \frac{R_0}{\Lambda} = \frac{R_0}{1 - \sigma v}$$

Defining the relative resistance as

$$\omega = \frac{R}{R_0}$$

we have

$$\omega = \frac{1}{\Lambda} = \frac{1}{1 - \sigma v}$$

then we have

$$\frac{d\omega}{dv} = \sigma\omega^2$$

Intermediate Blocking (n=1)

For intermediate blocking we have

$$\frac{dA}{dt} = -\sigma\frac{Q}{A_0}A$$

So,

$$\frac{1}{A}dA = -\sigma j_0 dt$$

$$ln\left(\frac{A}{A_0}\right) = -\sigma j_0 t$$

$$\Lambda = e^{-\sigma v}$$

Since this is an area problem, we again have

$$\omega = \frac{1}{\Lambda} = e^{\sigma v}$$

Thus,

$$\frac{d\omega}{dv} = \sigma\omega$$

Standard Blocking (n=3/2)

Standard blocking as in Hermia we have pore radius r constriction via deposition:

$$r^2 = r_0^2 - \frac{CV}{\pi N * L}\left(\frac{r}{r_0}\right)^2 = 1 - \frac{CV}{\pi N * r_0^2 L}$$

And per Hermia we define

$$A_0 = \pi N * r_0^2$$

So,

$$\left(\frac{r}{r_0}\right)^2 = 1 - \frac{CV}{A_0 L}$$

and Poiseuille's law is

$$p = \frac{8\mu QL}{\pi N * r^4}$$

At constant Q, we have

$$\frac{p}{p_0} = \left(\frac{r_0}{r}\right)^4 = \left(1 - \frac{C}{L}\nu\right)^{-2}$$

and can readily show that

$$\omega = \frac{p}{p_0}$$

Thus,

$$\omega = \left(1 - \frac{C}{L}\nu\right)^{-2}$$

and,

$$\frac{d\omega}{d\nu} = \frac{2C}{L}\left(1 - \frac{C}{L}\nu\right)^{-3}$$

or,

$$\frac{d\omega}{d\nu} = \left(\frac{2C}{L}\right)\omega^{\frac{3}{2}}$$

The blocking parameter can be defined as

$$\psi = \frac{C}{L}$$

<u>Cake Filtration (n=0)</u>

From Hermia, we have

$$\begin{aligned} \omega &= 1 + K_c Q_0 V \\ &= 1 + K_c Q_0 A_0 \nu \end{aligned}$$

Therefore,

$$\frac{d\omega}{dv} = K_c Q_0 A_0$$

Summary

We propose a scaled resistance law where

$$\omega = \frac{R}{R_0}\, and v = \frac{V}{A_0}$$

such that

$$\frac{d\omega}{dv} = \kappa_n \omega^n$$

Note that scaled resistance is filtration mode agnostic — it can represent fouling in both constant-flux and constant-pressure filtration. For constant-pressure filtration, the scaled resistance can be shown to be

$$\omega = \frac{Q_0}{Q}$$

where Q_0 is the clean filter flow rate and a constant, so

$$Q = \frac{Q_0}{\omega}$$

and

$$\frac{dQ}{dV} = -\frac{Q_0}{\omega^2}\frac{d\omega}{dV}$$

And from Hermia's law and $V = \nu A_0$

$$-k_n Q^{2-n} = -\frac{Q_0}{\omega^2}\frac{dv}{dV}\frac{d\omega}{dv}$$

$$k_n \left(\frac{Q_0}{\omega^2}\right)^{2-n} = \frac{Q_0}{\omega^2}\frac{1}{A_0}\frac{d\omega}{dv}$$

$$Q_0 A_0 k_n \left(\frac{Q_0}{\omega^2}\right)^{2-n} = \left(\frac{Q_0}{\omega^2}\right)^2 \frac{d\omega}{dv}$$

$$Q_0 A_0 k_n = \left(\frac{Q_0}{\omega^2}\right)^n \frac{d\omega}{dv}$$

So,

$$\frac{d\omega}{dv} = (k_n A_0 Q_0^{1-n})\omega^n$$

or

$$\frac{d\omega}{dv} = \kappa_n \omega^n \text{ with } \kappa_n = \left(\frac{A_0}{Q_0^{n-1}}\right) k_n$$

Checks

As a check if we apply Hermia's complete blocking (n=2) form with $K_b = j_0\sigma$ to this formula we find

$$\frac{d\omega}{dv} = \kappa_b \omega^2 \text{ with } \kappa_b = \left(\frac{A_0}{Q_0}\right) j_0\sigma = \sigma$$

which matches the derived form above. If we apply cake filtration (n = 0) form with K_c as the coefficient

$$\frac{d\omega}{dv} = \kappa_c \text{ with } \kappa_c = A_0 Q_0 K_c$$

which again matches the derived form above.

Appendix D – Total Alpha Analysis for Filtration Permeate Samples

Table D.1 provides the total alpha results for the filtration permeate samples taken from the backpulse dead-end filter.

Table D.1. Total alpha analysis for filtration permeate samples.

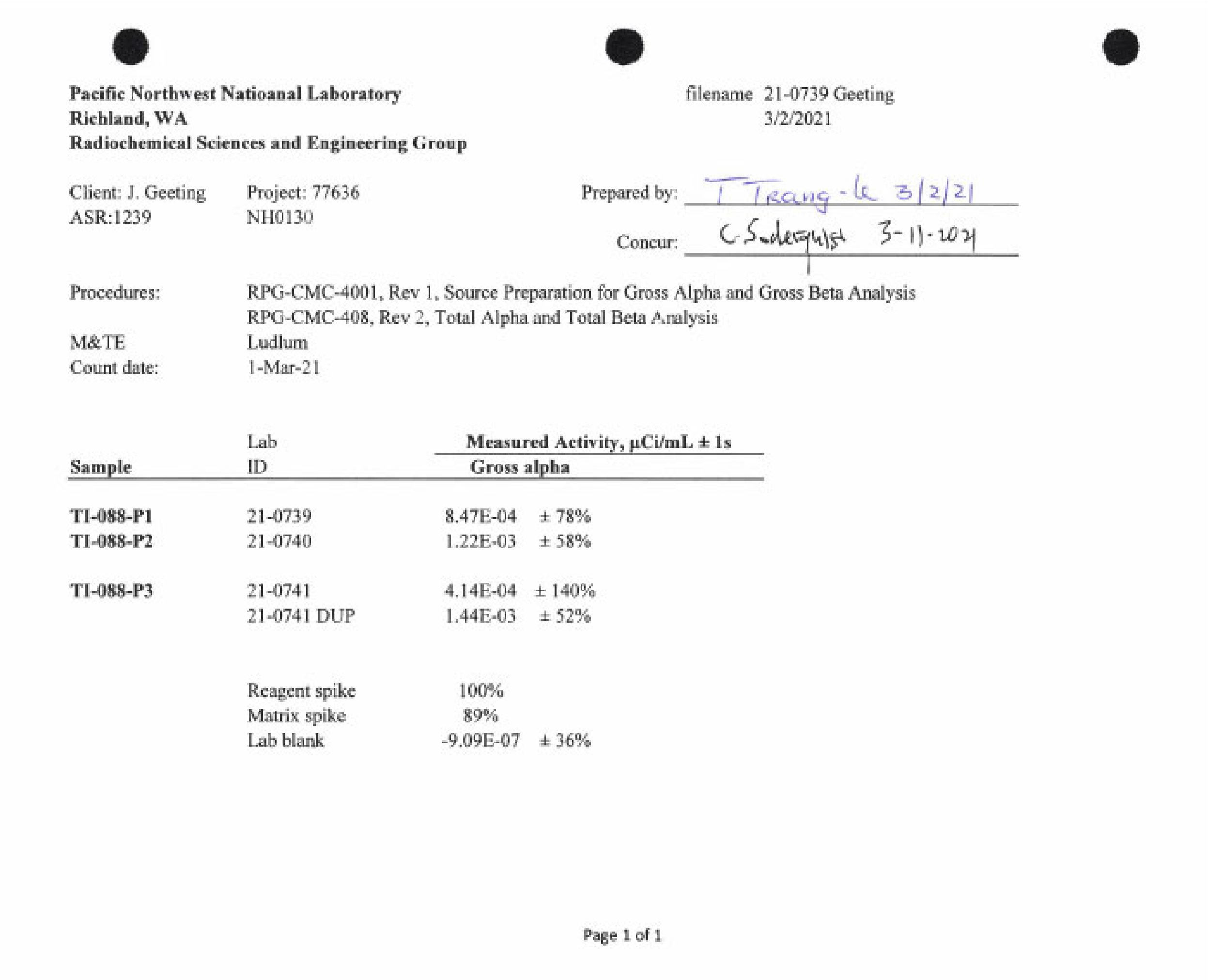

Pacific Northwest Natioanal Laboratory
Richland, WA
Radiochemical Sciences and Engineering Group

filename 21-0739 Geeting
3/2/2021

Client: J. Geeting
ASR:1239

Project: 77636
NH0130

Prepared by: T Trang-Le 3/2/21

Concur: C. Soderquist 3-11-2021

Procedures:	RPG-CMC-4001, Rev 1, Source Preparation for Gross Alpha and Gross Beta Analysis RPG-CMC-408, Rev 2, Total Alpha and Total Beta Analysis
M&TE	Ludlum
Count date:	1-Mar-21

Sample	Lab ID	**Measured Activity, µCi/mL ± 1s** **Gross alpha**	
TI-088-P1	21-0739	8.47E-04	± 78%
TI-088-P2	21-0740	1.22E-03	± 58%
TI-088-P3	21-0741	4.14E-04	± 140%
	21-0741 DUP	1.44E-03	± 52%
	Reagent spike	100%	
	Matrix spike	89%	
	Lab blank	-9.09E-07	± 36%

Page 1 of 1

Appendix E – Backpulse AP-107 Characterization with Scanning Electron Microscopy Coupled with Automated Particle Analysis

E.1 Microscopy Methods

Solids from a backpulse concentrate from Hanford tank waste material representing tank AP-107 were examined with scanning electron microscopy (SEM) and with higher-resolution scanning transmission electron microscopy (STEM). The sample was received as a liquid with suspended solids that had been centrifuged to concentrate the solids (see Figure E.1A). Samples for microscopy analyses were prepared using a filtering method to avoid the formation of evaporative salts.

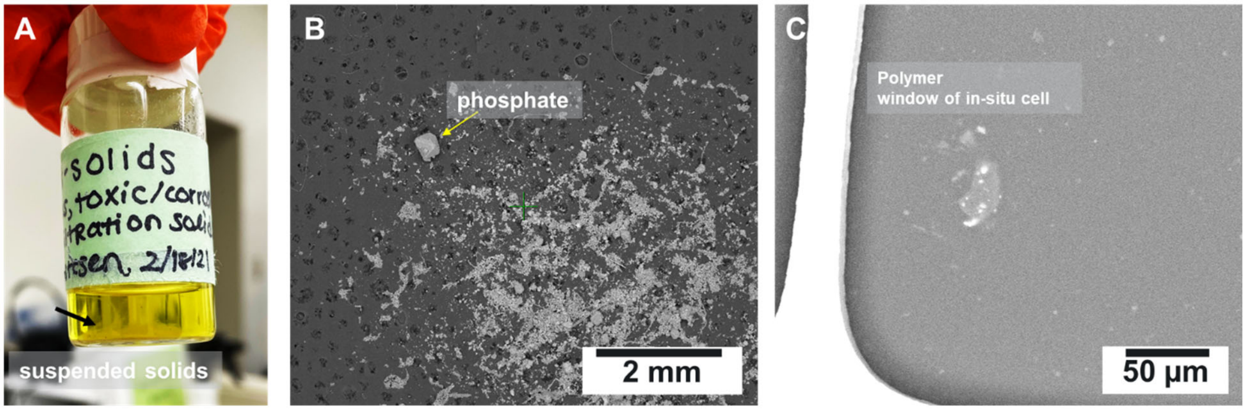

Figure E.1. The analysis of the AP-107 sample (A) used both solids precipitated onto a filter and then applied to standard carbon-tape Al-stub (B) and direct analysis of the “as-received” suspended solids in an *in situ* cell (C) in the electron microscope showing suspended particles.

The samples were examined with an FEI (Thermo-Fisher Inc., Hillsboro, OR) Quanta250 Field Emission Gun (FEG) equipped with a secondary electron (SE) detector and a backscattered electron (BSE) detector and an EDAX (EDAX Inc., NJ) Genesis X-ray energy dispersive spectroscopy (EDS) system. No conductive carbon coat was used on the sample, requiring the instrument to be operated in the low-vacuum mode. The radioactivity in the SEM samples was readily detected with the silicon drift detector (SDD) for EDS analysis (see Figure E.2).

The spectrum shows the X-ray emission from ^{137}Cs decay in the sample that leads to the formation of Ba-K and -L X-rays. To prepare the samples and avoid salts and evaporites forming, the suspended solids were initially pipetted onto a transmission electron microscopy (TEM) instrument grid with a holey carbon film. The film acted as a filter for the particles, allowing most of the solution to wick through. The grid was then applied to an SEM sticky-carbon stub to attach the particles (see Figure E.1B). This technique did sometimes result in some copper micro-particles in the sample but these were ignored in the analysis. An alternative method involved pipetting the solution and suspended solids directly from the “as-received” vial into an *in situ* liquid cell for imaging. The cell used was a wetSEM cell (QuantomiX Inc**.**, Rehovot, Israel), which is designed for imaging particles in solution in the SEM instrument (see Figure E.1C).[1] In this instance, the beam conditions needed to be controlled carefully as even moderate beam currents can easily cause the window to break. EDS analysis was possible, but the count rates were very low. The type analysis with Hanford tank waste required continuous Radiation Protection Technologist (RPT) coverage because of the potential hazard. However, direct imaging of radioactive Hanford waste in solution had not previously been attempted.

In previous work, particles obtained from the waste treatment process or from Hanford particle characterization campaigns[2-5] were analyzed in a manual mode in which the analyst located particles with unique forms or contrast, placed the electron beam on the particle, and collected an EDS spectrum. Identification of a specific phase was based on post-examination of the image and spectral data. This type of manual analysis is accurate but is relatively laborious and time-consuming [6, 7]. In this investigation, the analysis process was automated, enabling information to be provided on thousands of particles. The phases were grouped according to the EDS composition and assigned a classification by the operator. Particles were then classified automatically with a best fit to the modeled composition.

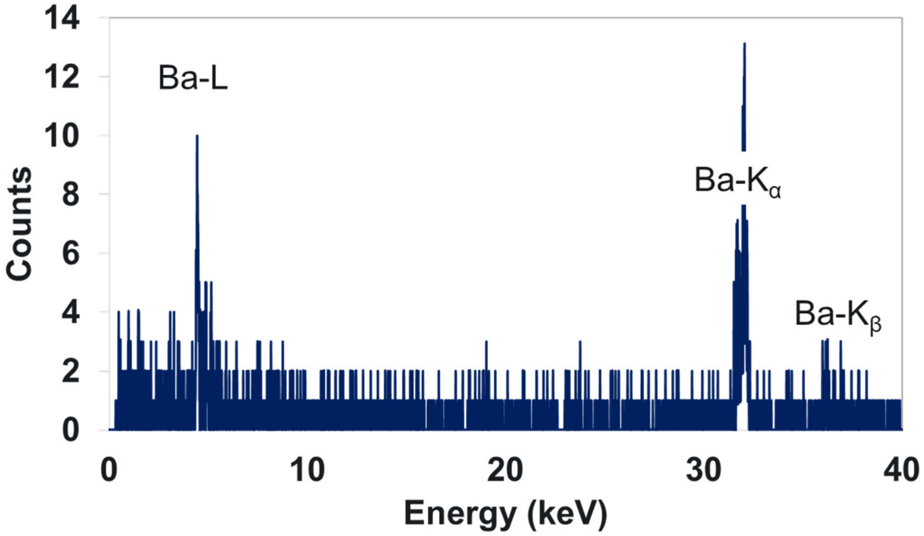

Figure E.2. SDD spectrum from SEM mount (beam off) showing barium X-rays from ^{137}Cs decay (2917 sec count).

The object of automated analysis was to remove potential operator bias from the analysis and to yield statistically useful data. This study shows the potential for this method to improve the quality of SEM analyses; however, the results do depend on consistent sample preparation methods.

The material was further examined with STEM using a JEOL (JEOL Inc., Japan) ARM300F (GrandARM) microscope. Samples were prepared by pipetting the radioactive solution onto a TEM grid. Any large particles were manually removed from the TEM grid. STEM images were collected using an annular dark field detector, and compositional analysis was obtained with EDS and electron energy loss spectroscopy (EELS) using the Gatan Quantum spectrometer (Gatan Inc., Pleasanton, CA). Diffraction patterns were analyzed with DigitalMicrograph™ 3.0 software and utilizing scripts developed by Mitchell.[8]

E.2 Microscopy Solids Analysis

The SEM analysis revealed a large distribution of particle sizes; some particles were close to 0.5 mm in diameter and were identified as sodium phosphates (see Figure E.3A and B). The wide variation in particle sizes meant that many of the particles were too large for STEM analysis, and in some cases even the SEM analysis was problematic owing to the large particle sizes. Manual SEM analysis, automated analysis, and STEM investigations were used in this study. A series of images of the material were collected with BSE imaging and EDS mapping and spot analysis was performed to understand the types of phases present in the material (see Figure E.3 for examples of the morphologies in the specimen).

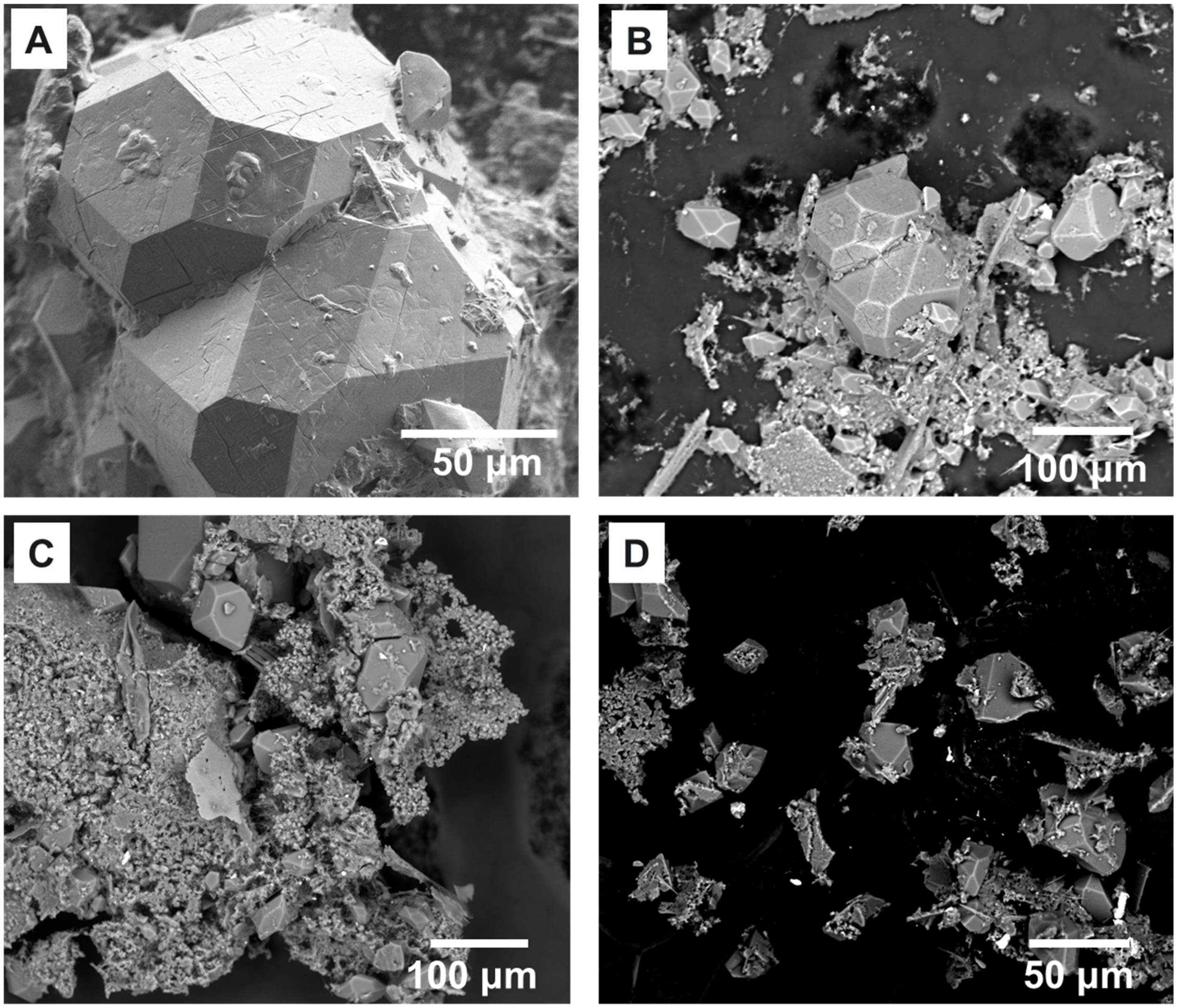

Figure E.3. SEM images of large particles found in the backpulse concentrate.

Sodium phosphate dodecahydrate [$Na_3PO_4 \cdot 12H_2O$ (1/4)NaOH] is known to form a gel during processes, whereas the natrophosphate [$Na_7F(PO_4)_2 \cdot 19H_2O$] phase – which typically crystallizes as large acicular particles, similar to what has been observed in this investigation[9] – can also cause filtering issues.

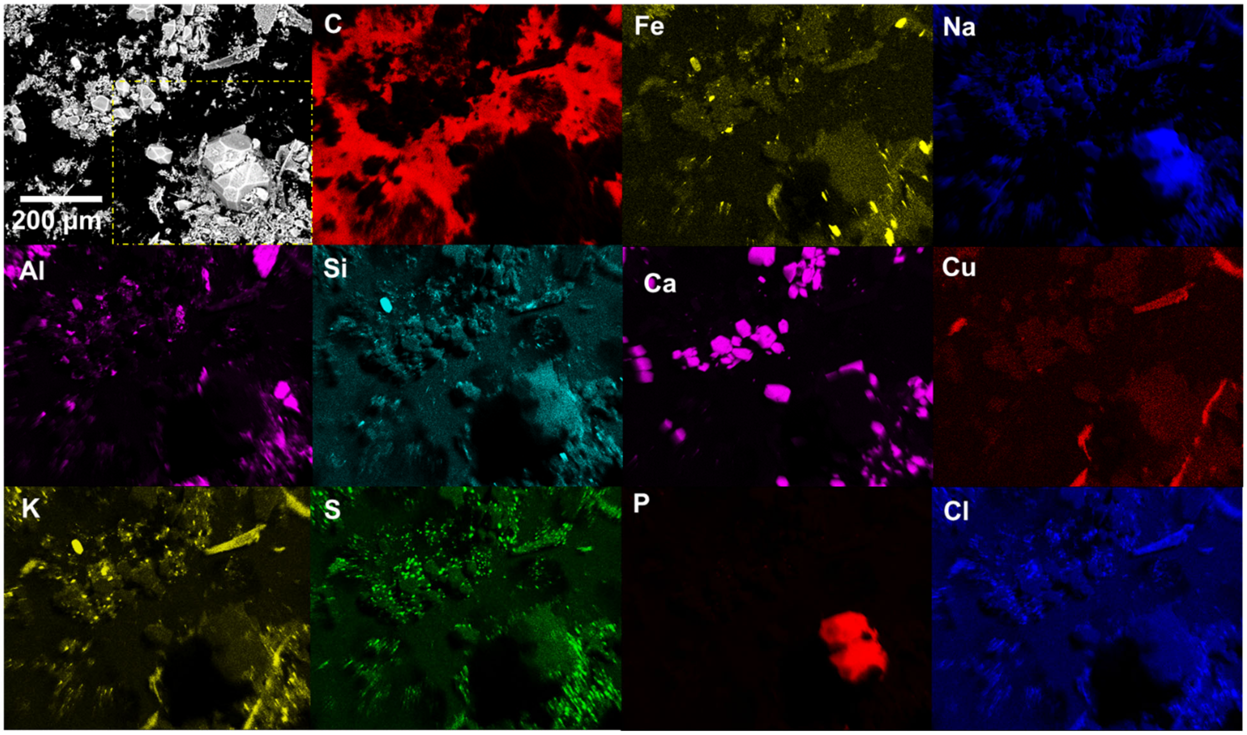

Figure E.4. SEM-EDS elemental maps of the large particles found in the backpulse concentrate showing Ca-rich, phosphate, and Al-particles. The yellow outline in the SE image is the same region as in Figure 4.11B and confirms that this large particle is sodium phosphate.

The SEM image and elemental maps in Figure E.4 reveal several readily identified phases, including a sodium phosphate, calcite-like phase; iron oxides; and aluminum oxides. Figure E.5 provides EDS spectra of the calcite and phosphate phases shown in Figure E.4. The simulation of the EDS was obtained with NIST-DTSA-2 (Microscopium 2021-01-06) software. The match of the sodium phosphate dodecahydrate to the EDS experimental result supports the assignment of this phase. Furthermore, there was no evidence for the presence of fluorine in the phase. The copper "particles" were artifacts from the TEM grid from sample preparation. The copper typically occurred as strips of material. As further preparations were made, this artifact was eliminated. In Figure E.6, a similar distribution of particle types is observed. In this instance, the images A through D show the same region at increasing magnification and the elemental maps show the major composition types. Both Al-oxides and Al-silicates were present, as were several transition metal oxides (Fe, Cr, and Ni) and the calcite phase. In these regions, the phosphate phase was not visible. These types of phases would be unlikely to form as evaporites during the sample preparation and therefore most likely represent the suspended solids material seen blocking the filter during the processing operations. The morphologies of these materials were also striking, and several images were collected showing the variety of morphologies in the specimen. In the SEM instrument, the imaging techniques will impact the visibility of features. The conditions required for elemental analysis are often incompatible with the conditions required to observe very fine or nano-sized features.

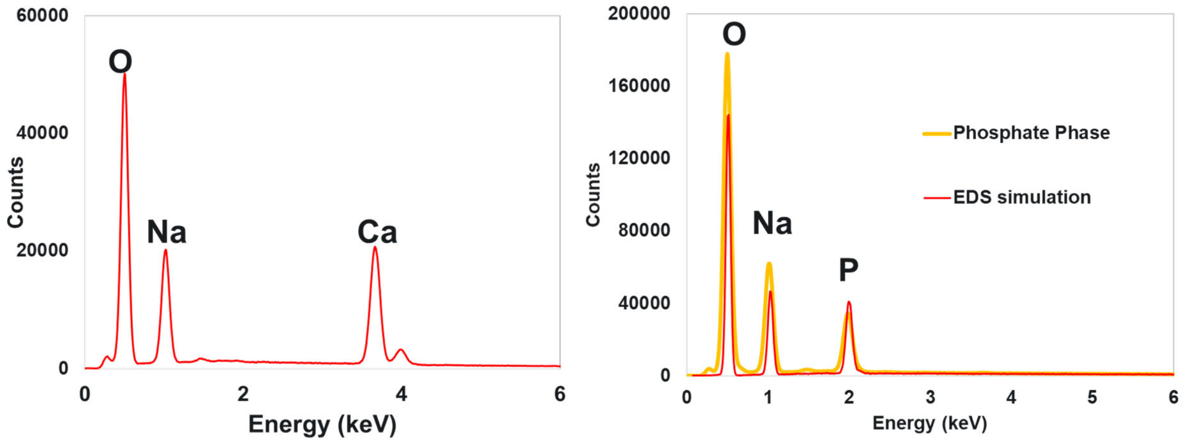

Figure E.5. EDS spectra of calcite phase and phosphate phases. Sodium was ubiquitous in the phases in AP-107. There was no evidence of fluorine in the phosphate phase. Using the composition [$Na_3PO_4 \cdot 12H_2O$ (1/4)NaOH], the EDS simulation is an excellent match for the experimental spectrum. This is good evidence that the phosphate phase in AP-107 is sodium phosphate dodecahydrate despite the morphological mismatch.

Using automated particle analysis, a series of compositional ternary diagrams were developed (see Figure E.7) for some major elements to provide an overview of the compositions in the material (see Table E.1). The compositions for specific classes were user-defined. These can be updated as new information becomes available; however, they roughly split the particles into major types that have been observed previously in Hanford tank wastes.[10, 11] For instance, two major Al-bearing phases were observed, one contained sodium and the other did not. The sodium-containing phase was reported as dawsonite, which has been identified by Reynolds and co-workers,[12] and the other identified as “gibbsite.” Although gibbsite has been observed in Hanford tank waste, this designation was used to identify the composition type. The actual phase remained unidentified but was investigated closely with STEM (see later sections).

The major types of particles are listed together with their quantities and particle sizes in Table E.2. Phosphates were included in the analysis; however, in many instances, these particles were too large to be captured by the segmentation routine. If a particle intersects an edge, it was not counted. Most of the phosphate particles were larger than the field of view at the magnifications required to capture the other phases. The data was collected from four different regions, and a total of 14,000 particles were examined.

This automated particle analysis technique was performed several times with other sample collections. It demonstrates the automated system’s ability to provide more quantitative data on these heterogeneous systems. Several particles remained unidentified. This occurred because the compositional classification was not included in the library. This type of data can be re-analyzed with new compositional classes, if needed. The particles that were included in the unidentified class typically contained Fe, Ti, and Ni (see Figure E.7B). Although the iron content in the particles was high, the classification system did not include them in the “hematite” class because of the presence of these other metals. The phase identifications are classifications for the plots and do not represent direct identification of these phases, but they do provide valuable insight into the composition of the solids in the sample.

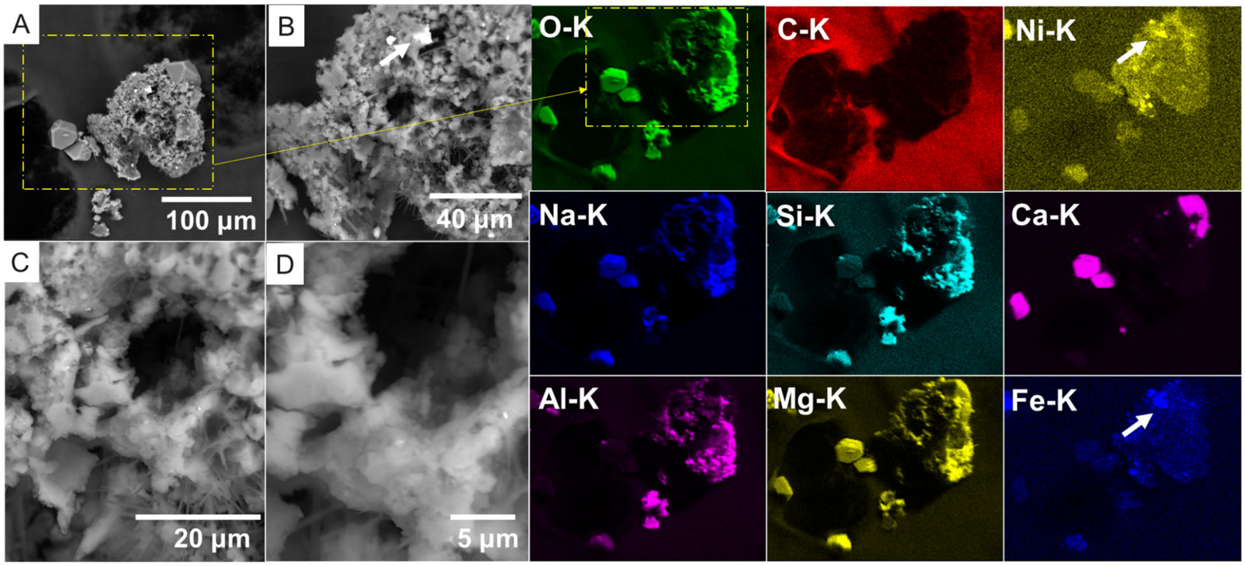

Figure E.6. SEM images (A-D) increasing in magnification of a particle in AP-107 and SEM-EDS elemental maps of this region showing Ca-rich particles, iron oxide, and Al-oxide particles and Al-silicates. The yellow outline in the BSE image shows the elemental mapping area. The white arrow points to the bright feature, which was identified as a metallic (Fe, Ni) particle.

Table E.1. Summary of particles classes and their average compositions (element wt%).

Class	CK	OK	NaK	MgK	AlK	SiK	PK	SK	ClK	KK	CaK	TiK	FeK	NiK
Nitrate/Nitrite	6.8	47.0	38.7	0.1	4.0	0.1	0.1	0.5	0.3	0.3	0.3	0.1	0.4	0.3
Gibbsite/Al-Oxide	1.2	55.8	10.8	0.1	29.3	0.1	0.0	0.1	0.3	0.4	0.4	0.1	0.4	0.3
Oxalate (C and O)	36.9	44.7	2.7	1.5	1.7	1.4	1.0	1.0	1.0	0.8	1.0	0.7	0.8	0.9
Na-Aluminate/Dawsonite	11.4	50.9	19.2	0.2	13.4	0.6	0.2	0.2	0.4	0.4	0.5	0.2	0.4	0.4
Calcite	7.5	52.4	17.9	0.4	1.5	0.5	0.3	0.4	0.4	0.5	14.8	0.3	0.6	0.5
Na-Phosphate	6.7	44.7	33.6	0.3	1.8	0.4	7.7	0.4	0.5	0.5	0.4	0.3	0.4	0.5
Metal oxides/Hematite	20.1	41.7	13.1	1.0	5.3	1.3	0.9	0.9	1.1	1.2	1.4	0.9	3.1	1.9
Na/Gaylussite	22.2	47.0	24.5	0.4	1.8	0.3	0.3	0.3	0.4	0.3	0.3	0.2	0.2	0.3
Unknown	10.7	11.9	6.2	0.9	3.2	1.7	1.8	2.4	2.9	3.3	5.0	3.6	6.3	5.8

The nitrate/nitrite class is an evaporite phase, as are possibly the “oxalate phases” that contained mainly carbon and oxygen. When sodium was also present, the phase was designated as gaylussite, a Na-carbonate phase. The phase containing calcium plus oxygen and carbon was termed calcite and particles containing iron were designated as hematite. Sodium was ubiquitous in the specimen, as was expected, and was included in all analyses where particle types were assigned. Previous studies have identified most of these phases with X-ray diffraction (XRD), which is why compositions matching these phases have been assigned these designations.

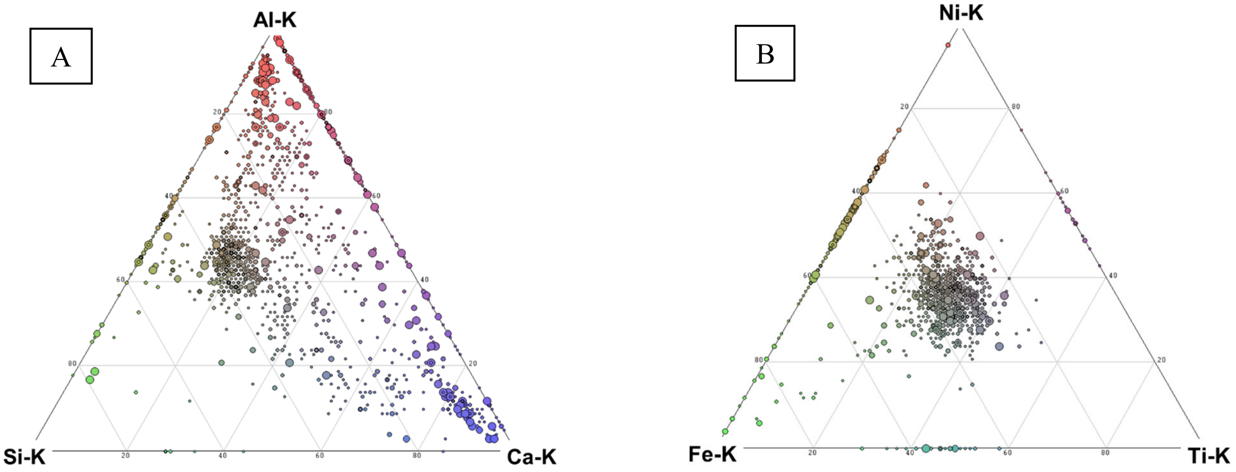

Figure E.7. Ternary plots of selected elements in AP-107 for major phases (A) and the unknown particle designation (B).

Table E.2. Summary of particles found in AP-107 in four regions.

	Region 1		Region 2		Region 3		Region 4	
Class	Number of Particles	Diameter (µm)	Number of Particles	Diameter (µm)	Number of Particles	Diameter (µm)	Number of Particles	Diameter (µm)
1 Nitrite/Nitrate	175	7.98	671	8.74	420	6.86	213	10.33
2 Gibbsite	85	12.67	87	14.54	158	10.98	3	16.95
3 Oxalate (C and O)	750	3.88	2776	2.98	637	2.57	848	2.79
4 Na-Aluminate/Dawsonite	496	8.81	1570	6.54	618	6.97	278	7.8
5 Calcite	162	13.89	191	12.67	184	12.95	61	7.68
6 Na-Phosphate	32	14.13	100	4.34	51	6.98	13	7.5
7 Metal oxides/Hematite	294	4.82	968	4.07	337	4.62	127	5.21
8 Na/Gayussite	218	2.45	1625	2.94	291	2.11	302	3.84
Total Number of Particles (14,471 for all regions)	2212	--	7988	--	2696	--	1845	--

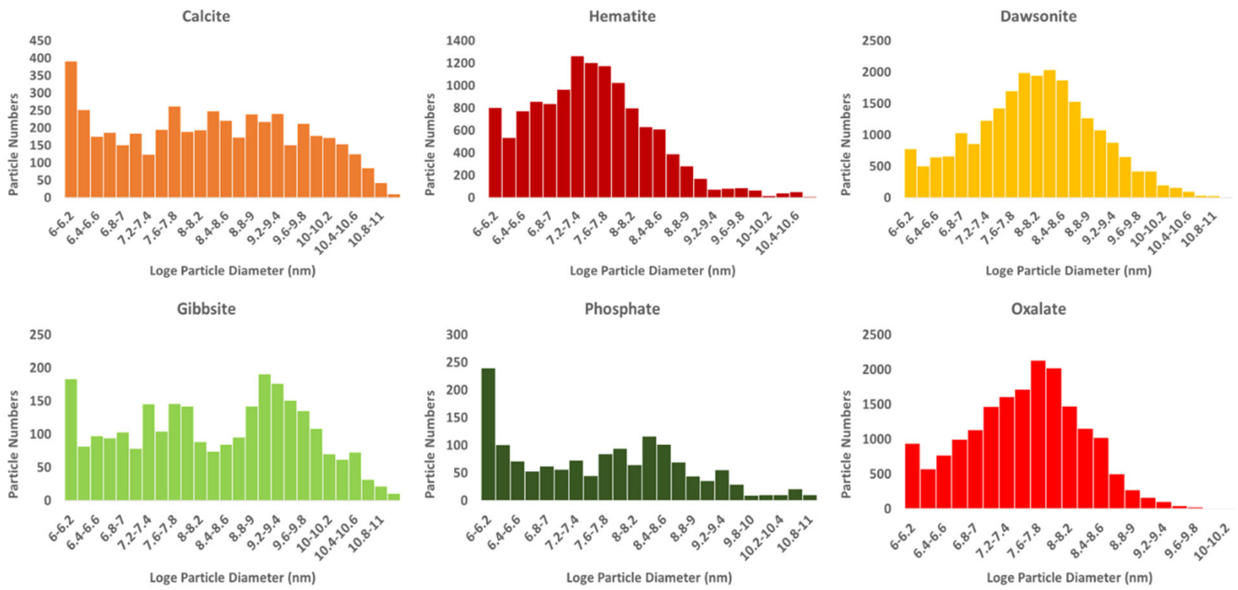

Figure E.8. Major types of particles and their size distributions observed in the AP-107 specimen. Automated particle analysis was used to analyze more than 16,000 particles and categorize them according to the reported EDS composition and the $\log_e$ of the particle diameter reported in nanometers.

The particle size (particle diameter in nanometers) distributions were fitted to a log-normal curve for each of the major identified classes (see Figure E.8). Particle size distributions most often will possess a gaussian fit when plotted as a log-normal distribution. The phosphate distribution did not fit this, but this could possibly be because the phosphate particles were larger than the field of view for the imaging conditions.

The occurrence of the Al-oxide phase was examined in more detail because it might be one of the phases responsible for blocking the filter, given the morphology of this phase and its inherent insolubility. Figure E.9 shows SEM-EDS analysis of an aluminum oxide phase. The morphology was investigated by using the SE detector and imaging at a lower kV (see Figure E.9B). The particles appeared to be composed of stacked discs. This morphology was inconsistent with common aluminum oxide phases found in the Hanford tanks, including boehmite and gibbsite. Boehmite in Hanford tank waste also is usually much smaller than the material shown in Figure E.9.[13]

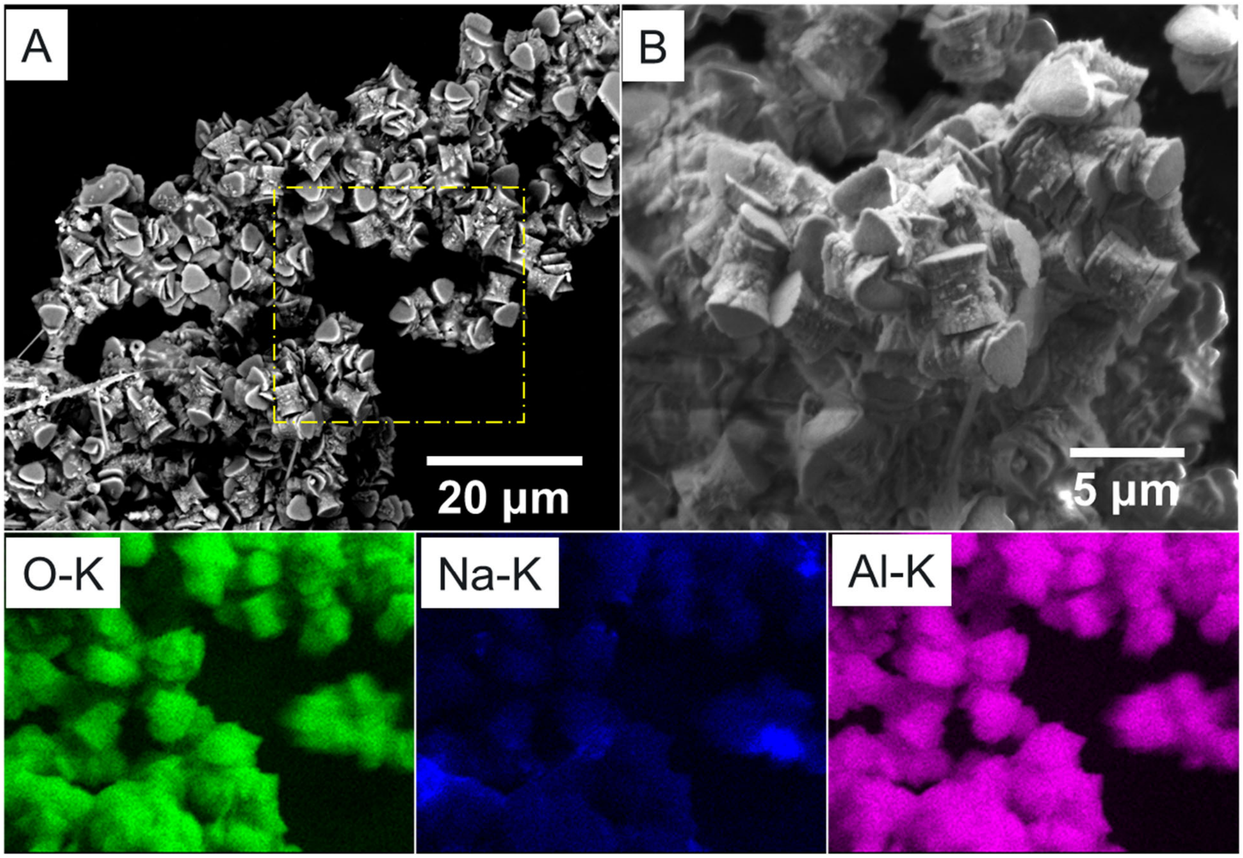

Figure E.9. An aggregate of an aluminum oxide material that was common in AP-107 suspended solids. The elemental maps show the absence of most other elements in this phase.

E.3 STEM-HAADF Analysis

STEM analysis was used to understand the nature of the non-sodium-bearing salt precipitates in the specimen; however, sodium-bearing salts were common in the prepared samples. Figure E.10 shows examples of STEM images and analysis of nitrate/nitrite particles. The EDS instrument on the STEM has a better resolution than the current system on the SEM instrument, and nitrogen is clearly visible in the particles. The STEM images and elemental maps in Figure E.13 show the sodium phases again, but other phases – notably, aluminum-rich phases – are present. Evaporite sodium phases could be observed surrounding the holes in the carbon support film. This is a good indication that these phases formed during the sample preparation process. Other STEM-EDS analyses (see Figure E.12) highlighted an alumino-silicate particle as well as some iron oxides. In contrast to the sodium-bearing phases, these particles were clearly crystalline and likely were present in the suspended solids in the original AP-107 sample.

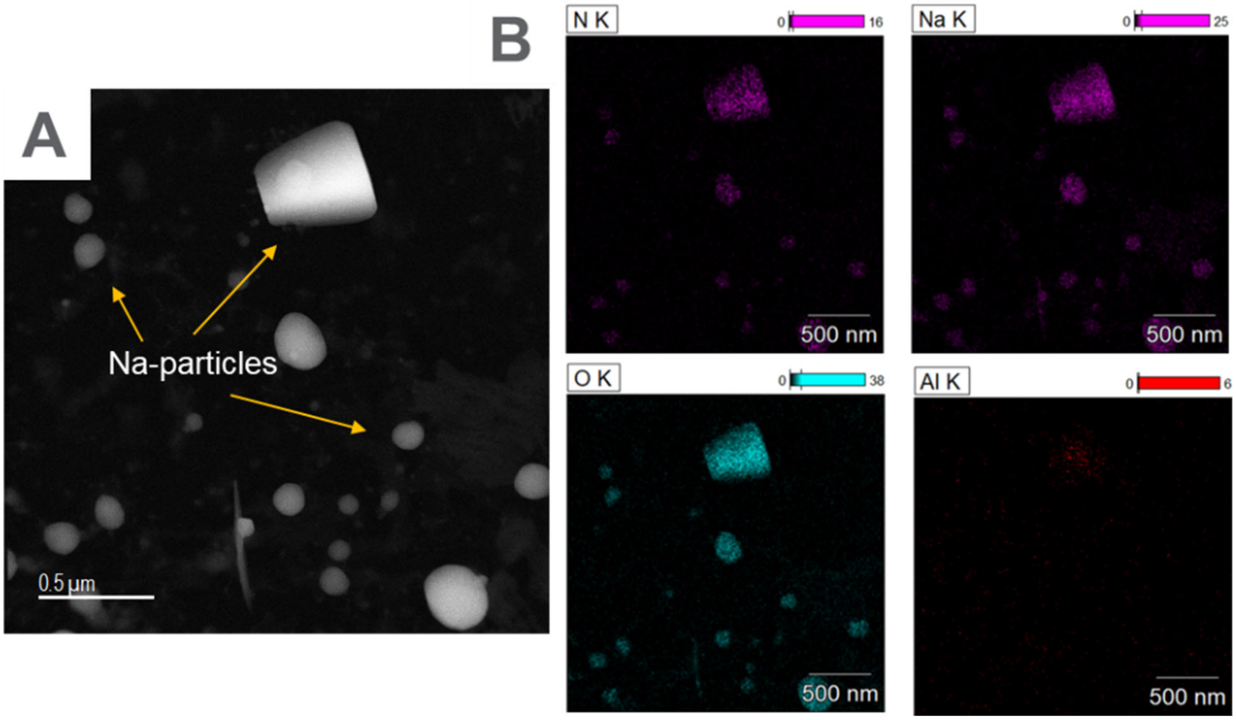

Figure E.10. Nitrate particles were common in the STEM prepared sample. These are likely evaporite phases that were not part of the suspended solids.

In Figure E.11, the phase appears to be entirely aluminum oxide, but there is an indication of other elements being present.

Excluding the dominant sodium nitrate material from the solids-washing process, there appear to be Al-silicates, mixed Cr-Al oxide, and Fe-oxides phases. Within these phases, localized enrichment of Mg and Ca was only partly visible. These compositions could be consistent with phases previously identified in tank wastes, such as cancrinite and Fe-oxides. STEM-EDS and electron diffraction was used to investigate whether these phases could be present in the sample.

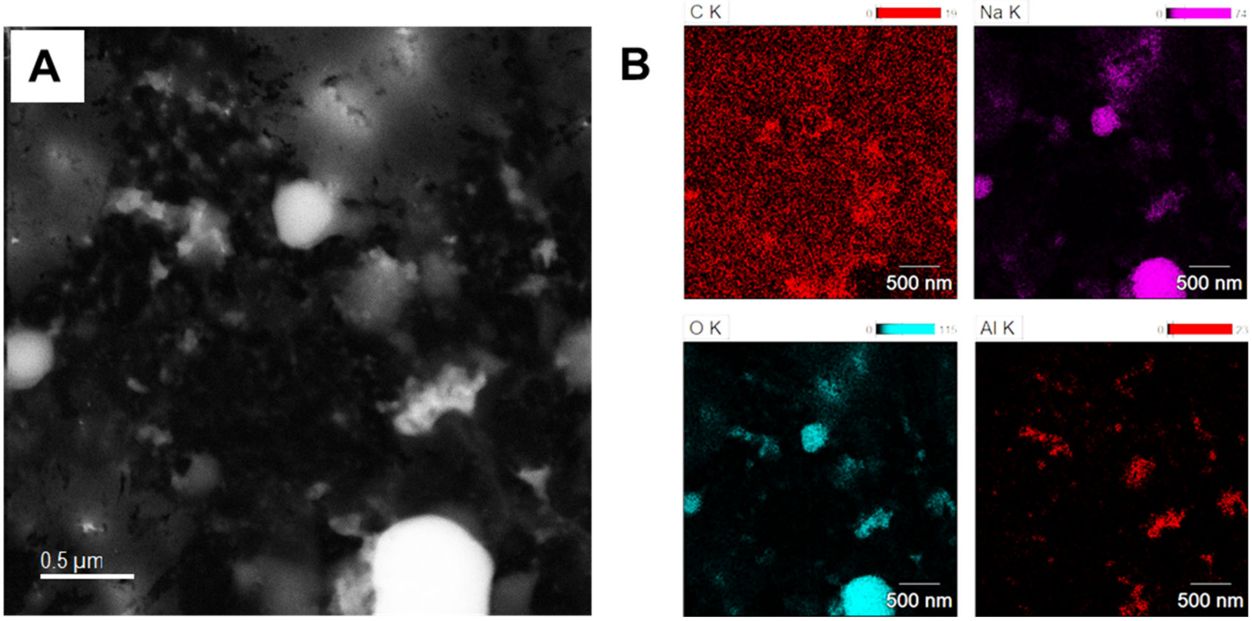

Figure E.11. Low-magnification STEM image and EDS analysis of a particle agglomerate showing an aluminum phase within the salt phases.

The SEM analysis and SEM-EDS analysis pointed to several additional minor phases that were present in the sample. With STEM and its analytical capabilities, it was possible to conduct a more detailed investigation of the occurrence of these minor phases and to see if they can be described in greater detail. Ti, Fe, and Ni were detected in the SEM-EDS analysis and reported as the “unknown” phase group, but it was not clear if these were artifacts or background because the signals were not strong. STEM could be used to establish if the major phases observed have any minor precipitates associated or attached to them. Because of the large size of the phosphate particles, it was unlikely that phosphate particles would be located during the STEM analysis. Indeed, phosphate particles were removed manually using an applicator stick from the TEM sample preparations as these would have been excessively large to image (the electron beam would not have penetrated them) and added to the total dose of the sample, creating an unnecessary hazard to the tools.

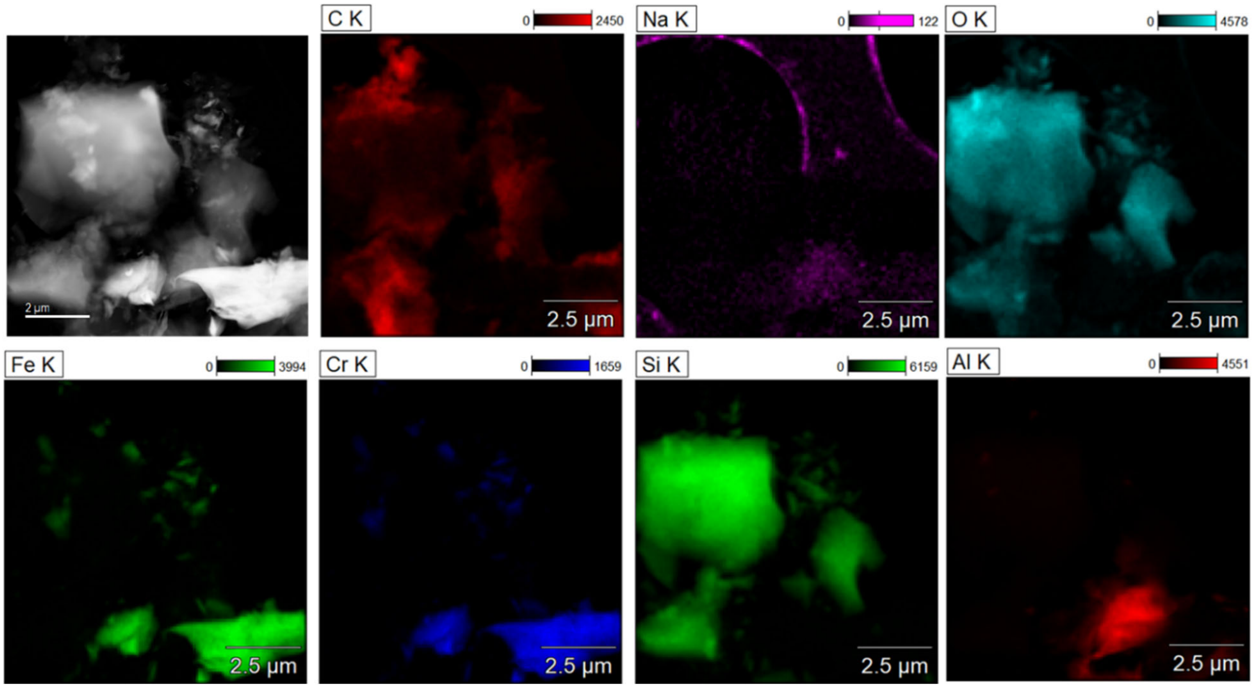

Figure E.12. High-angle annular dark-field imaging (HAADF) image and STEM-EDS analysis of particle agglomerate showing a Si-phase, Al-phase, as well as Fe-Cr phases. Salt phases (Na) are lacing a pre-formed hole in the carbon support grid.

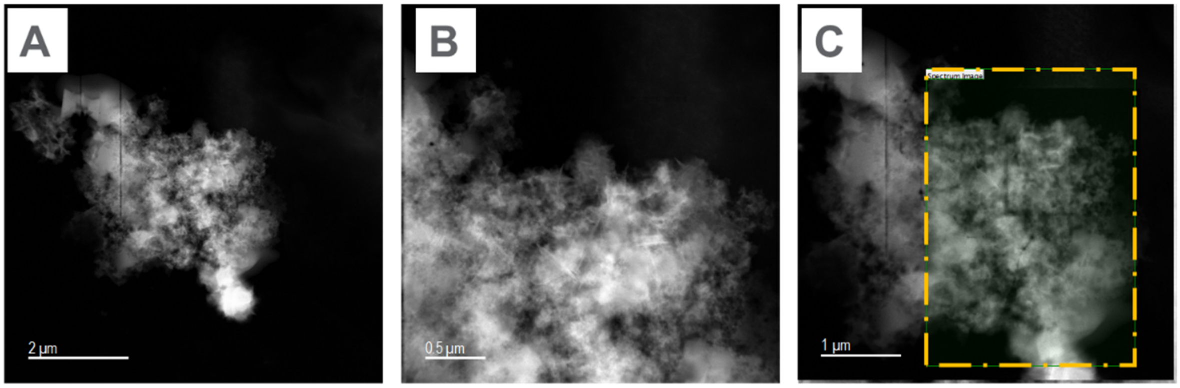

STEM ADF Images of Al-bearing agglomerate in AP-107 (region 3)

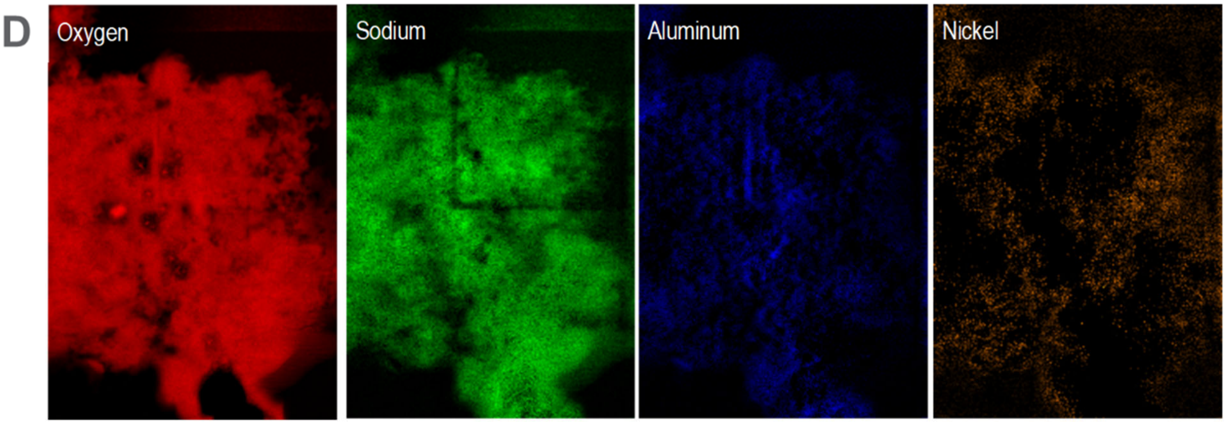

Figure E.13. (A-C) STEM images of particle agglomerate and (D) EELS maps of the material from region marked in (C) showing the occurrence of the Al-oxide that also appeared to contain Na. The straight black lines were beam damage from the STEM probe. This region was further interrogated (see Figure E.12)

Further analysis of the Al-phases shown in Figure E.13 with STEM EELS (see Figure E.14) indicated that it was Al oxide with nano-particles of iron and nickel. Electron diffraction of this region (see Figure E.14B) produced a ring pattern that was obtained in TEM-diffraction mode. The high-resolution TEM image (see Figure E.14C) shows some lattice fringes.

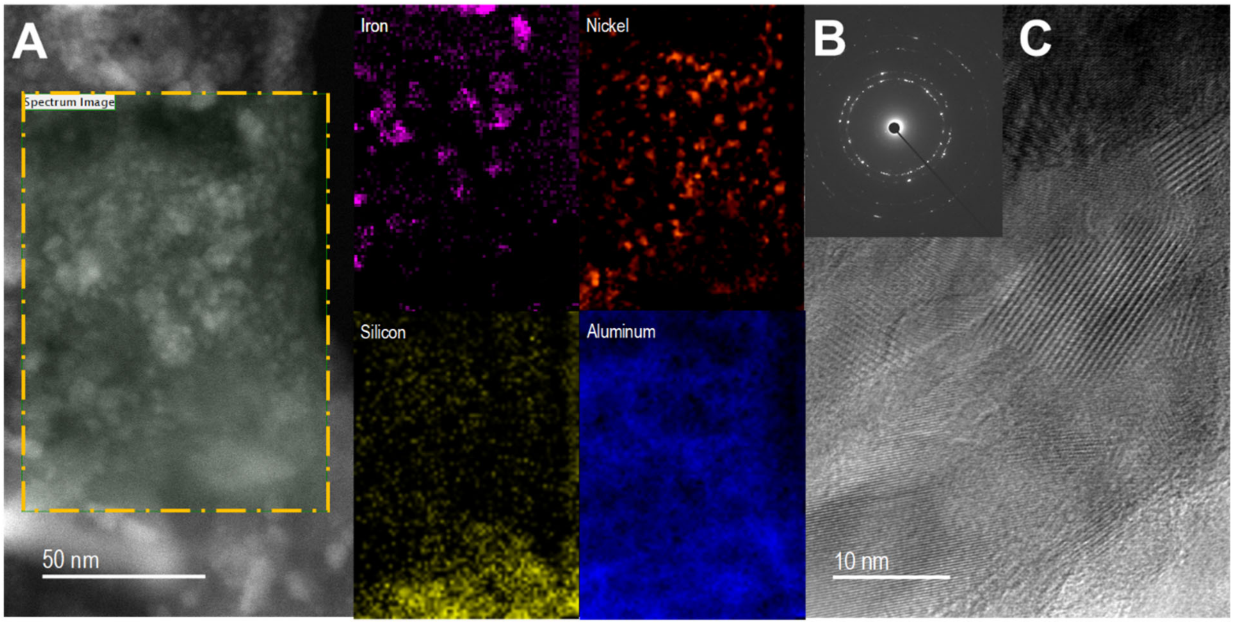

Figure E.14. STEM-EELS analysis of an aluminum oxide particle agglomerate showing the occurrence of nano-precipitates of iron and nickel. This shows the complexity of the composition of phases in the wastes. The electron diffraction (B) and high-resolution TEM image of the same region (C) where used to determine the phase (see Table E.3).

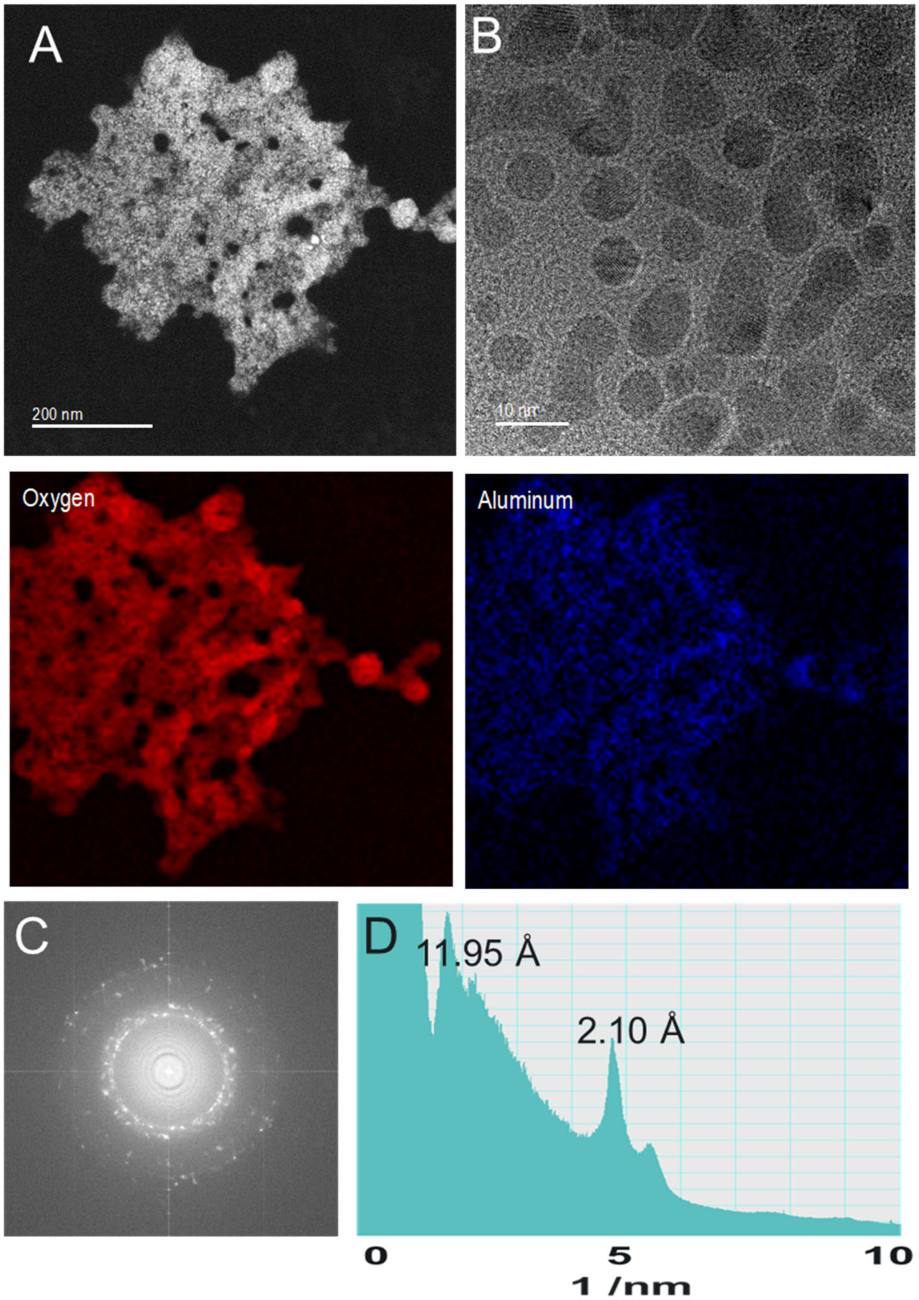

Figure E.15. (A) STEM images of the aluminum oxide particle agglomerate; (B) high-resolution TEM image showing the nanocrystalline nature of the material, EELS maps of oxygen and aluminum; (C) fast Fourier transform (FFT) of the high-resolution TEM image, and (D) a rotational average of the FFT with major peaks marked.

In Figure E.15, Al again was present in the phase, and at high magnifications under TEM imaging, the phases appeared to be nanocrystalline. An electron diffraction of the phase was obtained by examining the Fourier transform of the lattice image (see Table E.3); however, only a few reflections were found and much of the material was amorphous or possibly damaged rapidly under the electron beam. It would not be possible to use XRD to examine these solids as there was an insufficient amount of material. The electron diffraction (see Table E.3) was not convincing for the occurrence of specific well-known aluminum phases. However, there were good matches with sodium aluminate, which agrees with much of the EDS analyses. The match to gibbsite or boehmite was poor. The literature values in Table E.3 were taken from prior XRD reports on Hanford tank characterizations.[14, 15]

Table E.3. Electron diffraction analysis of the Al-oxide particles.

Al-particle, (d/nm)	Literature Values (d/nm)	Reported Tank Waste Phases containing Al	
	1.1950		
0.9304			
		0.60617,	Boehmite
0.5841	0.58942	Boehmite	
	0.48379	Gibbsite	
0.2662	0.27860	Na aluminate	
0.2595, 0.2532	0.25260	Na aluminate	
0.2203	0.23328	Na aluminate	
	0.2104	0.21197	Na aluminate
	0.20324, 0.2034	Gibbsite	
	0.20041	NaAlOx	
		0.18521	Boehmite
0.1648	0.17831, 0.1693	NaAlOx,	
0.1543	0.157	Cancrinite	
	0.1447, 0.1486	Cancrinite	
0.1372	0.1364	Cancrinite	

Additional electron diffraction results were obtained from phases from the STEM analysis, but these were not included in this report as they were likely salt phases.

Figure E.16 shows an alumino-silicon-bearing phase, but the STEM images (A and B) show nano-particles sorbed to the phase. The elemental map did not reveal the nature of the small particles. Further inspection of this region showed the Al, Na, and O signals and that the nano-particles were Ni-rich.

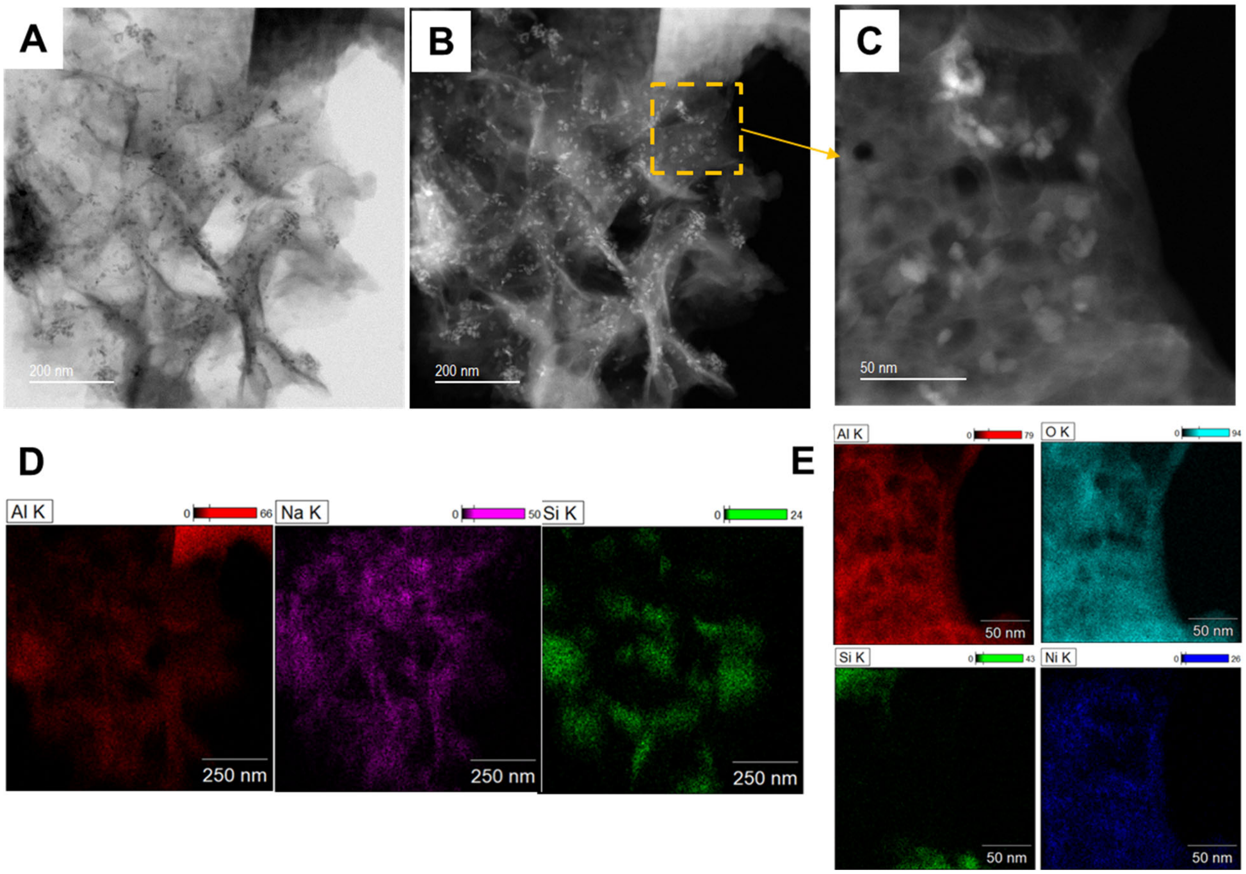

Figure E.16. STEM (A) bright field and (B) dark field images of a sodium alumina-silicate phase with evidence of nano-precipitates. Higher-magnification image (C) shows these precipitates in more detail. Elemental maps (D) of the areas in (A and B) and elemental map (E) for region shown in (C) indicate that the precipitate is nickel-rich.

E.4 In Situ Observations and Dissolution Investigations

Particles were observed directly in the solution in the SEM instrument to confirm the presence of micro-sized solids beyond doubt. In Figure E.17, SEM images of the suspended backpulse solids in the as-received solution are shown. Several micron-sized particles can be seen. In Figure E.17A, the large particle with the angular shape and size is consistent with the sodium phosphate particles that were observed in the ex situ analyses. SEM-EDS elemental maps of the one region were obtained and are shown in Figure E.18. Although the count rate was low, distinctive Al-rich particles can be seen, consistent with the earlier results with dried samples. The bright spot with the Ca-map may also indicate a particle, although this is not convincing. The beam current, and map resolution, and time were deliberately kept low to avoid rupturing the window. The oxygen signal is from water in the cell, whereas the maps from other elements are too noisy.

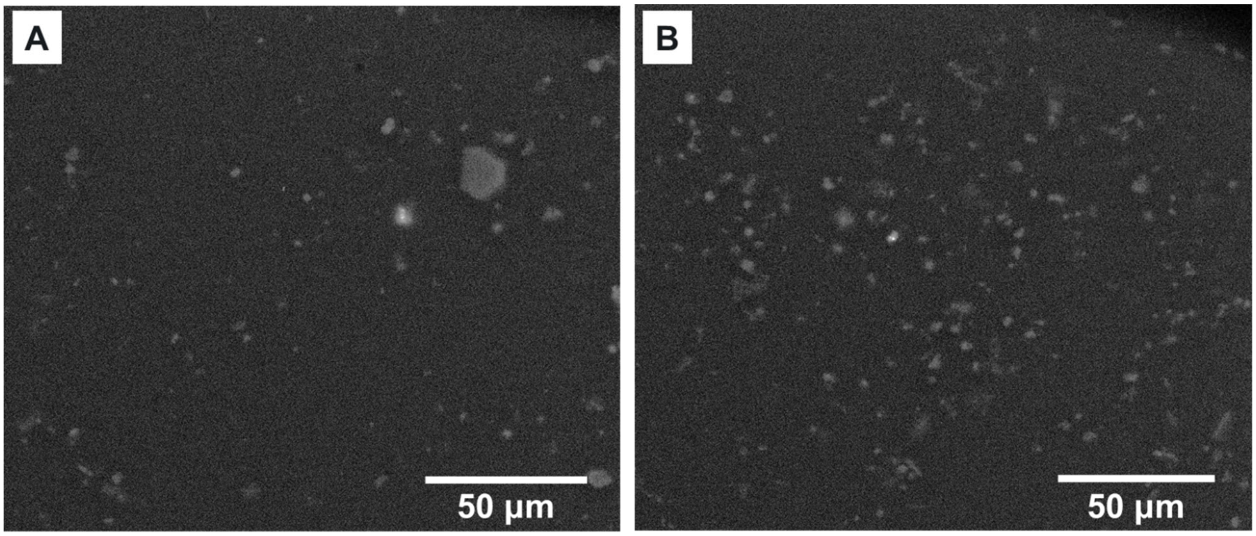

Figure E.17. In situ SEM images of AP-107 suspended particles in solution obtained using a wetSEM cell.

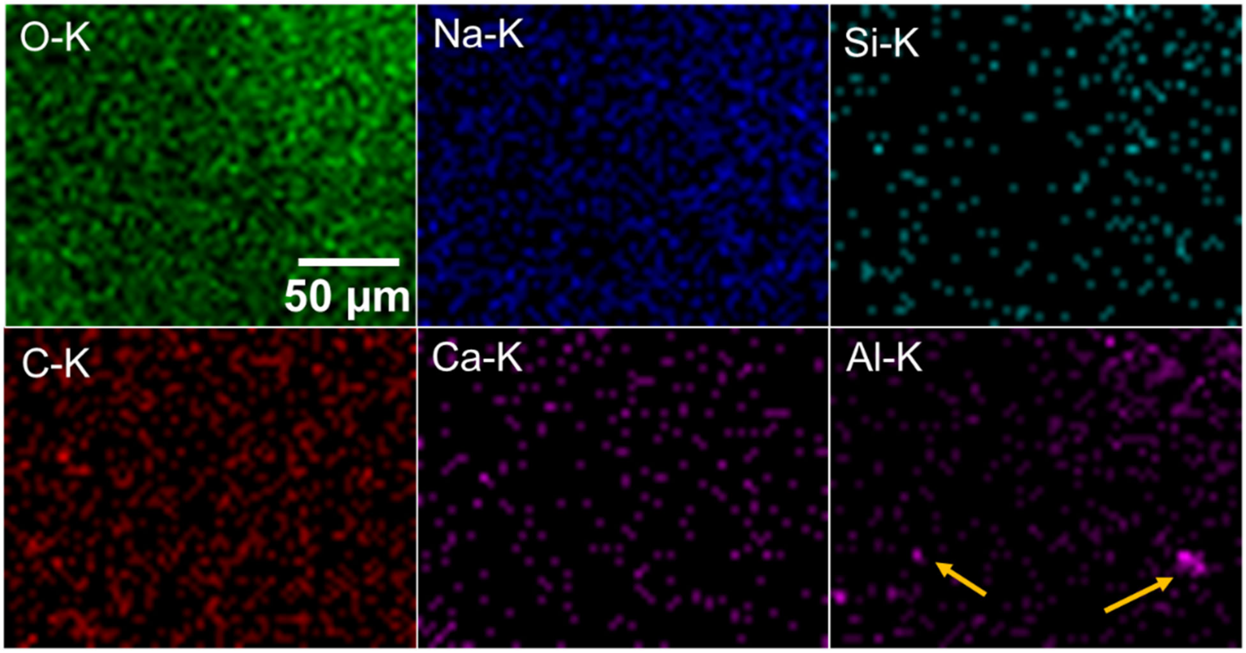

Figure E.18. Elemental maps obtained from liquid cell showing the occurrence of Al-phases in solution.

There have always been questions about the effect of drying Hanford tank waste particles prior to imaging them in the electron microscope. Using in situ liquid cells, it is possible to examine the particles in the solution or in a hydrated state.

The backpulse solids have been dissolved using a weak alkaline NaOH solution. To understand the effect of this method on the specimen, a few experiments were performed exposing the prepared SEM sample to this solution. A cap containing a few drops of 0.1M NaOH was placed over the top of the SEM instrument mount, creating a chamber where the sample was exposed to vapor. The intention was not to dissolve the particle directly but merely to look at partial dissolution. Figure E.19 shows the result of this technique on a sodium phosphate particle. The image shows the same phase before and after this process.

The phosphate has undergone extensive pitting and dissolution. A few smaller particles have either completely dissolved or have been transported away. Some particles appeared to be unaffected by this process.

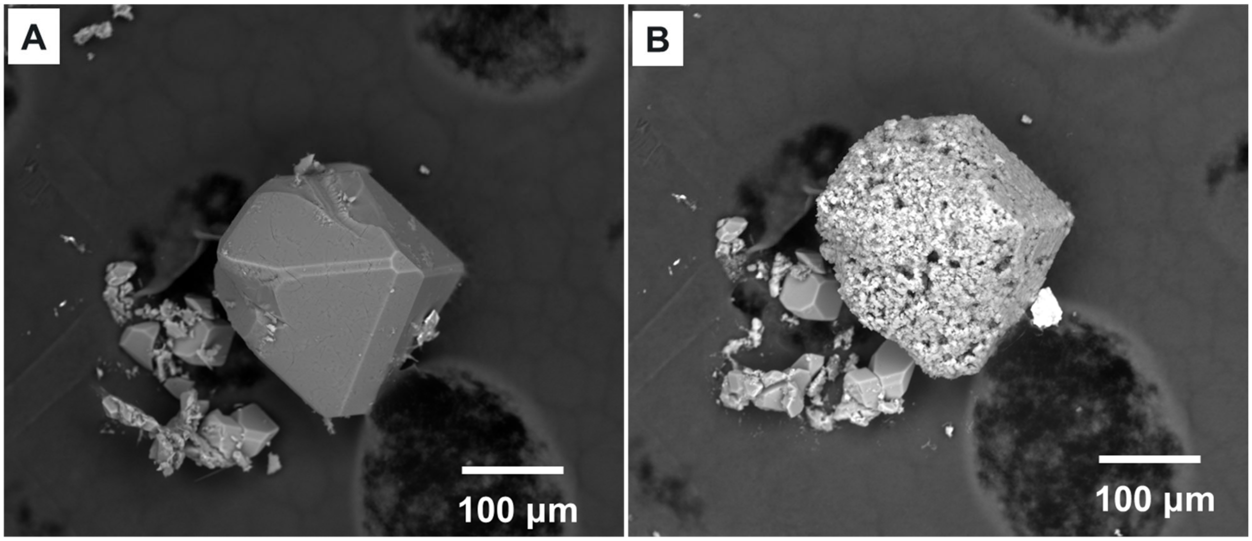

Figure E.19. Phosphate particle from as-received AP-107 sample and following exposure with 0.1 M NaOH "vapor." The large phosphate particle has undergone corrosion and pitting but the smaller calcite particles have not been affected.

In Figure E.20, both phosphate and an aluminum oxide phase that is shown in Figure E.9 were also exposed to these weak dissolution conditions. The morphology of these particles was distinctive, with a "stacked-plates" appearance. These particles were also likely the same Al-phase that was observed in the STEM investigation. Following the dissolution treatment, the particles had appeared to form an amalgam, but the phosphate component appeared to be completely dissolved. A few fibrous particles were visible.

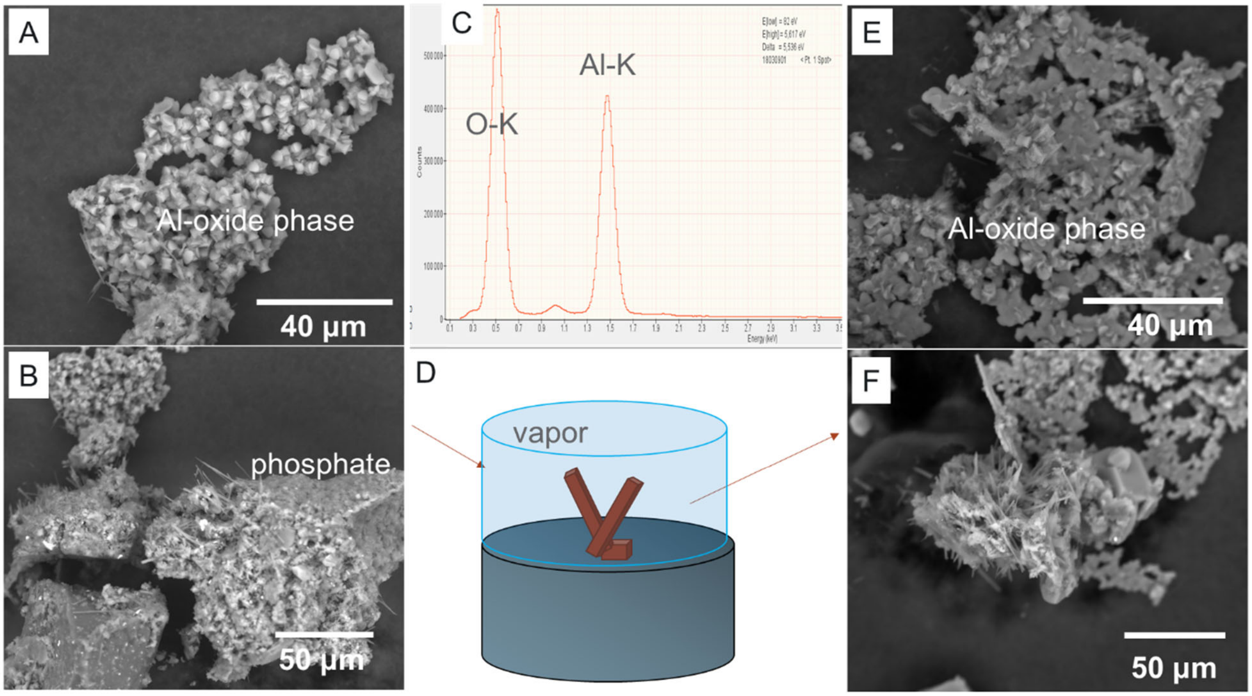

Figure E.20. SEM particles of phosphate and Al-oxide (A and B) were imaged. The major phase present was shown to be an aluminum oxide (C). The specimen was then exposed to a dilute vapor environment of NaOH (D). The vapor was created by dropping a solution into a vial and placing this on top of the SEM instrument mount for several hours. SEM images following this chemical attack revealed dissolution of the phosphate phase and partial dissolution of the Al-oxide phase.

The large phosphate particles in the specimen were sufficiently large that they would have been visible with the naked eye and hence may represent the most obvious particles on the backpulse filter, but the aggregates of Al-oxides that formed large structures might have also been visible. The same type of particle distribution analysis was obtained from three different conditions: as prepared, exposed for 2 hours, and exposed for 4 hours. In this case, the automated particle analysis was run over the same region. However, with slight shifts in the position of the mount, particles could move to an edge of the field of view and would not be counted by the software. This methodology could be improved by running the analysis at a series of magnifications or using techniques that better capture the particle morphologies. Figure E.21 shows the results of the change in particle size dissolution during this process. The experiment was used to determine which composition type was most impacted by the process, not to demonstrate complete dissolution.

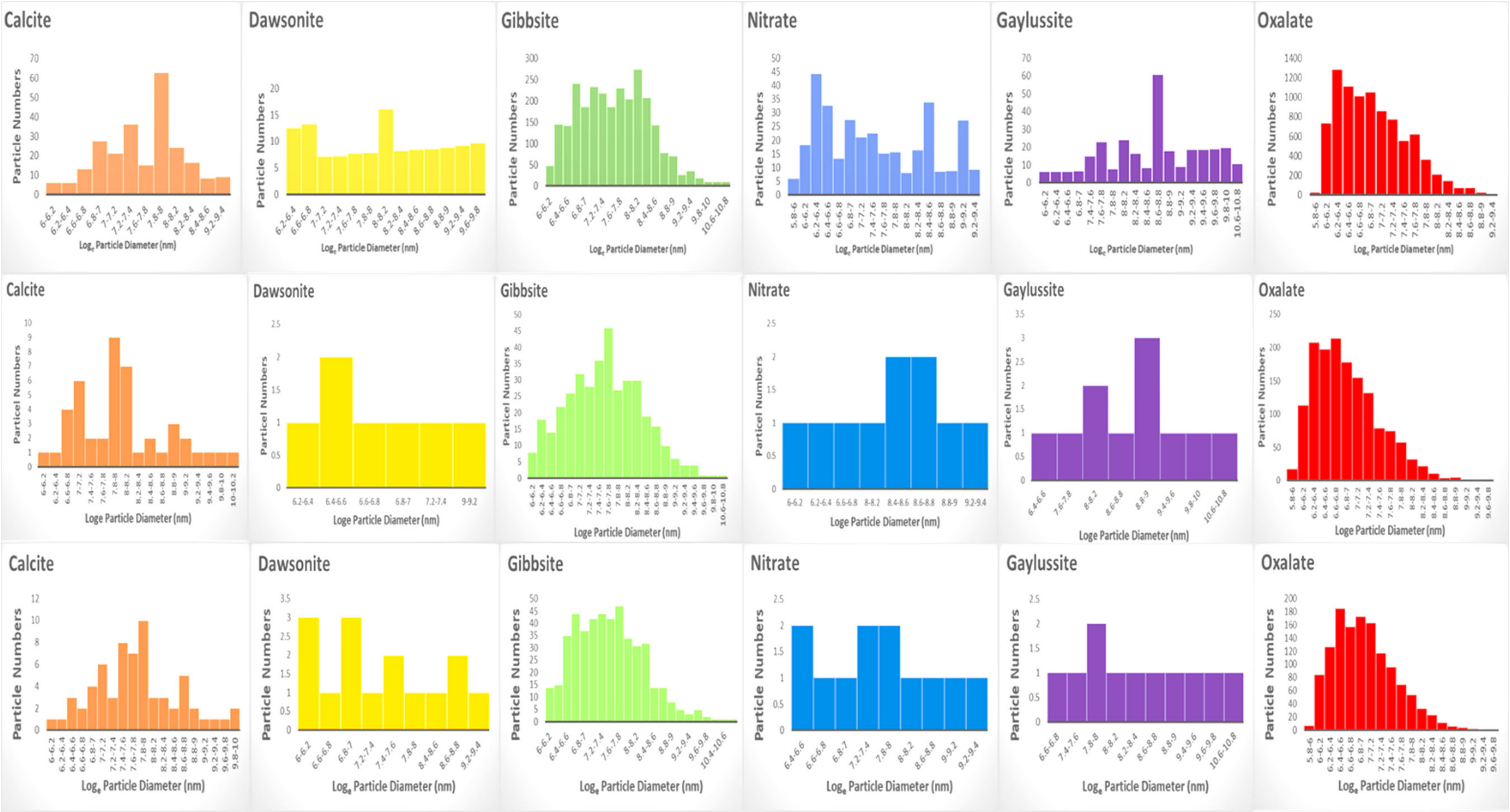

Figure E.21. Particle size distribution of six different particle types observed in AP-107 reported in log$_e$ of the reported particle diameter in nanometers: calcite (orange), dawsonite (yellow), gibbsite (green), nitrate (blue), gaylussite (purple), and oxalate/Na-oxalate (red). The top row represents data collected from the as-received sample. The middle and bottom rows represent analyses from exposure to 0.1 M NaOH for 2 and 4 hours, respectively. Particles smaller than below 0.5 µm were not analyzed and large particles were not always analyzed if they intersected the edge of the image. The identification of specific phases was based on the SEM-EDS analysis of the particles. The NaOH had little impact on the calcite and gibbsite-like phases but had a significant impact on the dawsonite phase, gaylussite, and the nitrate particle content. The oxalate phase was also impacted, with the larger particles appearing to have dissolved. The phosphate phases were left out of this analysis as they were, in general, excessively large and there were relatively few of them in the specimen.

It is expected that dissolution would impact the evaporite phases the most, and this can be seen in the particle distribution analysis. The particles designated as "nitrate" and "gaylussite," i.e., the sodium carbonate phase, were reduced in total number and in distribution. The oxalate contribution was also correspondingly affected where the total number of particles detected went from the thousands to a few hundred. However, the overall particle size distribution remained similar. Even with the "gibbsite" representing the Al-oxide component, and "calcite" particle distributions, the total number of identified particles decreased. In the case of "calcite," the particle number decreased as did the number of larger particles.

This experiment demonstrates some of the potential for SEM combined with automated particle analysis to provide more quantitative data on processing operations. The dissolution experiment here was a demonstration of the capabilities of this new tool to describe the dissolution behavior.

E.5 Conclusions of Microscopy Study

The SEM-based automated particle analysis provided information on the particle size distributions found in the backpulse sample for the various compositional types. The iron oxide, calcite, and Al-oxide phases had similar particle size distributions. By conducting a partial dissolution experiment on the backpulse sub-sample, it was possible see the phases that were being attacked by the chemical treatment and the effect on their particle size distributions. There was clear corrosion of the phosphate phase. Particle numbers of the nitrate-like phases and sodium-alumino-carbonate phases showed that they underwent significant dissolution and removal, whereas the particle size distributions of the calcite and Al-oxide phases were relatively unaffected.

E.6 References

1. Buck, E. C.; Wittman, R. S.; Soderquist, C. Z.; McNamara, B. K., Monitoring bromide effect on radiolytic yields using in situ observations of uranyl oxide precipitation in the electron microscope. *RSC Advances* **2018,** *8*, (33), 18227-18233.

2. Cantrell, K. J.; Um, W.; Williams, B. D.; Bowden, M. E.; Gartman, B.; Lukens, W. W.; Buck, E. C.; Mausolf, E. J., Chemical stabilization of Hanford tank residual waste. *Journal of Nuclear Materials* **2014,** *446*, (1–3), 246-256.

3. Buck, E. C.; McNamara, B. K., Precipitation of nitrate-cancrinite in Hanford tank sludge. *Environmental science & technology* **2004,** *38*, (16), 4432-4438.

4. Krupka, K. M.; Schaef, H. T.; Arey, B. W.; Heald, S. M.; Deutsch, W. J.; Lindberg, M. J.; Cantrell, K. J., Residual Waste from Hanford Tanks 241-C-203 and 241-C-204. 1. Solids Characterization. *Environmental Science & Technology* **2006,** *40*, (12), 3749-3754.

5. Lumetta, G. J.; McNamara, B. K.; Buck, E. C.; Fiskum, S. K.; Snow, L. A., Characterization of High Phosphate Radioactive Tank Waste and Simulant Development. *Environmental Science & Technology* **2009,** *43*, (20), 7843-7848.

6. Laskin, A.; Cowin, J. P., Automated Single-Particle SEM/EDX Analysis of Submicrometer Particles down to 0.1 µm. *Analytical Chemistry* **2001,** *73*, (5), 1023-1029.

7. Brożek-Mucha, Z., Scanning electron microscopy and X-ray microanalysis for chemical and morphological characterisation of the inorganic component of gunshot residue: selected problems. *Biomed Res Int* **2014,** *2014*, 428038-428038.

8. Mitchell, D. R. G., DiffTools: Electron diffraction software tools for DigitalMicrograph™. *Microscopy Research and Technique* **2008,** *71*, (8), 588-593.

9. Herting, D. L.; Reynolds, J. G. J. E. C. L., The composition of natrophosphate (sodium fluoride phosphate hydrate). **2016,** *14*, (3), 401-405.

10. Peterson, R. A.; Buck, E. C.; Chun, J.; Daniel, R. C.; Herting, D. L.; Ilton, E. S.; Lumetta, G. J.; Clark, S. B., Review of the Scientific Understanding of Radioactive Waste at the U.S. DOE Hanford Site. *Environmental Science & Technology* **2018,** *52*, (2), 381-396.

11. Wells, B.; Knight, M.; Buck, E.; Daniel, R.; Cooley, S.; Mahoney, L.; Meyer, P.; Poloski, A.; Tingey, J.; Callaway, W., Estimate of Hanford Waste Insoluble Solid Particle Size and Density Distribution. *Battelle—Pacific Northwest Division, Paper No. PNWD-3824* **2007**.

12. Reynolds, J. G.; Cooke, G. A.; Herting, D. L.; Warrant, R. W., Evidence for dawsonite in Hanford high-level nuclear waste tanks. *Journal of Hazardous Materials* **2012,** *209–210*, 186-192.

13. Snow, L. A.; Lumetta, G. J.; Fiskum, S.; Peterson, R. A., Boehmite actual waste dissolution studies. *Separation Science and Technology* **2008,** *43*, (9-10), 2900-2916.

14. Fiskum, S. K.; Buck, E. C.; Daniel, R. C.; Draper, K. E.; Edwards, M. K.; Hubler, T. L.; Jagoda, L. K.; Jenson, E. D.; Kozelisky, A. E.; Lumetta, G. J. *Characterization and Leach Testing for REDOX Sludge and S-Saltcake Actual Waste Sample Composites*; Pacific Northwest National Lab.: 2008.

15. Wells, B. E.; Kurath, D. E.; Mahoney, L. A.; Onishi, Y.; Huckaby, J. L.; Cooley, S. K.; Burns, C. A.; Buck, E. C.; Tingey, J. M.; Daniel, R. C. *Hanford Waste Physical and Rheological Properties: Data and Gaps*; Pacific Northwest National Laboratory (PNNL), Richland, WA (US): 2011.

Pacific Northwest
National Laboratory

902 Battelle Boulevard
P.O. Box 999
Richland, WA 99354
1-888-375-PNNL (7665)

www.pnnl.gov